Glaciers, erosion and climate change in the Himalaya and St. Elias Range, SE Alaska

Adam D. Barker

A dissertation
submitted in partial fulfillment of
the requirements for the degree of

Doctor of Philosophy

University of Washington

2016

Reading Committee:

Bernard Hallet, Chair

Howard Conway

Alan R. Gillespie

Edwin D. Waddington

Program Authorized to Offer Degree:
Department of Earth and Space Sciences

University of Washington

Abstract

Glaciers, erosion and climate change in the Himalaya and St. Elias Range, SE Alaska

Adam D. Barker

Chair of the Supervisory Committee:

Professor Bernard Hallet
Department of Earth and Space Sciences

The important roles of glaciers in topographic evolution, relief development, and sediment production are well recognized but understanding remains rather limited largely because of the inherent complexity of glacial erosion in diverse terrains, the lack of validated glacial erosion models, and the sparse nature of the data available on erosion rates. The primary focus of this research is defining and understanding rates of glacial erosion and their spatio-temporal variation at the scales of single glacier basins and entire orogens. I study glacial erosion in two tectonically active mountain ranges, the Himalaya and the St. Elias Range (Alaska), ideally suited for this study because of the wealth of pertinent data already available, and because they represent a broad range of climates and glacier types. In the Himalaya study, I also examine the impact of the debris produced by glacial erosion that accumulates on the glacier surface on glacier mass balance and the response of the glacier to climate change. In the SE Alaska study, I model the spatial pattern of erosion rates over an entire glacial cycle, and compare the temporally averaged rates to published rates of exhumation to validate and calibrate an erosion model. These model results illuminate the source region and temporal aspects of the offshore sediment record that have received

considerable attention in the context of climate-driven modulation of erosion and sediment production.

Large data sets on exhumation rates spanning the entire Himalayan arc have documented spatial and temporal variations in erosion rates; however, data on glacial erosion rates at the heavily glaciated crest of the Himalaya are very sparse. In light of this weakness in the knowledge base, I integrate several types of field research to investigate rates of erosion for a single glaciated basin at the base of Mt. Everest. I found that erosion rates for two timescales, contemporary (10^1 yr) and over the Holocene (10^4 yr), are similar to published long-term (O ~ 10^7 yr) exhumation rates (~1 mm/yr) derived from thermochronometric data in the region. The apparent uniformity of erosion and exhumation rates over a large range of time implies a surprising insensitivity to likely variations in climate, structural development, and relief evolution; it also contrasts with recent studies emphasizing the variation of rates over different timescales. Moreover, measurements of the suspended sediment flux out of the proglacial stream suggest that the fluvial evacuation rate of suspended sediments is ~50x less than the contemporary sediment production rate. This, together with the known time over which sediment has accumulated in the basin, the downglacier decrease in sediment flux, and evidence that the contemporary glacier is perched on a 20–100 m thick debris edifice, implies that most of the eroded debris remains within the basin. This result provides new insights into the geomorphic development of the high relief in the Himalaya, and the episodic nature of the downstream transfer of sediment from high glaciers.

To investigate links between basin erosion, debris transfer, and the evolution of debris-covered glaciers during periods of climate change, I numerically model the coupled evolution of ice and debris for Khumbu Glacier. For the first time, I define a relationship between ice-melt rate and debris thickness, representative of the thick surface debris characteristic of the Khumbu region, and implement it in the model to quantitatively explore the "debris-covered glacier anomaly". The model simulates the response of a debris-covered glacier to changes in climate forced by variations in the net mass balance represented by vertical shifts in the equilibrium line. Model results indicate that despite the thick debris cover, Khumbu Glacier has thinned at rates similar to current rates measured by remote sensing, averaging 0.4 m w.e./yr, for over a century since the Little Ice Age (LIA). Even under a constant climate, it will continue to thin into the future, by about 6–8% by AD2100, largely in the middle part of the glacier with minor changes in the terminus ice thickness and extent.

In SE Alaska, I expand the study region from a single catchment to an entire orogen where I model the spatial distribution of erosion rates on two timescales, the present-day and the longer-term. The latter represents the past ~100-kyr when much larger ice masses covered the study area and underwent large oscillations; by inference, it represents the Quaternary during which these large oscillations prevailed and much of the orogen was exhumed. I hypothesize that the rate of erosion increases with the glacier power, the amount of energy available for erosion per unit time and per unit area of the glacier bed, which has the advantage of representing the strength of the ice-bed coupling, the basal shear stress, as well as the sliding rate. When averaged over an entire major cycle, glacier power accounts for nearly 70% of the variation in the published exhumation rates inferred from

thermochronology data from the entire orogen despite the large range of substrate characteristics expected in the region. The strong correlation between exhumation rates and glacier power validates the hypothesis that the rate of erosion scales with power and the numerical erosion model. Model results define the zones of rapid exhumation as the zones of steep and rapid glaciers. Moreover, the results dispel the notion that rapid erosion is spatially coincident with the long-term position of the equilibrium line; averaged over the major Quaternary glaciations, the position of the equilibrium line is well south of zones of rapid exhumation, close to the continental shelf break in the Gulf of Alaska.

TABLE OF CONTENTS

LIST OF FIGURES

LIST OF TABLES

ACKNOWLEDGEMENTS

I begin by thanking Bernard Hallet, whose vast knowledge and broad scientific understanding opened up worlds I never knew existed. Thank you to my committee members, Howard Conway, Alan Gillespie, and Ed Waddington, who provided essential encouragement and help. I especially want to thank Twit for your effort and support.

My work brought me to locations that are the extremes of this world. Thank you to my field assistants Taylor Brugh, Lauren Wheeler and Trevor Hillebrand, who had to endure the beauty of the Khumbu region and also do work. I also thank Peter Koons, my Master's advisor, and Sean Birkel, for their integral assistance and modeling results that went into the SE Alaska project. The NSF and the Quaternary Research Center provided financial support.

I have worked alongside some incredibly smart people, far more than I can possibly mention out of fear of leaving anybody out. More important, I have made some life-long friends at UW, most notably Brooke Medley, T.J. Fudge, Isaac Larsen, and Kristin Poinar. I want to thank you for being the wonderful people you are. And to my family, thank you for your love and support.

I must also acknowledge Brooke Medley, a very special person to me.

Chapter 1: Introduction

Rates of erosion and debris production at the crest of the Himalaya, the quintessential tectonically active mountain range, are poorly known, yet it is widely recognized that erosion plays a central role in mountain building and that debris strongly influences the sensitivity of glaciers to climate change. In contrast, erosion rates averaged over individual glacier basins and over timescales of 10 to 10^6 years are relatively well defined in the St Elias Range, SE Alaska through studies of sediment flux and thermochronology, respectively. However, the link between the pace of erosion and glacier characteristics has received little attention, and very little geologic data exist to define empirically the spatial variation of erosion rates within the vast areas of individual glacier systems that reach 5000 km^2. Moreover, long-term variations in the pattern of erosion driven by growth and shrinkage of glaciers during typical glacial cycles are poorly understood. Consequently, the relationship between the dynamic glaciers and the rapid exhumation in the St Elias Range remains poorly defined.

This thesis aims to constrain the temporal variations of glacial erosion rates at the crest of the Himalaya, Nepal, and their spatial and temporal variation in the St. Elias Mountains, SE Alaska. In the Himalaya, I also examine the impact of the debris produced by glacial erosion, which accumulates on the glacier surface, on the mass balance of a glacier and on its response to climate change. This work bears on several topics of considerable current interest within the scientific community and of direct societal relevance. Three substantive chapters (2-4) comprise the thesis and are followed by a summary. In this chapter, I introduce important underlying concepts and

provide context for the research reported herein. I start by introducing the importance of glacial erosion studies, and explaining what is known and is not known about glacial erosion rates. I, then, follow with a primer on how glacier erosion is implemented in numerical models and review modeling studies investigating the influence of debris on glacier evolution in the Mt. Everest region.

1.1 Importance of glacial erosion

Understanding the spatial and temporal variations of glacial erosion rates not only helps define the influence of glaciers on Earth's surface but also helps address topics in diverse disciplines in which glacial erosion plays a vital role. 1) Geodynamics: the influence of glacial erosion on mountain building and the interplay between tectonics, topography, and surface processes (e.g., Molnar and England, 1990; Beaumont et al., 2001; Zeitler et al., 2001; Wobus et al., 2003; Tomkin, 2007; Berger et al., 2008; Scherler et al., 2011; Valla et al., 2011; Yanites and Ehlers, 2012; Herman et al., 2013, 2015; Enkelmann et al., 2015; Herman and Champagnac, 2016; Willenbring and Jerolmack, 2016). 2) Marine geology: offshore glacial sediment sequences record spatial and temporal patterns of sediment production that reveal the influence of climate variability on erosion processes (e.g., Hallet et al., 1996; Elverhøi et al, 1998; Peizhen et al., 2001; Molnar, 2004; Koppes and Hallet, 2006; Gulick et al., 2015; Koppes et al., 2015; Fernandez et al., 2016). 3) Glaciology: sediments that underlie ice masses (e.g., the ice streams that drain much of the West Antarctic Ice Sheet) may enhance glacier motion and influence the position of ice streams by reducing bed roughness and lowering resistance to flow (e.g., Weertman, 1964; Anandakrishnan et al., 1998; Tulaczyk et al., 2000; Alley et al., 2003; Joughin et al., 2004; Smith et al., 2013; Seigert et al., 2016). 4) Climate change and sea-level rise: ice/ocean interactions have

received much attention in part due to the role of offshore sediments in controlling the advance of marine-terminating glaciers into deep water (e.g., Meier and Post, 1987; Nick et al., 2007; Pollard and DeConto, 2009; Love et al., 2016), and their retreat that tends to be more rapid (e.g., Benn et al., 2007; Nick et al., 2007; Straneo et al., 2010, 2011; Motyka et al., 2013; Rignot et al., 2016).

Despite the importance of glacial erosion, rates of erosion are only defined by sparse data, and the diversity of rates is not understood. Numerous field studies in SE Alaska of sediment accumulation in fjords (e.g., Koppes and Hallet, 2002; 2006), on the continental shelf (Jaeger et al., 1998; Sheaf et al., 2003) and in the deep sea part of the Gulf of Alaska (Gulick et al., 2015) have, respectively, documented spatially averaged erosion rates over multiple timescales for individual glacier systems and regional rates. In a comprehensive overview of existing data, Hallet et al. (1996) reported effective rates of glacial erosion from sediment yields over years or decades reaching or even exceeding 10 mm/yr for large and fast-moving temperate valley glaciers in the tectonically active ranges of SE Alaska. At Tyndall Glacier in SE Alaska, Koppes and Hallet (2006) estimated the long-term, basin-wide erosion rate to be 9 ± 2 mm/yr after applying a correction factor accounting for glacial retreat and the release of stored sediment. On the shelf, sediment accumulation rates averaged nearly 8 mm/yr over the Holocene, corresponding to an average erosion rate of 5.1 mm/yr, which they attributed to efficient erosion by glaciers (Sheaf et al., 2003). Over longer time scales, drilling of deep-sea sediment deposits shows an acceleration in sediment yields following the onset of ~100-kyr glacial cycles; the evacuation of eroded crustal material appears to outpace the tectonic influx by 50-80% (Gulick et al., 2015). Collectively, the studies of sediment accumulation in fjords, on the shelf, and in the deep sea suggest that

erosion rates in SE Alaska are some of the highest in the world. For glaciers in Patagonia and the Antarctic Peninsula, Koppes et al. (2015) reported a three order of magnitude difference in basin-averaged erosion rates inferred from 15 outlet glaciers spanning 19 degrees of latitude. Their findings, which show how glacial erosion rates increase with decreasing latitude, suggest that climate and the glacier thermal regime exert more control on erosion rates than do ice cover extent, ice flux, or sliding speeds. However, using sediment volumes as a proxy for glacial erosion is not without controversy as the incompleteness of the sediment record and remobilization of previously deposited sediments confound the erosion signal (e.g., Sadler, 1981; Sadler and Jerolmack, 2014; Cowan et al., 2010; Boldt et al. 2016; Herman and Champagnac, 2016; Ganti et al., 2016).

Unlike the offshore sediment record, thermochronometric methods allow for quantification of local erosion rates for the source regions producing the sediment. Specifically, low-temperature thermochronology can be used to determine the time since a mineral cooled through a closure temperature window, which is generally due to exhumation over million-year timescales (Dodson, 1973). The cooling age is converted into an erosion rate making the reasonable assumption for convergent orogens that erosion accounts for the exhumation, and using estimates of the near-surface temperature gradient; however, uncertainties in the geothermal gradient lead to corresponding uncertainties in the interpretation of thermochronometric data (e.g., Herman et al., 2013; Enkelmann et al., 2015). Global compilations of exhumation data reveal an increase in erosion rates in mountain ranges since ca. 6 Ma and most rapidly since 2 Ma (Herman and Champagnac, 2016); the increase in erosion rates has been reported a number of regions, including both SE Alaska (Berger et al., 2008) and parts of the Himalaya (Thiede and Ehlers, 2013).

In SE Alaska, many thermochronometric studies have documented rapid erosion and deep-seated rock exhumation (e.g., Berger et al., 2008; Enkelmann et al., 2008, 2009, 2010, 2015; Grabowski et al., 2013; Falkowski et al., 2014). Detrital zircon fission track (FT) ages reveal rapid exhumation (~2-5 mm/yr) primarily under the Hubbard and Seward-Malaspina Glacier systems (Enkelmann et al., 2015). Previous studies have used the spatial correlation between rapid exhumation and the current state of glaciers and equilibrium line (EL) position as evidence of a link between climate and erosional processes (Berger et al., 2008); however, this general notion fails to take into account specific controls on erosion rates and the large changes in the ice masses through the Quaternary.

In contrast with SE Alaska, very little data exists on erosion rates for Himalayan glaciers. Using a method that parallels Chapter 2 of this thesis, Heimsath and McGlynn (2008) estimated the headwall retreat rate of 1.3 ± 0.5 mm/yr for a debris-covered glacier on the north slope of the Annapurna Range, central Nepal. Faster contemporary erosion rates of 5–7 mm/yr were derived for Raikot Glacier, Nanga Parbat (Gardner and Jones, 1993). In the Marsyandi river catchment, modern basin-wide erosion rates of 0.1 to 2.0 mm/yr were reported in sparsely glaciated catchments based on suspended sediment flux measurements (Gabet et al., 2008). Erosion is fast, however, for at least one major mountain in the Himalaya in the eastern most Himalaya. Detrital zircons from a stream draining the cirque glacier incising the north flank of Namche Barwa yielded a population of extremely young ages characterized by a number of peaks, the youngest of which is 0.3 Ma and accounts for 35% of the 81 grains analyzed; the oldest grain in this entire sample is 3.6 Ma (Enkelmann et al, 2011). The dearth of information highlights the need for additional studies.

1.2 Glacial erosion and representation in models

The deeply incised valleys of glaciated regions leaves little doubt that glaciers actively erode and efficiently remove rock debris. From the early illustrations and descriptive studies by Chamberlain (1885) to sophisticated analog experiments by Iverson and Zoet (2015), a wide range of studies and experiments have improved our knowledge of glacial erosion. In this section, I outline published theoretical and experimental studies on glacial erosion and review the representations of glacial erosion in past models of landscape evolution.

Glacial erosion and sediment production occur primarily by two processes: abrasion and quarrying. Abrasion is the dominant producer of fine sediments and has received much attention in the literature (Glen and Lewis, 1961; Boulton, 1974; Hallet, 1979; 1981). Abrasion depends on the flux and lithology of rock fragments in contact with the glacier bed, the shapes of the bed and fragments, and the effective contact force; the rate of abrasion is proportional to the rate at which work is done on rock-to-rock friction on the glacier bed (Hallet, 1979). Quarrying (plucking) occurs following cracking and dislodgement of bedrock and supplies rock fragments for abrasion. Cracks form due to stress concentrations that tend to be enhanced by variations in basal water pressure (Rothlisberger and Iken, 1981; Cohen et al., 2006). Field observations, theoretical considerations, and cosmogenic nuclide studies (Briner and Swanson, 1998) suggest that quarrying dominates over abrasion. Mechanistic models of abrasion (e.g., Hallet, 1979) and quarrying (e.g., Hallet et al., 1996, Iverson, 2012) assume that basal sliding is the primary control on the rate of glacial erosion; however, estimating absolute erosion rates from the models is difficult due to poorly known basal conditions and bed properties.

In numerical models, glacier erosion has been represented over length scales ranging from a single landform (Harbor, 1992) to an entire mountain range (Egholm et al., 2009). As summarized by Iverson (2012), bedrock erosion rate is generally represented in models as::

$$\dot{E} = a u_s^b \qquad \text{(Eq. 1)}$$

where u_s is the glacier sliding speed and a and b are constants (Harbor, 1992; Humphrey and Raymond, 1994; Braun et al., 1999; MacGregor et al., 2000; Tomkin, 2007, 2009; Herman and Braun, 2008; Kessler et al., 2008; Egholm et al., 2009; Herman et al., 2015). The constant, a, depends on bedrock properties and basal conditions. Other forms assume that erosion rate scales with ice discharge:

$$\dot{E} = a_f \bar{u} H \qquad \text{(Eq. 2)}$$

where a_f is similar to a but with units of m^{-1}, $\bar{u}$ is depth-averaged velocity and H is ice thickness (Kessler et al., 2008). Herein, in chapter 4, the erosion rate is assumed to scale with glacial power, the product of the sliding speed and basal shear stress, τ_b:

$$\dot{E} = a_p u_s \tau_b \qquad \text{(Eq. 3)}$$

where the proportionality factor is a_p with units: Pa^{-1} (Pollard and DeConto, 2007; Hallet et al., 2011; Melanson et al., 2013). The glacial power approach combines the widely recognized importance of glacial sliding with the coupling strength of the glacier and bed (Hallet, 2011). While modeling the spatial variation in erosion rates for Seward Glacier, Headley et al. (2012) compared the erosion rate models from Eqs. 1-3; they reported that the basin geometry exerted stronger control on the spatial distribution of erosion rates than both the model choice and equilibrium line, which is commonly invoked in discussions of patterns of glacier erosion because the ice flux is greatest there.

1.3 Modeling the response of debris-covered glaciers to climate change

The response of glaciers to climate change is of fundamental scientific interest, and has important practical consequences, including fresh water availability, global sea-level change, and environmental hazards (e.g., Richardson and Reynolds, 2000; Immerzeel et al., 2010). A significant threat to Himalayan communities is moraine-dammed lakes that form following glacier recession or subsidence (Bolch et al., 2008a; Benn et al., 2012; Thompson et al., 2012). Recent studies show that the areal extent of glaciers in the Everest region, including many with a thick debris cover, decreased 5% during the second half of the 20th century (Bolch et al., 2008b; Salerno et al., 2008). The glaciers are also thinning actively. For Khumbu Glacier, the rate of thinning across the ablation area averaged 0.38 ± 0.07 m/yr between 1970 and 2007 (Bolch et al., 2011). Predicting the future of Himalayan glaciers and, hence, assessing the societal consequences are especially challenging due to the presence of surface debris, which strongly influences glacier mass balance and evolution (e.g., Scherler et al., 2011, Anderson and Anderson, 2016).

To shed light on glacier changes in the Khumbu region, and by extension in similar settings along the Himalaya and elsewhere, several researchers have used numerical models to examine the current state of Khumbu glacier and its probable evolution. Naito et al. (2000) coupled mass balance glacier flow to investigate shrinkage of the Khumbu between 1978 and 1999. They predicted that the lowest part of the glacier would stagnate and eventually decouple from the upper glacier, which could lead to the development of a large and potentially hazardous glacial lake. Shea et al. (2015) used a glacier mass balance and ice-flow model to examine historical change of glaciers in the Everest region from 1961 to 2007 and assess future changes. They concluded that glaciers may lose between 73 to 96%

of their total volume due to sustained warming by the year 2100. Rowan et al. (2015) coupled ice flow with debris evolution in a three-dimensional model, and focused on interactions between the debris cover and mass balance. Model simulations quantified the imbalance of Khumbu Glacier with the current climate, which is evident from the current and post-Little Ice Age (LIA) thinning of the Khumbu. They suggest that even without a further change in climate, Khumbu Glacier will continue to respond to post-LIA warming until AD2500. In another study, Anderson and Anderson (2016) developed a transient 2-D model to investigate debris cover and glacier evolution for generic debris-covered glaciers, using Khumbu Glacier as a case example. Unlike Rowan et al. (2015), they focus on improving understanding of glacier evolution solely in response to changes in debris cover; in this initial modeling phase, they do not consider the effects of climate change. These numerical models provide insight into the response of Khumbu and other debris-covered glaciers to climate change, and provide a rich backdrop for this study.

1.4 Thesis roadmap

In this thesis, I address glacial erosion in a glaciated basin in Nepal and over an entire orogen in SE Alaska. For the Nepalese glaciated basin, I also consider the storage and evacuation of debris, and the effect of the eroded rock debris on the response of glaciers to adverse climatic trends in Nepal. Chapters 2 and 3 report the findings of several field seasons of measurements and numerical modeling regarding Khumbu Glacier, Mt. Everest region of Nepal. In Chapter 4, I investigate erosion rates in the St. Elias Mountains, the highest coastal mountain range in the world. My thesis addresses the following questions:

- In Himalaya, what is the pace of erosion at the crest of the range and has it changed over time? **Chapter 2**
- How does debris influence glacier evolution? **Chapter 3**
- How can we improve understanding and predictions of the future behavior of Khumbu Glacier, and similar glaciers? **Chapter 3**
- In Alaska, what is the spatial and temporal variation in erosion rates and what is the link between glacial erosion and exhumation and tectonics? **Chapter 4**

Chapter 2: Glacial erosion, exhumation, and debris evacuation over a wide range of time scales in the Mt. Everest region, Nepal

2.1 Abstract

The pace of erosion in the Himalaya has been studied extensively, yet few studies have addressed the glaciated crest of the orogen. New and existing data from Khumbu Basin at the base of Mt. Everest are used to define erosion rates over two time scales: contemporary and the Holocene (O ~ 10^1 and 10^4 yr). Erosion rates are calculated using field and remote sensing measurements of the flux of rock debris from the basin. The underlying premise is that just as the flux of glacier ice is sustained by input of snowfall, the flux of debris is sustained by erosion. Contemporary and Holocene basin-averaged erosion rates, on average 0.6 and 0.8 mm/yr, respectively, are very similar to one another, suggesting that erosion of the Khumbu basin has, on average, maintained a steady pace over time scales up to 10^4 years. Contemporary suspended sediment evacuation is ~50x less than the Holocene-averaged sediment production. This, together with evidence that the contemporary glacier is perched on a debris edifice, implies that most of the eroded debris remains within the basin. Moreover, the basin-averaged erosion rates are similar to published long-term (O ~ 10^7 yr) exhumation rates derived from thermochronometric data in the region. This similarity contrasts with other studies that suggest exhumation accelerated significantly with the onset of Plio-Pleistocene glaciation; our results point to the need for additional studies of erosion in other high regions in the Himalaya.

2.2 Introduction

The rate and spatial pattern of erosion and exhumation in the Himalaya have been studied extensively using diverse approaches, largely because of the important role exhumation plays in the development of the range. For example, in a comprehensive study across the entire Himalaya, significant spatial and temporal variations in exhumation rates were inferred from more than 10^3 mineral cooling ages obtained from in-situ bedrock samples (Thiede and Ehlers, 2013). Within the range, a few basins, the Sutlej (Thiede et al., 2004; Vanney et al., 2004; Bookhagen et al., 2006) and the Marsyandi (Burbank et al., 2003, 2012; Hodges et al., 2004; Pratt-Situala et al., 2004; Brewer et al., 2006; Huntington et al., 2006; Garzanti et al., 2007; Godard et al., 2012) in particular, have been studied in detail, while other areas have received sparse attention. Beyond the Himalayan arc, much work has focused on the two syntaxial regions at the ends of the range: the Nanga Parbat (Zeitler, 1984; Gardner and Jones, 1993; Burbank et al., 1996; Zeitler et al., 2001; Koons et al., 2002) and Namche Barwa massifs (Clark et al., 2004; Hren et al., 2007; Finnegan et al., 2008; Stewart et al., 2008; Enkelmann et al., 2011; Larsen and Montgomery, 2012; Lang et al., 2013; Zeitler et al, 2014).

However, little is known about erosion rates at the heavily glaciated crest of the Himalaya, which spans ~2000 km. Contemporary erosion rates of 5–7 mm/yr derived for Raikot Glacier, Nanga Parbat (Gardner and Jones, 1993) are similar to exhumation rates estimated for the region over time scales of 10^6 yr (Zeitler et al., 2001). Comparable, but slightly faster exhumation has also been inferred from sediments from a stream draining the steep glacier on the West flank of Namche Barwa (Sample H, Enkelmann et al., 2011). On the other hand, relatively slow erosion, ~1.3 mm/yr, determined from contemporary headwall

retreat rates were reported for a high basin in Nepal (Heimsath and McGlynn, 2008), and modern basin-wide erosion rates of 0.1 to 2.0 mm/yr were reported in sparsely glaciated catchments based on suspended sediment flux measurements (Gabet et al., 2008). In the latter study, it was argued that relatively rapid erosion during periods of glaciation (e.g., Hallet et al., 1996) would compensate for the slow erosion now occurring in the High Himalaya (Gabet et al., 2008). In contrast, Rahaman et al. (2009) found that sediment yields in the High Himalaya decreased during periods of more extensive glacial cover in the past ~10^5 years. The sparse data currently available indicate highly varying erosion rates along the glaciated Himalayan crest, ranging from ~1–7 mm/yr, which points to the need for additional studies in those regions.

Here we synthesize existing data and present new data from Khumbu Basin to constrain erosion rates over two timescales: contemporary and the Holocene (O ~ 10^1 and 10^4 yr). We compare these rates with published exhumation rates over much longer times scales (O ~ 10^7 yr) derived from thermochronometric studies in the region (Sakai et al., 2005; Streule et al., 2012). Using field measurements and observations, and remote sensing data, we (i) quantify the modern debris flux (including suspended sediments flushed out of the basin), (ii) calculate the debris volume within Holocene-aged deposits. We also consider temporal changes in the rates of erosion and debris production, and implications for the evolution of the highest topography on the planet. Other aspects of Khumbu Glacier are considered in Chapter 3 of this thesis, which investigates the influence the eroded material has on ice melt. The Chapters are linked in many ways, with the overall goal in characterizing Khumbu Basin from two perspectives. First, from the view of a geologist, we consider erosion and long-term geomorphic evolution of Khumbu Basin. Second, from the

view of a glaciologist, we consider past and future states of the glacier and the important role of eroded debris in the evolution of Khumbu Glacier.

2.3 Existing and new glaciological and geological measurements

Khumbu Basin in Sagarmatha National Park, Nepal extends over an area of ~90 km^2 that is bordered by several of the world's highest peaks, including Mt. Everest (Fig. 2.1). The 18 km-long Khumbu Glacier descends from an elevation of about 7100 m to 4900 m and covers an area ~17 km^2. Snow and ice avalanches from the steep cliffs that surround the accumulation zone contribute to the mass balance of the glacier (Fig. 2.1 inset). Khumbu icefall, a steep, heavily crevassed region connects the accumulation zone with the relatively gentle-sloped, debris-covered ablation zone (Fig. 2.2). The modern equilibrium line altitude (ELA) is within the icefall at ~5700 m (Scherler et al., 2011).

Abundant geological and glaciological observations and measurements make Khumbu Basin ideal for our study:

1) Glacier surface and bed profiles: the surface profile along the centerline of the glacier was constructed from a 2003 ASTER DEM and the bed profile was calculated by differencing the surface and the ice-thickness profiles (Fig. 2.2). Seven ice-penetrating radar profiles from May 1999 show ice thickness decreasing from ~450 m (maximum thickness) near Everest Base Camp (EBC) to less than 20 m (minimum thickness) about 2 km from the present terminus (Gades et al., 2000). To our knowledge, ice thickness has not been measured in the upper glacier; we estimate it using measurements of surface slope and assuming a constant value, 10^5 Pa, for the basal shear stress, which is consistent with values we calculate for locations where the ice thickness is known.

2) Surface velocity profile: velocities derived from repeat measurements using satellite optical and radar sensors (Luckman et al., 2007; Quincey et al., 2009; Casey et al., 2012) range from ~60 m/yr just below the Khumbu icefall to less than 5 m/yr in the lower ablation area of the glacier (Fig. 2.2).

3) Distribution of surface debris: previous direct field measurements indicate the present-day thickness of surface debris varies from less than 0.1 m directly below the icefall to more than 2 m near the terminus (Nakawo et al., 1999). Our measurements over four field seasons during pre- and post-monsoon months in 2010-2012, including electrical resistivity tomography (ERT), quantified the spatial distribution and variability of surface debris (Fig. 2.3).

2.4 Framework for analyses

We begin by considering the contemporary erosion rate from the fluxes of surface and englacial debris, and of suspended sediments exiting the glacier through the proglacial stream. Calculation of the total volume of Holocene debris deposits in the Khumbu Basin allows us to compare contemporary erosion rates with those over ~10^4 years.

Excluding transient changes in the volume of debris stored in the basin above the ELA, the debris flux, Q_d, at any glacier cross-section represents the product of the spatially averaged erosion rate and the area of the basin upglacier of that section. Transient changes are neglected because the very steep slopes preclude significant storage of sediment above the glacier and the rapid ice flow above the ELA is not conducive to appreciable storage under the glacier. The debris flux is linked to the ice flux, Q_i, which can be estimated from available field and remote sensing studies:

$$Q_d(x) = U_s w D_s(1-\phi) + Q_i C_d \,, \qquad \text{(Eq.1)}$$

where the values of surface velocity U_s, thickness of surface debris D_s, porosity of the supraglacial debris ϕ, and the volumetric concentration of debris within the ice C_d, are averaged across the glacier width w. We assume that the englacial debris concentration is uniformly distributed. Here we adopt $\phi = 0.33$, based on measurements from nearby Ngozumpa Glacier (Nicholson and Benn, 2013). The contemporary area-averaged erosion rate, $\dot{E}_{Cont}$, scales with the sum of the glacier debris flux and the suspended sediment flux, Q_{sus}, in the outlet stream:

$$\dot{E}_{Cont} = \frac{\rho_s}{\rho_r}\frac{(Q_d + Q_{sus})}{A_B} \qquad \text{(Eq. 2)}$$

The density ratio, $\frac{\rho_s}{\rho_r}$ = 0.8 accounts for the density difference between sediment, ρ_s, and bedrock, ρ_r, (Heimsath and McGlynn, 2008), and A_B is the area of the contributing basin (26.5 km^2 is used to derive the contemporary erosion rate–Fig 2.8).

Next, we consider the Holocene timescale by examining the volume of debris currently residing in the basin. Multiple lines of evidence support the notion that debris has been accumulating since the Holocene. Near the base of the Khumbu terminal moraine, optically stimulated luminescence (OSL) dating of sediments yield ages at 10.9 ± 2.4 ka (Richards et al., 2000). Moreover, cosmogenic radionuclide (CRN) ^{10}Be surface exposure dates (9.2 ± 0.2 ka) of glacial deposits at the terminus of other glaciers in the region support the Holocene OSL age (Finkel et al., 2003). Studies of outwash fans, terraces and moraines in the Khumbu region show that glacial debris has been accumulating in the valleys since the last major glacier advance at ca. 10 ka (Chhukung stage; Williams, 1983; Nakawo et al.,

1999; Richards et al., 2000; Finkel et al., 2003; Barnard et al., 2006; Hambrey et al., 2008; Owen et al., 2009). Together, the data provide a time scale for Holocene sediment accumulation within the basin. The glaciers that correspond to older well-dated moraines, which are 16 ka and older (Finkel et al., 2003), would have filled the entire lower portion of Khumbu Valley, rather than only the central portion that is currently occupied by the current Khumbu Glacier. We expect that the broader valley had to be excavated during this and similar glacial advances, and hence that any unconsolidated debris would have been removed during the extended ice advance over this area. Moreover, stratigraphic and sedimentology relationships suggest that formation of fans and terraces occurs during glacier retreat (Barnard et al., 2006). Hence the volume of glacial debris eroded during the Holocene, V_D, is estimated from all the debris bounded by the Holocene-aged moraines and regions upvalley. Therefore, the average erosion rate over the Holocene, $\dot{E}_{Holo}$, is the sum of the volume of debris and the volume fluvially evacuated from the basin, V_f, over period, *t*, and the area of the Khumbu basin, A_B (70 km^2 is used to derive the Holocene erosion rate– Fig 2.8):

$$\dot{E}_{Holo} = \frac{\rho_s}{\rho_r}\frac{(V_D+V_f)}{A_B t} \qquad \text{(Eq. 3)}$$

2.5 Materials and methods

2.5.1 Contemporary erosion rates

The contemporary erosion rate for the portion of the basin above the ELA was calculated from the surface and englacial debris fluxes at the uppermost cross-section in Fig. 2.1, using Eq. 2. The ~10–50 yr-timespan represented in the contemporary analysis reflects the period in which the principal characteristics (i.e., glacier thickness and velocity) are well

documented. Near EBC, the site of the upper ice-thickness survey, the ice surface elevation changed less than 5 m between 1970 and 2007 (Bolch et al., 2011).

To determine the debris flux, we used published and our new measurements of surface ice velocity, glacier thickness and width, surface debris thickness and englacial debris concentration. The debris flux cross-sections, shown in Fig. 2.1, correspond to locations of measured ice thickness (Gades et al., 2000). Horizontal surface velocities were derived from feature tracking of distinct surface features using TerraSAR-X imagery between January and May 2008 (Courtesy of M. Braun); depth-averaged velocities were estimated by accounting for the decrease in velocity with depth (Cuffey and Paterson, 2010). Surface velocities were used to calculate surface debris flux and depth-averaged velocities were used to calculate the englacial flux.

The thickness of surface debris was measured pre- and post-monsoon in 2010, 2011 and 2012 (Fig. 2.3). The spatial variation of debris thickness was determined from ~125 direct field measurements over the entire ablation region using hand measurements, and at the top of ice cliffs using a Laser Range Finder. To augment these measurements we used ERT in the lower few kilometers of the glacier. The ERT surveys used an IRIS Syscal Kid system with 36 electrodes spaced 10 m apart. Because the glacier surface is very rough the maximum survey line-length was ~300 m. The output current was adjusted automatically to optimize measurement quality. Both Wenner and Dipole-Dipole configurations were tested in the field; during processing, it became evident that the Wenner array was more effective in identifying the relatively flat ice/debris interface. Electrode contacts were maintained by watering the electrodes in the debris with a saline solution. The data were filtered and processed using commercially available software, Res2D.

The ERT surveys clearly distinguished glacial ice, which includes englacial debris, (domains with resistivity > 10^6 Ω m (Reynolds, 1985; Haeberli et al., 1988)), from surface debris or moraine deposits (~1.5 x 10^4 Ω m (Nakawo et al., 1999)). The most complete section, Line B-B' that runs N-S (Fig. 2.4), shows that the ice-debris contact is nearly horizontal. The internal consistency of the surveys was excellent where it could be assessed at the cross-over point, X, in lines A-A' and B-B'; here, the debris thickness over a substantial part of the domain is ~5 m. In several surveys (notably line D, and parts of A and B), the electrode coupling with the debris was poor, limiting acquisition of useful data (Fig. 2.4). Nevertheless, we show data from all surveys to highlight the challenges of surveying glaciers covered with loose, dry debris.

2.5.2 Holocene erosion rate

Holocene sediment volumes were estimated from field measurements and DEM analysis. Parabolic functions were used to approximate the geometries of 25 U-shaped valley cross-sections (Mey et al., 2015); a DEM of the bedrock surface was constructed by simply interpolating between the cross-sections. Fig. 2.5 shows three representative cross-sections for the upper, middle, and lower parts of the glacier and the approximation of the bedrock and sediment/glacier interface. Additional cross-sections (not shown) used to calculate deposit volumes include cross-sections for the tributary glaciers that likely fed the Khumbu during the Little Ice Age, and other periods of the Holocene. These tributary glaciers are included in calculation of the Holocene contributing-basin area (Fig. 2.8).

Sediment volumes for the Holocene analysis were split between two domains: Khumbu Glacier and Khumbu Basin. Khumbu Glacier includes surface, englacial and subglacial debris described above. Khumbu Basin includes Khumbu Glacier and the massive

lateral and terminal moraines bordering the glacier and the tributary glaciers, as well as the total volume of sediment evacuated in the proglacial stream during the Holocene. The volume of the lateral and terminal moraines was estimated using DEMs, composite images of VNIR (visual near-infrared) bands from an ASTER image collected in April of 2003, and thickness measurements from a laser-range finder gathered during field seasons. The transverse profile of the massive terminal moraine is rounded and tapers downvalley; we estimated its volume by abstracting this edifice as a half-cone with a range of sizes. Tributary glacier volumes were estimated using corresponding data from Khumbu Glacier, and the surface thickness was assumed to be identical to that at the same elevation on the Khumbu.

In addition to stored debris, the amount of debris evacuated fluvially during the 10^4 year period was determined by assuming that the modern fluvial flux averaged over two years of suspended sediment monitoring in the proglacial stream is representative of the Holocene. Likely, the value represents a lower bound due to episodic high-discharge events that were not captured in our suspended sediment study. We monitored the suspended sediment flux in the principal outlet stream during the 2011 and 2012 monsoon season. We used two nearby sites: 1) ~0.5 km upstream from the small settlement of Thukla where the stream forms a single channel directly beyond the moraine and where we felt confident the equipment would remain undisturbed (Fig. 2.1) and 2) just upstream from Thukla. At site 1, we monitored stage, water temperature and turbidity continuously; measurements were automated at 15-minute intervals with stage and water temperature recorded using a HOBO water level logger, and turbidity averaged over five measurements monitored using a Campbell Scientific OBS 3+. At site 2, we measured stage visually and photographically; we also collected water samples periodically to determine the suspended sediment

concentration (SSC). Additional information about our SSC measurements is in supplementary section 2.9.

2.6 Results

2.6.1 Contemporary erosion rates

Surface debris: Debris emerges from the glacier at the surface in patches that coalesce to form a nearly continuous monolayer about 2 km down glacier from the ELA near EBC. Our 30 evenly spaced point measurements roughly parallel to glacier flow near EBC showed debris thickness ranging from 0.008 to 0.08 m (averaging 0.03 ± 0.03 m). A few kilometers down glacier, debris thickness across the top of an ice cliff varied from 0.85 to 2.5 m in just 10 m. Measurements at other locations down the glacier, showed both increasing debris thickness and increasing local variability. Fig. 2.3 summarizes the surface debris thickness data; thickness was most variable near the terminus where the ERT measurements augment ice-cliff-top measurements. In nearly all cases, the ice-cliff-top measurements, which are included in Fig. 2.3, were less than those from the ERT, resulting in asymmetric error bars (Fig. 2.3).

Englacial debris: We are unaware of any measurements of englacial-debris concentration for Khumbu Glacier, but data exist for other temperate alpine glaciers (Table 2.1). Here we select a range of values based on Table 2.1 centered on 2 kg/m^3, which is similar to the mean value for Raikot Glacier in the Punjab Himalaya (Gardner and Jones, 1993). The two glaciers have similar configurations: a high elevation accumulation basin surrounded by steep slopes, which transitions through a steep icefall to a low-gradient ablation zone.

Debris Flux: At the uppermost cross-section in Fig. 2.1, the total debris flux, both surface and englacial, was used to estimate the contemporary erosion rate for the upper Khumbu catchment (Eq. 2). Near EBC, the englacial contribution dominates the total debris flux (erosion rate) for the upper catchment (Fig. 2.6); uncertainty in the englacial-debris flux is calculated using the range of debris concentrations measured on other glaciers (Table 2.1). We also calculate uncertainty in surface-debris thickness based on our new spatially distributed measurements. Using these values in Eq. 2, the contemporary upper basin-wide erosion rate is 0.6 ± 0.3 mm/yr.

For all cross-sections in Fig. 2.1, surface and englacial debris fluxes are summarized in Fig. 2.6. While englacial transport dominates in the first two cross-sections, most of the debris in the lower five sections is advected along the surface. The flux of surface debris increases for about 3.5 km down glacier from EBC; further down glacier it remains relatively constant (Fig. 2.6). The surface flux profile reflects spatial variations in debris thickness and the glacier velocity. For example, with a constant debris thickness, the flux of surface debris would be proportional to the ice velocity. The nearly constant flux suggests a balance between diminishing ice speeds and the dynamic thickening of the surface debris that is caused by the slowdown of the ice (Fig. 2.2) and the active surface melting. The relationship between the surface melting and the lowering, as well documented from satellite data (Bolch et al., 2011), is discussed elsewhere (Chap. 3).

In general, the total debris flux decreases steadily down glacier except near the terminus, which implies active loss of debris from the glacier, along the length the ablation zone; the debris is evidently transferred to the glacier base, as it is not accumulating elsewhere off the glacier. Along the glacier sides, the steep inner slopes of the moraines

would more likely function as sources of surface debris than sinks of debris. Moreover, leakage of debris out of the confines of Khumbu Glacier is unlikely because sediment evacuation rates in the proglacial stream are insignificant (Section 2.9). This discovery that debris is currently lost from Khumbu Glacier, along the length the ablation zone, and accumulating below the glacier is supported by evidence that the modern glacier is perched on a thick valley fill of debris that accumulates over time. Near the terminus, ice is at most 20 m thick (Gades et al., 2000), yet the crest of the glacier terminus rises more than 200 m above the modern valley surface. This debris flux analysis, which is developed in the next paragraph, also provides an opportunity to assess the rate of formation of thick subglacial debris edifice for other Himalayan glaciers, which have been illustrated in the literature (Benn and Evans, 2000; Westoby et al., 2014).

From mass conservation, the rate of change in the total debris thickness can be quantified from the divergence of the total flux of debris (Fig. 2.6) and was approximated as the ratio of the change in debris flux measured at two adjacent cross-sections, $Q_{up} - Q_{down}$, to the distance between the defining sections, Δx (Fig. 2.1). Q_{up} is the upglacier location. Thus, the deposition rate of debris beneath the glacier, $S_{basal}(x)$ is:

$$S_{basal}(x) = \frac{1}{w(x)} \frac{Q_{up} - Q_{down}}{\Delta x} \qquad \text{(Eq. 4)}$$

For the analysis, the glacier was subdivided into six zones defined by seven ice-thickness profiles across the width of the glacier (Gades et al., 2000). Glacier variables at each profile include the depth-averaged glacier velocity, the average glacier thickness, width across the glacier (defined by surface velocities), ice flux, and distance between each flux gate. For all zones, the rate at which debris is lost from the glacier, and presumably accumulating at the bed, ranges from 0.6 to 5.0 mm/yr (average 1.7 mm/yr). The rate of

basal deposition is highest in the three upper zones and steadily decreases down glacier to a minimum value near the terminus. The analysis is presented in greater detail in Chap. 3.

2.6.2 Holocene erosion rates

In contrast to the accumulation area, the lower part of Khumbu Glacier is surrounded by sediment accumulations (lateral and terminal moraines, and subglacial deposits) that have formed through the Holocene (Richards et al., 2000). The volume of debris stored or evacuated within the Khumbu Basin is summarized in Table 2.2 and estimates range from 0.5 to 0.9 km^3. The range of volumes shown in Table 2.2 reflects the uncertainty in the measurements. The bulk of the debris (0.3 to 0.6 km^3) is stored in the terminal moraine and debris edifice, lateral moraines and tributary glaciers. In fact, the massive terminal debris edifice contains about half the volume of the ~8 km long lateral moraines, which are evident in the southernmost cross-section in Fig. 2.5 along with the depressed glacier surface. Near EBC it is likely that the glacier is sliding over bedrock and eroding it; whereas near the terminus, the glacier is perched on ~150 m of debris. Overall, debris on top of, within and beneath the glacier ranges from 0.1 to 0.3 km^3. The wide range, especially for the englacial, subglacial, and tributary glacier domains reflect the considerable uncertainties in the analysis.

Using Eq. 3, we estimate the Holocene basin-wide erosion rate is between 0.8 ± 0.2 mm/yr. This rate is ~50 times higher than that needed to sustain the measured suspended sediment fluxes from the basin (~0.015 mm/yr). This result indicates that much of the debris eroded over the last 10^4 years still resides in the basin, and implies that measurements of sediment flux in proglacial streams can lead to substantial under-estimates of erosion rates.

2.7 Discussion

2.7.1 The pace of erosion and exhumation of Khumbu Basin

Results suggest that, on average, erosion of Khumbu Basin has maintained a steady pace over time scales ranging from 10^2 to 10^4 years. Our estimated basin-averaged erosion rates are similar to exhumation rates derived from thermochronometric data in the region, which include both erosional and tectonic exhumation over timescales of ~10^6-10^7 years. Rates of exhumation since the mid Miocene (~9 Ma) derived from apatite and zircon fission track data on samples from the high slopes of Everest average 1.0 ± 0.2 mm/yr (Streule et al., 2012). Nearly uniform erosion and exhumation rates over a large range of time scales for the Khumbu Basin imply a surprising insensitivity to likely variations in climate, structural development, and relief evolution. For example, in terms of expected climate effects, frost cracking that likely affects headwall retreat rates, is sensitively dependent on temperature (Scherler, 2014). Furthermore, an ice-core sample from the north side of Everest showed significant variations in mean annual snow accumulation related to changes in the south Asian monsoon (Kaspari et al., 2007).

Our findings contrast with results of other studies that commonly report exhumation accelerating in the Himalaya and other regions worldwide with the onset of Plio-Pleistocene glaciation (Shuster, 2005; Thomson et al., 2010; Herman et al., 2013; Thiede and Ehlers, 2013; Herman and Campagnac, 2016). Our findings also contrast with a number of studies in diverse settings reporting a dependence of erosion rates on the duration of the period under study. For example, Kirchner et al. (2001) suggested that erosion rates measured over short timescales are lower than those over longer timescales in part because the shorter measurement periods tend to miss large, but ephemeral erosional events. On the other hand,

short-term sedimentary records often suggest faster erosion than longer-term records, which are more likely to reflect significant depositional hiatuses (Sadler, 1981; Finnegan et al., 2014). Moreover, erosion rates from glaciated basins decrease with the length of the period over which they are averaged (Fernandez et al., 2011; 2016). Yet based on our work in the Khumbu, we see little, if any, temporal variation, at least within a factor of 2. We note that our estimates of erosion rates integrate all processes operating in the Khumbu Basin, not just those associated directly with glacial erosion; we do not address the relative efficiencies of erosional systems: glacial, periglacial, or hillslope processes. They simply imply constant rates of erosion over time despite climate change, structural activity and relief evolution.

2.7.2 Implications for the structural and topographic development of Mt. Everest

The wealth of structural, metamorphic, and geochronological data from the Mt. Everest region provides insight into the evolution of the highest region on Earth. One of the principal Himalayan faults, the South Tibetan Detachment fault (STD), is exposed in the region; it consists of 1) the upper (brittle) Qomolangma detachment (QD) and 2) the lower (ductile) Lhotse detachment shear zone (LD) (Searle et al., 2003, 2006; Cottle et al., 2011). The two strands merge into one large-scale ductile shear zone to the North in the Rongbuk valley (Cottle et al., 2007; Streule et al., 2012). Collectively, they separate un-metamorphosed Ordovician limestone that extends to the peak of Mount Everest in the upper plate, from high-grade metamorphic rocks of the Greater Himalayan Sequence (GHS) below.

The GHS rocks beneath Everest were at high temperatures during a metamorphic event that lasted from ~39 Ma to ~17 Ma, while brittle faulting on the QD is likely younger than 16 Ma (Searle et al., 2003). Since the main phase of melting and metamorphism in the

GHS during the Miocene from ca. 21 to 16 Ma (Searle et al., 2003, Cottle et al., 2007; Hodges et al., 2000; Simpson et al., 2000; Cottle et al., 2009; Streule et al., 2010), the exhumation rate due to both tectonic extension and erosion in the Khumbu and nearby regions has averaged 1.0 mm/yr (Sakai et al., 2005; Streule et al., 2012). This exhumation probably switched from being driven by tectonic processes to erosion at 11–13 Ma, when movement on the STD in the Everest area ceased (Streule et al., 2012). Meanwhile, paleoelevation estimates based on hydrogen isotope ratios of hydrous minerals deformed in the STD during the Early Miocene suggest that mean surface elevations in the Everest region at that time were similar to modern ones (Gébelin et al., 2013). The history of the extreme relief of the Everest region, with several of the world's highest peaks and deep glacial valleys, remains essentially unconstrained. The deep glacial incision probably started when glaciers first developed at the crest of the range before the global Quaternary glaciation.

Sustained erosion of bedrock, even at the relatively low rate of 1 mm/yr, would exhume 10 km of crustal material over 10^7 years, the time scale since cessation of the STD movement. Hence, the absence of long-term surface uplift suggested by the paleoelevation study requires a close balance between bedrock uplift and erosion at the crest of the Himalaya despite substantial changes in climate during the onset of Pliocene-Pleistocene glaciation and major changes in monsoonal circulation. This result is consistent with recent global datasets of sediment accumulation rates and weathering rates suggesting that rates of landscape change have remained surprisingly constant over the last 10 Ma (Willenbring and Jerolmack, 2016).

The total debris flux for Khumbu decreases steadily downglacier, which indicates a progressive loss of debris along the length of the debris-covered ablation zone and deposition

subglacially (Fig. 2.6). Our estimates of basal deposition reveal that the highest rates are near EBC; however, the subglacial debris thicknesses in Fig. 2.5 reveal that much of the subglacial debris resides beneath the lower part of the glacier where basal deposition rates are at a minimum. Conceptually, we hypothesize that a fraction of the surface debris actively falls into crevasses, tarns, moulins, or other englacial conduits (Gulley et al., 2009), progressively migrates to the glacier bed, and is transported subglacially to the terminus, likely by meltwater. An important consequence of the debris transfer is that the surface of the glacier now has less debris, and hence, less insulation, which promotes more ice melt.

In Section 2.6.1, we determined that contemporary subglacial deposition rates range from 0.6 to 5.0 mm/yr along the glacier. Assuming these values represent the range of rates that can be sustained through the Holocene (10^4 years), the average thickness of debris beneath the glacier would range from 6 to 50 m. Previously, in our analysis of Holocene deposits, we estimated the volume of subglacial debris for Khumbu Glacier to be 0.04 to 0.095 km^3 (Table 1), which corresponds to a width-averaged subglacial debris thickness of 12 to 40 m. The similarity between the subglacial debris thicknesses based on the topographic analysis (Fig. 2.5) and the thickness based on basal deposition rates suggests that debris is currently accumulating under Khumbu Glacier and doing so at a rate that is similar to the Holocene average. Before the Holocene, extensive valley glaciation corresponding to the Periche stages (e.g., Finkel et al., 2003) efficiently transported eroded material downvalley, and the absence of upvalley fans, terraces, and moraines older than the Holocene can be attributed to rapid sediment transfer characteristic of large glaciers (Richards et al., 2004). Following retreat to the current position, tributary and debris flow fans and moraines were deposited as the smaller glacier and lower-runoff rates could not keep pace with

sediment production. Note that contemporary suspended sediment evacuation is ~50x less than the Holocene-averaged sediment production. This, together with evidence that the contemporary glacier is perched on a debris edifice, implies that most of the eroded debris remains within the basin.

2.8 Summary

In view of the structural complexities as well as major climatic changes through the last few million years including the onset of glaciations and several glacial cycles, two surprises emerge from our study: exhumation rates are similar to erosion rates, and they show no significant changes over time periods ranging from 10 to 10^7 years. Taken together with the paleo-elevation evidence, our results suggest a self-organized balance achieved as the surface and tectonic systems mutually adjust to remove rock mass from the crest of the range at roughly the same rate as the rock uplift. Over the last 10^4 years, the bulk of debris produced by erosion remains under and in the vicinity of Khumbu Glacier, suggesting that although erosion rates of the basin do not vary appreciably over time, debris evacuation and transfer down valley is likely be highly variable in time and peak during major glacial advances. The current accumulation of debris beneath the glacier that curtails the accumulation of debris on glacier surfaces is likely widespread in the region, and hence has important implications for estimates of ice volumes, and predictions of future glacier evolution and fresh water resources.

2.9 Supplement

2.9.1 Measurements of fluvial sediment flux

We established rating curves to convert stage measurements to water discharge by measuring depth profiles of flow velocity. We also surveyed repeat topographic profiles of the streambed covering both the stream bank and channel in order to estimate rates of higher discharge using the Manning equation with values for bed roughness guided by our measurements. During monsoon periods, stage and turbidity were monitored continuously at site 1, while stage and suspended sediment concentrations (SSC) were measured twice daily at site 2 (Fig. 2.1). Locals were hired and trained to collect water samples from the stream surface at periods of near minimum (early morning) and maximum (evening) discharge and to photograph the stream to document stage. The measurements of SSC were used to calibrate the turbidity data, which were collected over a longer period and with higher temporal frequency. The suspended sediment discharge (Q_{ss}) is calculated from the product of the SSC and water discharge. We do not account for the increase in sediment concentration with depth, which could be as much as 30% (e.g., Riihimaki et al., 2005), and nor do we account for the fluvial flux of solutes, and corresponding chemical erosion. In another study, the cation denudation rate for catchments occupied by alpine glaciers was greater than the global mean rate but did not exceed rates in nonglacial catchments with similar water discharge suggesting that water flux exerts the primary control of chemical erosion by glaciers (Anderson et al., 1997). During colder periods such as the Last Glacial Maximum (LGM), chemical erosion rates determined from LGM sediments were an order of magnitude lower than that measured from youngest sediments (Anderson et al., 2000). A third, more significant loss of material that is also not considered is the evacuation of

sediments during glacial outburst floods; our estimates should therefore be considered as a lower bound.

Fig. 2.7 summarizes the discharge, SSC and turbidity measurements. Measurements vary widely each summer and year-to-year. In 2011, discharge steadily increases until it peaks in late July and then steadily decreases. In contrast, in 2012, the discharge peaks early in the monsoon season, and subsequently varies around a relatively constant value in early Sept. SSC also peaks in mid-June and then slowly decreases over the rest of the measurement period. SSC measurements in 2011 yielded a mean concentration of 0.10 g/L with a standard deviation of 0.04 g/L. In 2012, the mean concentration was 0.14 g/L with a standard deviation of 0.05 g/L. Assuming little sediment is removed before or after the measurement period, in 2011 and 2012, 570 and 840 m^3 of debris respectively were evacuated (or 10^6 and 1.5 x 10^6 kg assuming a density of 1800 kg/m^3). The amount of sediment evacuated is averaged over the year for the erosion rate; however, we only measured sediment fluxes when they are likely to be significant, during the monsoon. The corresponding erosion rate, 0.01 and 0.02 in 2011 and 2012, respectively, from the suspended sediment flux in this study may miss episodic but high-discharge events and hence is a lower bound of both suspended sediment fluxes and erosion rates.

Figures for Chapter 2

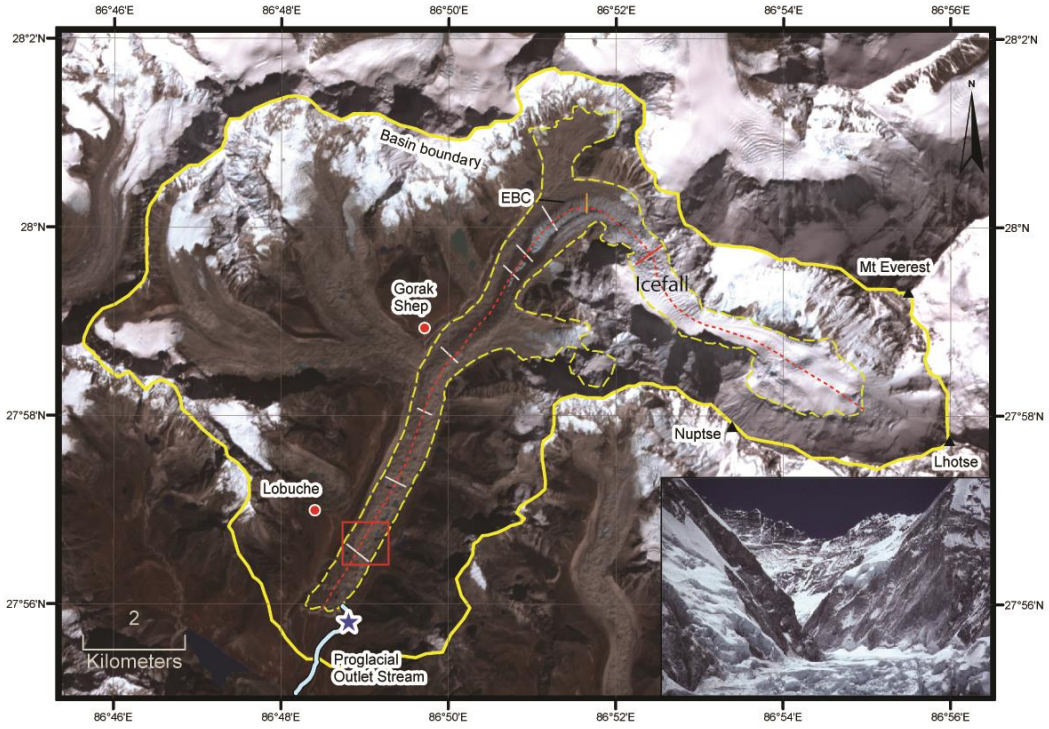

Figure 2.1 – Visual and near infrared band composite satellite image of Khumbu Basin (Aster—3 Oct 2003). Solid and dashed yellow lines outline the drainage basin and the glacier, respectively. Transverse white lines locate the ice-thickness radar surveys (Gades et al., 2000). Red dotted line is the centerline and location of the longitudinal elevation profile in Fig. 2.2. The orange line near Everest Base Camp (EBC) is the start of the longitudinal velocity profile in Fig. 2.2 and the red line is the equilibrium line altitude (ELA) near 5700 m in the icefall (Scherler et al., 2011). Red square over the lower ablation zone defines area covered in Fig. 2.4. The blue star shows where suspended sediment flux was determined in the proglacial outlet stream. Inset shows the massive headwalls surrounding the accumulation zone of the glacier and extreme relief above the glacier (Image courtesy of A. Gillespie).

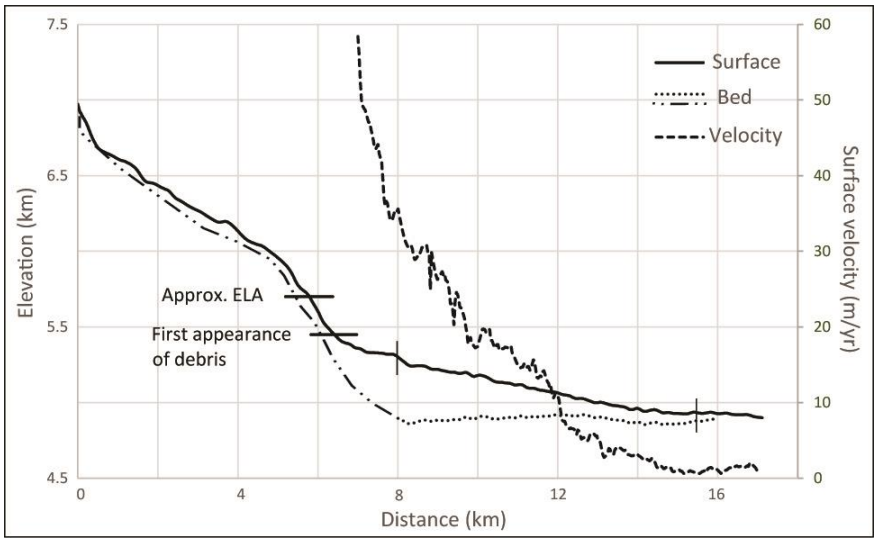

Figure 2.2 – Longitudinal profiles of the surface and bed elevation profiles and surface velocities (right-hand axis) of Khumbu Glacier. In the lower half of the glacier, shown as dotted line between 8-16 km, the glacier bed is interpolated between 7 cross-profiles of ice thickness (Gades et al., 2000) and between 0-8 km, the dash-dot line, it is modeled using profiles of surface slope and velocity derived from remote sensing data, and by assuming basal shear stress of 1 bar. Surface velocities are derived by using intensity feature tracking over a period of 4.5 months [courtesy of M. Braun]. The vertical lines at km-8 and km-15.7 are the start and end positions of Figs. 2.3 and 2.6.

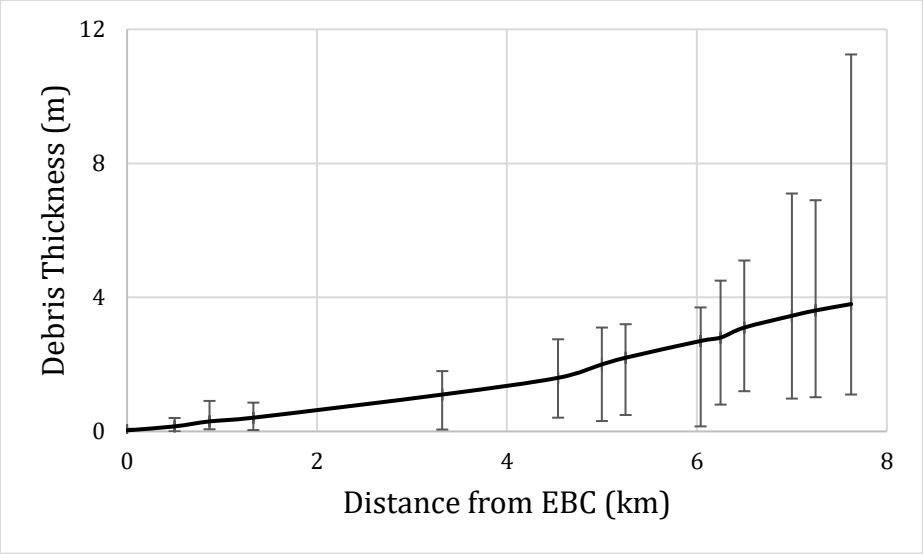

Figure 2.3 – Downglacier variation in mean thickness of surface debris. The horizontal axis, distance down glacier, starts at Everest Base Camp, where debris begins to accumulate at the surface. Error bars represent the range in debris thicknesses, where measurements are available, binned into 250 m increments along the glacier surface.

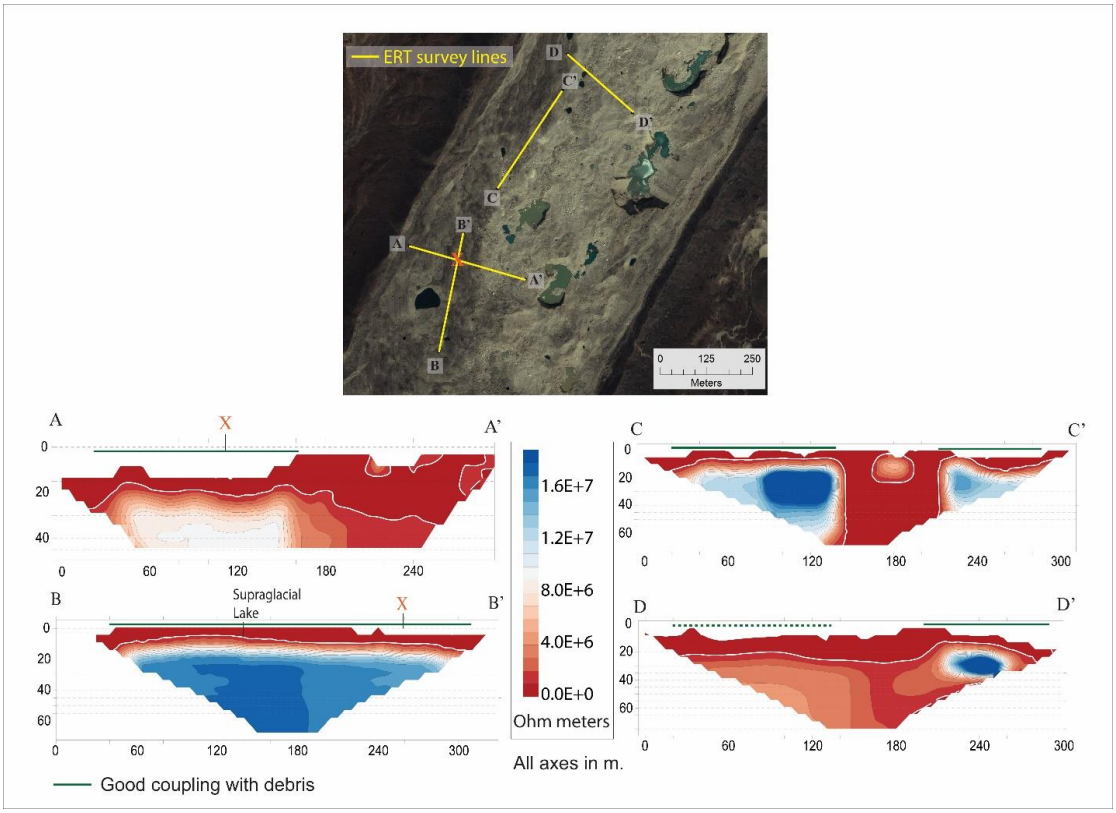

Fig. 2.4 – Electrical resistivity tomography (ERT) profiles along survey lines shown in the top image, the location of which is shown in Fig. 2.1. Horizontal and vertical axes are in meters. All images use the same color scheme; blue colors denote very high resistivity. Resistivity values of 10^6 Ω m marked by white lines likely correspond to the boundary between surface debris and glacial ice below. Solid green lines above each survey indicate regions where electrode coupling with the surface debris was adequate; dashed green lines indicate regions of high uncertainty; regions with no line are those where electrode-debris coupling was inadequate and data are uninterpretable.

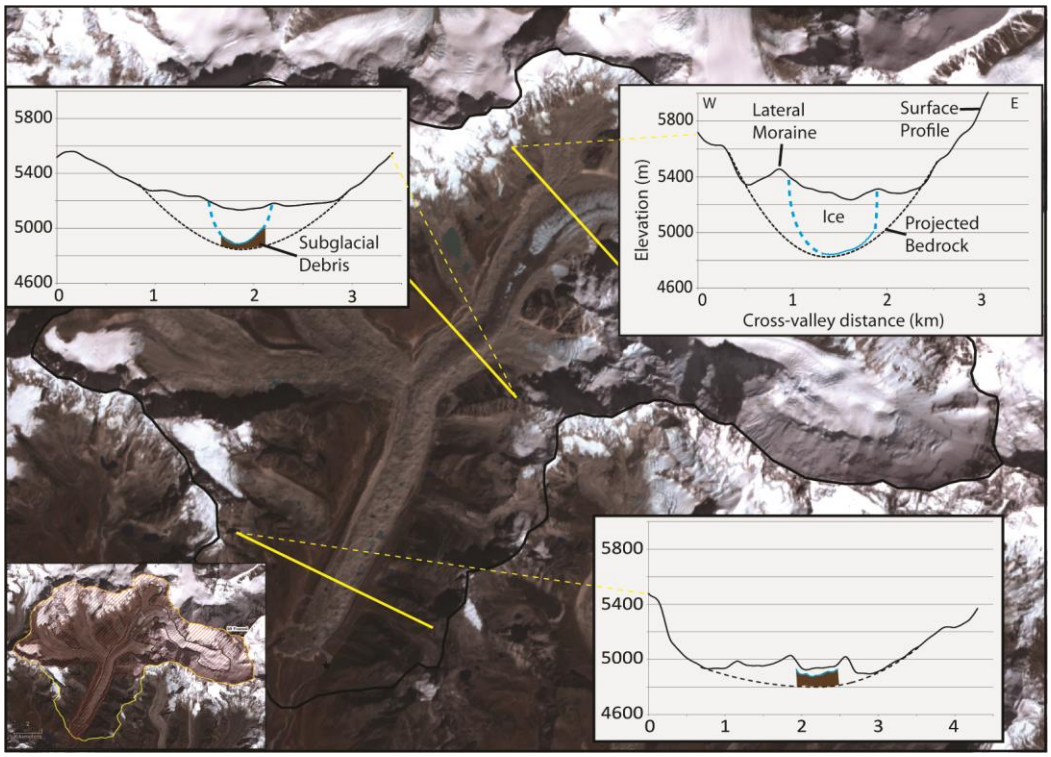

Fig. 2.5 – Surface and subsurface cross-sections from which the volume of sediment stored within the basin was estimated. In the cross-sections, which run West to East, the solid black line is the current surface, blue line is the glacier bed (solid are measurements (Gades et al., 2000) and dashed are extrapolated), shaded brown region represents subglacial sediment/debris.

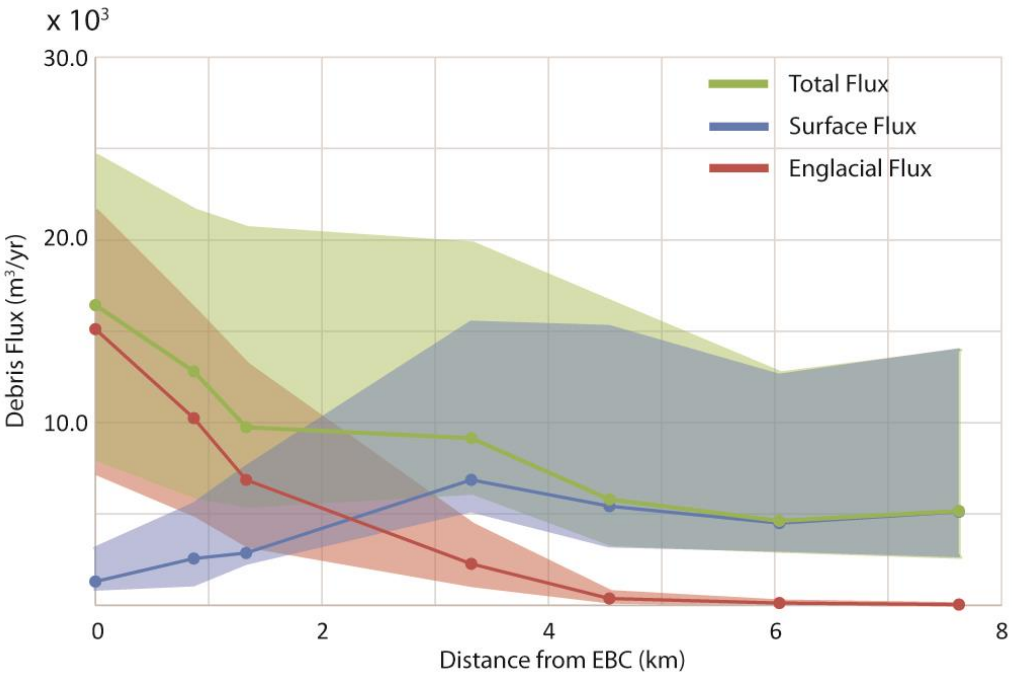

Fig. 2.6 – Surface, englacial and total debris fluxes downglacier beginning near EBC (the uppermost radar profile in Fig. 2.1). The shaded regions represent uncertainties in the data. The flux calculation at 7.7 km corresponds to the radar profile ~ 2 km up from the terminus. Near EBC, total debris flux is dominated by the englacial flux, but at 2.2 km, contributions from the englacial- and surface-debris fluxes are similar. By 4.5km, the surface-debris flux dominates; the englacial-debris flux is small because of the combination of low depth-averaged velocities (<5m/yr) and thin ice (<100 m).

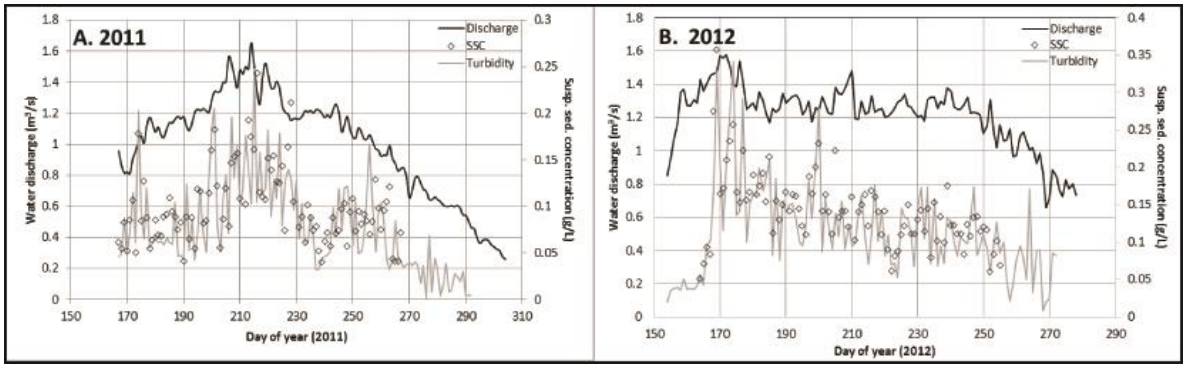

Fig. 2.7 – Time series of daily-averaged stream discharge (black line), SSC (open diamonds) and turbidity (gray line) measurements for the summer monsoon (late May to Sept) in both 2011 (A) and 2012 (B). Turbidity was converted to SSC in g/L using the rating curves developed in this study. Day 150 = May 10th, and 290 = Oct 17th.

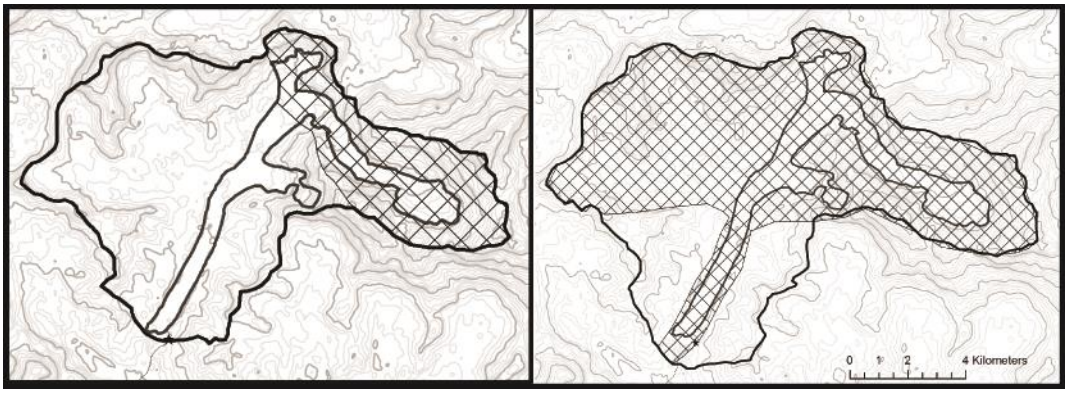

Fig. 2.8 – Spatial extents of basin areas for erosion rates. Left: contemporary area ~26.5 km^2; Right: Holocene area ~70 km^2.

Tables for Chapter 2

Table 2.1 – Observations of englacial sediment concentrations

Table 2.1. Observations of englacial sediment concentrations

Glacier	Location/Type	Concentration kg/m^3	Source
Muir	AK/M.E.	16.8 ± 3	(Hunter et al., 1996)
Margerie	AK/M.E.	8 ± 8	(Hunter et al., 1996)
Grand Pacific	AK/M.E.	2.5 ± 2.4	(Hunter et al., 1996)
Raikot	Pak/Alpine	2.13	(Gardner and Jones, 1993)
Kviarjokull	Ice/Outlet	5.2	(Swift et al., 2006)
W. Washawapta	BC/Cirque	0.7 (0.0 - 6.6)	(Sanders et al., 2013)
W. Washawapta	BC/Cirque	0.02 (0.0 - 3.2)	(Sanders et al., 2013)

where AK = Alaska, Pak = Pakistan, Ice = Iceland, BC = British Columbia
M.E. = marine ending

Table 2.2 – Basin-wide debris volume estimates

Table 2.2. Basin-wide debris volume estimates

Domain	Volume (km^3)	
	Low	High
Surface debris	0.03	0.04
Englacial debris	0.01	0.03
Subglacial debris	0.1	0.2
Lateral moraines	0.2	0.3
Terminus debris edifice	0.1	0.2
Tributary glaciers	0.04	0.1
Fluvially evacuated	0.006	0.008

Chapter 3: Climate and debris controls on the evolution of debris-covered glaciers on time scales of 10 to 10^4 years examined for Khumbu Glacier, Nepal.

3.1 Abstract

We use data and observations from Khumbu Glacier to develop a relationship between the rate of ice melt and debris thickness for the large range of debris thickness and rough thermoskarst surface representative of Himalayan glaciers. We implement this relationship in a numerical glacier model using records of the Little Ice Age and Last Glacier Maximum extents of Khumbu Glacier as stable reference states to validate the model under steady-state conditions, and to serve as the initial state in transient models used to study the current glacier recession and future evolution. Model results quantify both the damping effect on ablation (melting) of a continuous surface layer of debris layer and the acceleration of melting by thermokarst processes that disrupt the surface debris layer and form a network of conduits below the surface. Comparison between observed volume changes, based on changes in elevation from the moraine to the current glacier surface, and model results show that our model adequately accounts for the ~29% volume of ice lost since the end of the LIA to present. Furthermore, our model suggests that the glacier will continue to thin, resulting in a ~6% volume loss from present over the next 100 years, even if the current climate remains unchanged, which bears directly on fresh water resources. Our work builds on significant modeling studies on debris-covered glaciers by Rowan et al. (2015) and Anderson and Anderson (2016). We differ in that we specifically calibrate our model using extensive direct

observations of Khumbu Glacier, many of which are new, and focus our attention on the treatment of ice melt under thick debris to elucidate the past, current and future states of debris-covered glaciers.

3.2 Introduction

The response of glaciers to climate change is of fundamental scientific interest, and has important practical consequences, including fresh water availability, global sea-level change, and environmental hazards (e.g., Richardson and Reynolds, 2000; Immerzeel et al., 2010). A significant threat to Himalayan communities is moraine-dammed lakes that form following glacier recession or subsidence (Bolch et al., 2008a; Benn et al., 2012; Thompson et al., 2012). Recent studies show that the areal extent of glaciers in the Everest region, including many with a thick debris cover, decreased 5% during the second half of the 20th century (Bolch et al., 2008b; Salerno et al., 2008) and are also thinning actively. For Khumbu Glacier, the rate of thinning across the ablation area averaged 0.38 ± 0.07 m a^{-1} between 1970 and 2007 (Bolch et al., 2011). Predicting the future of Himalayan glaciers and, hence, assessing the societal consequences is especially challenging due to the presence of surface debris, which strongly influences glacier mass balance and evolution (e.g., Scherler et al., 2011, Anderson and Anderson, 2016).

In order to shed light on glacier changes in the Khumbu region, and by extension in similar settings along the Himalaya and elsewhere, several researchers have used numerical models to examine the current state of the glacier and its probable evolution. Naito et al. (2000) coupled mass balance, which they modified to represent simply the protective effect of debris, and glacier flow to investigate shrinkage of the Khumbu between 1978 and 1999. They predicted that the lowest part of the glacier would stagnate and eventually decouple

from the upper glacier, which could lead to the development of a large and potentially hazardous glacial lake. Shea et al. (2015) used a glacier mass balance, parameterized for both clean and debris-covered glaciers, and ice-flow model to examine historical change of glaciers in the Everest region from 1961 to 2007 and assess future changes. They concluded that glaciers may lose between 73 to 96% of their total volume due to sustained warming by the year 2100.

Rowan et al. (2015) used the integrated second-order shallow ice approximation (iSOSIA) model (Egholm et al., 2011) to investigate the response of Khumbu Glacier to recent and future climate change. Their 3-D model coupled ice flow with debris evolution, and focused on interactions between the debris cover and mass balance. Model simulations quantified the imbalance of Khumbu Glacier with the current climate, which is evident from the current and post-Little Ice Age (LIA) thinning of the Khumbu. They suggest that even without a further change in climate, Khumbu Glacier will continue to respond to post-LIA warming until AD2500. Furthermore, they predicted a loss equivalent to 8-10% of the present-day volume by AD2100 and detachment of the debris-covered tongue from the accumulation area of the glacier before AD2200. It is worth noting that their estimate of glacier shrinkage by AD2100 is an order of magnitude less than that predicted by Shea et al. (2015). In another study, Anderson and Anderson (2016) developed a transient 2-D model to investigate debris cover and glacier evolution for generic debris-covered glaciers, using Khumbu Glacier as a case example. Unlike Rowan et al. (2015), they focus on improving understanding of glacier evolution solely in response to changes in debris cover; in this initial modeling phase, they do not consider the effects of climate change. Among many important findings, model simulations show that a high input of debris to the glacier surface greatly

increases glacier lengths relative to debris-free glaciers responding to the same steady climate, which is consistent with observations of debris-covered glaciers existing entirely below the snow line (Konrad and Humphrey, 2000; Scherler et al., 2011). These numerical models provide insight into the response of Khumbu and other debris-covered glaciers and are a foundation for future studies.

In this paper, we build on these early studies and address unexpected observations outlined by Kääb et al. (2012) suggesting that thinning of debris-covered glaciers over a 5-year span was not statistically different from thinning of relatively debris-free (clean) glaciers; herein, we refer to these results as the debris-covered glacier anomaly. According to the authors, the long-recognized insulating effect of debris acts on local scales of continuous cover, but not over the scale of the entire debris-covered tongue where rapid ice loss continues due to the thermokarst processes. At Khumbu, the rough thermokarst surface and very thick cover layer of debris likely reflect this behavior, providing a rare opportunity to examine it in detail because of the relative wealth of data available for this glacier. Using existing and new observations of thinning rates, surface velocity, and the thickness of both ice and debris, we quantify a relation between debris thickness and the rate of ice melting. The relation reflects processes occurring on a scale larger than the distinct thermokarst roughness elements, which include depressions and tarns 10-100 m in diameter and intervening ridges with exposed ice on steep slopes; thus we name it the “large-scale melt rule”. We assess the rule in an ice-flow model, which is validated with new and existing data from Khumbu Glacier. An often-overlooked result evident from these and other datasets is that the ice is dynamically thickening in the ablation zone, hence the melting rate must exceed the remotely measured thinning rate. Herein, we will show that the melt rate exceeds

the thinning rate on Khumbu Glacier by more than an order of magnitude over much of the debris-covered area. We stress that the representation of the influence of surface debris on ice melt strongly impacts the modeled long-term evolution of both the glacier and debris; a conclusion shared by other studies (e.g., Scherler et al., 2011; Rowan et al. 2015; Anderson and Anderson, 2016). Finally, we predict the future state of the glacier using a model validated through observations of the modern glacier and from known, former glacier states during LIA (~0.15 ka) and the regional Last Glacial Maximum (LGM; ~18 ka). These periods of relative glacier stability provide useful reference states for assessing glacier models because glaciers were closer then to being in balance with the climate than during the current period of active recession.

3.3 Khumbu Glacier

The 18 km-long glacier descends from an elevation of ~7100 m, directly below Mt. Everest, to its terminus at 4900 m. It covers ~17 km^2 within a ~90 km^2 basin (Fig. 3.1). Sheer rock faces that surround the accumulation zone shed snow and ice avalanches onto the glacier. A steep, heavily crevassed icefall connects the accumulation zone with the relatively gentle debris-covered ablation zone that extends to the terminus. The modern equilibrium line altitude (ELA) is within the icefall at about 5700 m (Scherler et al., 2012); whereas, at the end of the LIA, it was estimated to be 5479 ± 120 m (Kayastha and Harrison, 2008).

The wealth of published and unpublished data about Khumbu Glacier makes our study possible. The data include: 1) *Meteorological data*: A high-altitude (5050 m a.s.l.) automatic weather station (AWS) has recorded hourly meteorological observations near Khumbu since 1990 (Bollasina et al., 2002). The data include air temperature and precipitation, and when included with other AWS, the temperature gradient with elevation (-

5.8°C km^{-1}; Scherler, 2014). Seasonal temperature and precipitation observations include: Winter) low average monthly temperature (-8°C) and light precipitation (less than 2% of annual amount); Summer) warmer temperature (3.1°C) and intense precipitation (87% of annual amount) (Tartari et al., 1998). 2) *Ice thickness*: seven ice-penetrating radar profiles measured in 1999 across the ablation region define its transverse geometry. The maximum ice thickness decreased from 450 m near Everest Base Camp (EBC) to less than 20 m about 2 km from the present terminus (Gades et al., 2000); it is not known well beyond this location. However, in most of the lower reach of the glacier, the difference between the surface of Khumbu Glacier and the valley floor at the outer base of the lateral moraines exceeds the ice thickness considerably indicating that the current glacier bed is perched well above the valley floor directly adjacent to the moraines (Fig. 3.1C). 2) *Ice thickness changes*: In addition to the satellite-based studies of active thinning outlined in the introduction, the local elevation difference between the top of the most recent (LIA) lateral moraines and the current glacier surface shows nearly 100 m of glacier thinning in the center of the ablation area while the terminus and EBC region have been relatively stable. 3) *Surface velocity*: repeat sets of satellite imagery have yielded estimates of surface velocity that are nearly continuous spatially; we use these to calculate ice and debris fluxes and utilize them as a modern baseline from which to compare sparse historical field measurements and model results (Kodoma and Mae, 1976 and Nakawo et al., 1999). 4) *Distribution of surface debris:* Early studies showed that the thickness of the surface debris varies from less than 0.1 m directly below the icefall to more than 2 m near the terminus (Nakawo et al., 1986). Our field geophysical measurements and observations show the debris to be thicker, averaging ~5 m near the terminus (Chapter 2).

3.4 Model

In this section, we introduce the ice-flow model, melt-rate relationships, and boundary conditions used to investigate the evolution of Khumbu Glacier. We focus on the debris-covered ablation area of the glacier, and begin by considering the conservation of ice and debris, and its relationship to changes in the glacier and debris volumes over time. Then we introduce the numerical glacier flow model, the boundary and initial conditions, and a new representation of the rate ice melt is under debris for a much broader range of debris thickness than addressed in previous studies.

3.4.1 Conservation of ice and debris

We begin with a series of conservation equations that quantitatively link the dynamics and other properties of ice and debris, and serve as the basis for our flow-band model along the glacier centerline. Conservation of ice is:

$$\frac{\partial H}{\partial t} = \dot{b}(z,\ D_s) - \frac{1}{w(x)}\frac{\partial (Q_i)}{\partial x}, \qquad \text{(Eq. 1)}$$

where H is glacier thickness, t is time, x is the downvalley distance, $\dot{b}$ is the net mass balance rate as a function of elevation, z, and surface debris thickness, D_s, w is glacier width, and Q_i is ice flux:

$$Q_i = \bar{U} w H, \qquad \text{(Eq. 2)}$$

where $\bar{U}$ is the depth-averaged glacier velocity. In the ablation zone of Khumbu, assuming negligible accumulation, the net mass balance rate approximates the ice-melt rate. This assumption is reasonable for Khumbu Glacier, as discussed later. The ice-melt rate is then the sum of the surface subsidence rate, $\frac{\partial H}{\partial t}$ assuming the glacier bed is stable, plus the vertical

component of ice motion (i.e., the emergence velocity), positive being upward; it scales with the ice convergence (last term in Eq. 1).

Similarly, a conservation equation for the debris parallels Equation 1 for the ice, taking the form:

$$\frac{\partial D_{Tot}}{\partial t} = \frac{(\phi-1)}{w}\frac{\partial (Q_{TD})}{\partial x} - S(x) - F(x), \qquad \text{(Eq. 3)}$$

where D_{Tot} is the total effective debris thickness, which includes surface and englacial debris , ϕ is the debris porosity, $S(x)$ is a debris sink term, and F represents the rate of fluvial evacuation of debris by the proglacial stream. The last two terms on the right side are critical; without them, the glacier will not reach a steady-state length. Instead, rapidly thickening debris at the glacier terminus will effectively stop ablation forcing the glacier to advance. Konrad and Humphrey (2000) conceptually introduced a debris sink term at the glacier terminus, which involved debris raveling off the glacier terminus as exposed ice at the glacier toe melted underneath, undercutting the debris. Anderson and Anderson (2016) parameterized the removal of debris at the glacier terminus as a function of the debris thickness and clean-ice mass balance rate at the terminus. They found that the steady-state glacier length, as well as if it even reached a steady state, was dependent on the debris flux off the glacier. The representation of the sink term in our model is discussed in section 3.5.3.

The total debris flux, Q_{TD}, comprises both debris advected along the surface, Q_s, and within the glacier, Q_{en}:

$$Q_{TD} = Q_s + Q_{en}, \qquad \text{(Eq. 4)}$$

where

$$Q_s = U_s w D_s \text{ and } Q_{en} = \bar{U} w H C_d \qquad \text{(Eq. 5)}$$

The variable U_s is the surface velocity and C_d is the average volumetric concentration of debris in the ice. Inserting Equations 4 and 5, into Equation 3 leads to:

$$\frac{\partial D_{Tot}}{\partial t} = \frac{(\phi-1)}{w}\frac{\partial}{\partial x}(U_s w D_s + \bar{U} w H C_d) - S(x) - F(x), \qquad \text{(Eq. 6)}$$

Eq. 6 expresses how the effective debris thickness changes over time, in response to the glacier dynamics and debris losses. In our model, we assume that the englacial debris is sourced from mass wasting and headwall erosion occurring on the rock slopes surrounding the accumulation zone and extending under the glacier. In the ablation zone, mass wasting is limited to the marginal glacier region away from the centerline and the basal-debris supply is a relatively minor component of the effective debris load (Gustavson and Boothroyd, 1987).

The surface debris thickness increases with time as debris melts out of the ice at a rate $\dot{m}$, which is a sensitive function of debris thickness, and with the convergence of the flux of debris advected on the glacier surface. The conservation of surface debris is expressed as:

$$\frac{\partial D_s}{\partial t} = \dot{m}(z,\, D_s)C_d - \frac{(1-\phi)}{w}\frac{\partial (U_s\, D_s w)}{\partial x} - S(x) - F(x) \qquad \text{(Eq. 7)}$$

In this analysis, we distinguish between the net mass balance term, $\dot{b}$, used in Eq. 1 and the melt-rate term, $\dot{m}$, used in Eq. 7 that neglects accumulation and other forms of ice ablation. Sublimation is most likely negligible relative to melting at the relatively high surface temperatures that prevail over the lower reach of the glacier. Moreover, in the upper ablation zone, scattered debris promotes melting by absorption of solar radiation (Inoue, 1977). Annual accumulation in the ablation zone is neglected. Although winter snowfall often covers the entire glacier, its overall magnitude is small relative to the precipitation during the monsoon, which falls as snow at high altitudes and as rain at lower altitudes due to the high summer temperatures (Inoue, 1977).

3.4.2 Glacier flow model

Our 1.5-dimensional central flowband model uses the finite-difference method to discretize our domain. In the solution, ice thickness is evaluated at each grid center, and ice flux is evaluated across each grid edge. The depth-averaged horizontal velocity comes from the shallow-ice approximation (SIA), which applies to cases where the ice thickness is smaller than the characteristic length scales over which thickness changes significantly (Fowler and Larson, 1978; Hutter, 1981). The SIA is adequate for understanding the behavior of the slow-moving, debris-covered ablation area of Khumbu Glacier, which is relatively uniform in width, surface gradient and velocity. The depth-averaged velocity, $\bar{u}_{def}$, attributed to internal ice deformation is:

$$\bar{u}_{def} = \frac{2A}{n+2}(f\rho_i g \sin\alpha)^n H^{n+1} \qquad \text{(Eq. 8)}$$

where A and n (= 3) are flow law parameters. As in Anderson and Anderson (2016), ice throughout the ablation area is treated as temperate, which is consistent with the abundance of surface water on the glacier during much of the year and with model results for the nearby East Rongbuk glacier that show the existence of an extensive temperate zone in the ablation area (Zhang et al., 2013). Accordingly, A is set at the standard value of 2.4 x 10^{-24} Pa^{-3} s^{-1} (Cuffey and Paterson, 2010). The timestep for ice flow and debris evolution is 0.01 yr. The shape factor, f (= 0.8) accounts for lateral drag for an idealized parabolic glacier cross-section (Cuffey and Paterson, 2010). ρ_i is ice density, g the acceleration due to gravity, and α the glacier surface slope. We do not include an explicit parameterization for basal sliding; instead, we solve for the rate of sliding as the residual between the observed surface velocity and the velocity due to internal ice deformation. At East Rongbuk Glacier, basal sliding was

found to be a minor contribution to the mean annual ice velocity; rather, flow is dominated by internal deformation (Zhang et al., 2013).

3.4.3 Boundary Conditions

Additional model inputs include surface and bed topography, which are derived from analyses of modern digital elevation models (DEMs). A 15 m-resolution DEM is used to define the current glacier geometry, as well as the geometry of former glacier extents. Bed topography was determined from ice thicknesses in the lower ablation zone, which were interpolated between measurements at seven cross-glacier sections (Gades et al., 2000). Ice thickness, and hence bed topography, in the upper reaches was estimated from measurements of surface slope and assuming a constant value, 10^5 Pa, for the basal shear stress, which is consistent with values we calculate for locations where the ice thickness is known. Directly below the ice-fall, the ice flux is defined as the integrated net mass balance profile upglacier. The debris flux, which is completely englacial because of the lack of significant surface debris upglacier of this location, is the product of the ice flux and the englacial volumetric concentration of debris, which is taken to be constant. In the model, ice flux is zero at the headwall and ice thickness vanishes at the terminus.

To validate and calibrate the model for Khumbu Glacier in light of the regional climate, we first consider steady states, and use well-developed moraines and related landforms and deposits that record past glacial extent and thickness under climate conditions closer to those required to sustain the glacier in a relatively stable state than at present. The distribution of the glacial landforms and timing of past glaciations along the Dudh Koshi valley have been investigated since the 1970s, as reviewed by Owen et al. (1998). Much debate therein arguably reflects potential ambiguities in the interpretation of landforms, but

based on optically stimulated luminescence (OSL) dates of glacial deposits, Richards et al. (2000) assigned the following ages to past glacial advances: ~18 ka (LGM), ~10 ka (Holocene), and ~1 ka. The OSL method determines the time elapsed since a sample was exposed to daylight and assumes that quartz grains are 99% reset after an extremely rapid (10 s) exposure to sunlight (Richards et al., 2000). The OSL ages are supported by cosmogenic radionuclide (CRN) ^{10}Be surface exposure dates performed on moraines in the region; in the analysis several boulders were dated to check reproducibility and to assess the possibility of CRN inheritance (Finkel et al., 2003). Here, we use the end of the LIA (~0.15 ka) as our reference period, instead of the timing of the peak LIA roughly estimated to be 0.5 ka (Finkel et al., 2003), as to permit focusing on the subsequent glacier shrinkage. The timing, ~0.15 ka, corresponds to photographs of Jannu Glacier in eastern Nepal that show the glacier surface close to the crest of the lateral moraines (GlacierWorks, 2016). Furthermore, a high-resolution ice core in Dasuopu, Tibet and tree-ring records from Nepal both indicate a warm interval beginning in *ca* 1870—1890 (Thompson et al., 2000; Cook et al., 2003). We acknowledge the uncertainties in characterizing mountain meteorology as ice-core records from nearby East Rongbuk Glacier show a decrease in precipitation up to the late 1800s to early 1900s followed by an increase and, finally, another decrease in the late 1900s (Kaspari et al., 2008).

The modern terminus of the glacier roughly coincides with the upglacier end of the LGM moraines and the lower end of the LIA moraines (Fig. 3.1). Curiously, based on 2003 DEM, the LGM moraine surface would be nearly 200 m lower in elevation than the crest of the LIA moraine if slightly extrapolated upvalley. The LIA lateral moraines on both sides of the glacier are traced in Fig. 3.1, which also shows the prominent LGM left-lateral moraine

(dashed red line in Fig 3.1a) that extends continuously along the east side of the valley for ~5 km from the terminus to beyond the Imja Khola tributary. This LGM moraine is dated to the Periche II glacier succession at 16 ± 2 ka (Finkel et al., 2003), which is within the range of the timing of the LGM retreat of glaciers in Tibet (Clark et al., 2009). The early Holocene-aged moraine is less prominent, but has been located near the base of the contemporary terminal moraine, and suggests that the terminus has remained in the same position for 10^4 years (Richards et al., 2000).

3.4.4 Glacier mass balance in the absence of debris

In the model, the net mass balance rate is approximated as a simple linear function of elevation, $\dot{b}_z$, until a maximum, $\dot{b}_z^{max}$, is reached:

$$\dot{b}_z = \frac{d\dot{b}_z}{dz}(z_{ice} - ELA) \; or \qquad \text{(Eq. 9)}$$

$$\dot{b}_z = \dot{b}_z^{max},$$

where $\frac{d\dot{b}_z}{dz}$ is the mass-balance gradient, and z_{ice} is the ice elevation. This approach has been used to represent the mass balance of other high altitude Himalayan Glaciers, including the nearby glacier AX010, which is about 30 km SW of Khumbu Glacier (Harper and Humphrey, 2003; Adhikari and Huybrechts, 2009; Anderson and Anderson, 2016). For each ice-flow model, we examined mass balance gradients ranging from 0.005 to 0.015 a^{-1}; here we show only model results with $\frac{d\dot{b}_z}{dz} = 0.01$ a^{-1}, which is similar to the gradient for glacier AX010, and $\dot{b}_z^{max}$ is 2 m a^{-1} (WGMS, 2005).

3.4.5 Dependence of surface melt rate on surface debris thickness

The melt rate of ice beneath debris has been measured directly in the field at prepared plots of known debris thickness (e.g., Ostrem, 1959; Nakawo and Young, 1981; Reznichenko et al., 2010) and at natural sites with in situ surface debris (e.g., Inoue and Yoshida, 1980; Mattson and Gardner, 1990; Kayastha et al., 2000; Nicholson and Benn, 2006). Lundstrom (1992) compiled much of the data, including measurements from Khumbu Glacier, and established one of the first relationships between the rate of ice melt and debris thickness; however, the data are limited to at most a few decimeters in thickness.

Previous theoretical studies have simply parameterized the influence of debris on surface melt rates as:

$$\dot{m}(D_s) = \dot{b}_z \exp\left(\frac{-D_s}{D_*}\right) \quad \text{(Anderson, 2000)} \qquad \text{(Eq. 10)}$$

or as:

$$\dot{m}(D_s) = \dot{b}_z \left(\frac{D_*}{D_* + D_s}\right) \quad \text{(Anderson and Anderson, 2016)} \qquad \text{(Eq. 11)}$$

where $\dot{b}_z$ is the melt rate for clean ice, reflecting local environmental conditions, and D_* is a fall off length scale, (~0.1 m); it represents the thickness of debris under which the melt rate is 1/e of the bare-ice rate (Anderson, 2000). Eq. 9 sets the clean-ice melt rate in Eq. 10. In the formulation by Anderson (2000), the melt rate decreases exponentially with increasing debris thickness and nearly vanishes under a few decimeters of debris and yet at Khumbu Glacier, where debris thickness averages ~3-6 m near the glacier terminus, the glacier is actively thinning at rates of 0.2 to 0.4 m a^{-1} (e.g., Bolch et al., 2011). In Anderson and Anderson (2016), the melt rate decreases in a hyperbolic fashion with increasing debris thickness (Eq. 11), which approaches zero melt less rapidly than the exponential formulation.

The type of insulation represented by Eqs. 10 and 11, (herein **local-melt rule**) are appropriate locally where debris cover is continuous and uniform. The local-melt rule does not apply to larger spatial scales for rough glacier surfaces with discontinuous surface debris, where ice-melt is enhanced by thermokarst activity. To account for these cases, we have developed a **large-scale melt rule** that pertains to domains larger than the size of individual thermokarst roughness elements (ice cliffs, tarns & crevasses).

The **large-scale melt rule** uses the conservation of ice, Eq. 1, and relevant data from Khumbu Glacier. We approximate the ice-flux divergence as finite differences in ice flux (in and out) for each of the six glacier zones of the ablation area of Khumbu Glacier (Fig. 3.1); the variables for each zone are summarized in the supplement (Table 3.2). Surface velocities derived from feature tracking (FT- data courtesy of M. Braun, 2012) and ice-thickness from ice-penetrating radar surveys were used to calculate the depth-averaged velocity. For the lower two km of the glacier, we augment the FT velocities with repeat GPS measurements at nine sites.

3.5 Results

We begin by introducing the large-scale melt rule, which provides a quantitative framework to investigate the debris-covered anomaly enigma suggested by Kääb et al. (2012). Then we present results of a repeat GPS survey on Khumbu. Next, we describe and estimate the debris sink term, which differs from other models (e.g., Anderson and Anderson, 2016). The preceding results are incorporated into a numerical model, which begin as a simulation of the steady-state glacier. For this state, we use inferred LIA environmental conditions rather than the modern conditions because the modern glacier is far from being in equilibrium with the present environment. We gain further confidence in our model by

simulating the well-known extents of the LGM glacier. In the model, the climate forcing is introduced by variations in the local net mass balance, which can be imposed by assuming either a balance shift or an ELA shift. Using the LIA-optimized simulation as the initial condition, we explore the response of Khumbu Glacier to environmental change by raising the ELA to an elevation consistent with published values of the contemporary ELA (Richards et al., 2000; Owen et al., 2009; Asahi, 2010). Raising the ELA decreases the area of the accumulation zone and, hence, the ice flux through the ELA. We consider the sensitivity of the modeled behavior by showing results for cases using the conventional local-melt rule and for cases using the large-scale melt rule.

3.5.1 Large-scale melt rule

Within the ablation zone, the ice-flux convergence causes positive emergence velocities, but the upward movement is more than offset by melting to yield the modern surface thinning rates shown in Fig. 3.2 (values in Table 3.2). Hence, the actual melt rates are larger (i.e., more negative mass balance) than the observed thinning rates (e.g., Bolch et al., 2011) through the ablation zone.

The rate of ice melt in Fig. 3.2 directly leads to the large-scale melt rule. For the formulation of the rule, the ice-melt rate is related to the corresponding debris thickness (Fig. 3.3). For use in the numerical models, we then parameterize the curve using a fit that has the same form as Eq. 11:

$$\dot{m}(D_s) = \dot{M}\left(\frac{D_*}{D_* + D_s}\right) \qquad \text{(Eq. 12)}$$

where the coefficient $\dot{M}$ has a constant value of 4.7 m a^{-1}; the same value as the average melt rate measured by Kayastha et al. (2000) for ice melt on debris-free ice at EBC. D_* is 0.25 m, which is greater than the 0.165 m value used by Anderson and Anderson (2016). As with

Anderson and Anderson (2016), we neglect the melt-amplifying effects of very thin debris. For comparison, Fig. 3.3 includes the melt-rate rules used in Anderson (2000) and Anderson and Anderson (2016) and the melt-rate curve and data used by Lundstrom (1993). To ease comparison, we use a constant value for the clean-ice melt-rate term in Eqs 10 and 11, which is set to the average clean-ice net mass balance of -3.0 m a^{-1} of nearby Changri Nup Glacier (Vincent et al., 2016).

3.5.2 Modern dynamics at the glacier terminus from GPS

Low velocities near the terminus hamper assessment of remotely sensed measurements of flow and surface thinning. Hence, we augment satellite measurements with GPS measurements of large boulders at the glacier surface that can safely be assumed to move with the surface ice (Fig. 3.1B). Over a three-year interval, we made repeat GPS measurements at sites along the glacier and used kinematic post-processing methods to derive surface velocity vectors. We chose stable, mostly flat boulders over 1.5 m in diameter as measurement sites. The average distance between sites and a local base station was 0.75 km and the occupation time was 1 hr. Surface velocities show motion near the terminus (Fig. 3.4): vertical velocities are negative at all locations except for the southernmost site. That is, although the emergence velocity is positive (Fig. 3.2), with one exception, large boulders on the glacier surface are subsiding, suggesting significant ice loss and conduit collapse well below the surface.

3.5.3 Debris Sink

As described before, the absence of a debris sink prevents a steady-state solution (Konrad and Humphrey, 2000). In other modeling studies, a debris sink term is included at

the glacier toe to remove a prescribed amount of debris from the glacier surface. In Anderson and Anderson (2016), the term is dependent on the local melt rate, which parallels the conceptual model of Konrad and Humphrey (2000); however, at Khumbu, a massive infilling of debris surrounds the toe and effectively shields the glacier from melt processes that are dependent on local air temperatures and insolation (Fig. 3.1).

At Khumbu, the availability of key datasets allow us to explore an alternate debris sink, by enabling the calculation of the change in total debris flux along the glacier. In Fig. 3.5, the total debris flux is shown at each of the seven locations where ice thickness is known. The distinct downglacier decrease in the total debris flux reflects a progressive loss of debris from the glacier. Assuming that significant change in the volume of sediment stored in the interior of the glacier is unlikely, this debris flux decline implies that debris is actively accumulating under the glacier. The rate of change in the total effective debris thickness can be quantified from the divergence of the total debris flux (Eq. 3); this change was approximated as the ratio of the change in debris flux measured at two cross-sections, $Q_{up} - Q_{down}$, to the distance between the defining sections, Δx (Fig. 3.1). Where Q_{up} is the upglacier location. The rate of basal deposition along the glacier, $S(x)$, is:

$$S(x) = \frac{1}{w(x)} \frac{Q_{up} - Q_{down}}{\Delta x} \qquad \text{(Eq. 13)}$$

For the debris sink/source analysis, the glacier was subdivided into six zones (Fig. 3.1), each extending across the width of the glacier. For all zones, the rate at which debris is removed from the glacier and presumably added to the bed ranges from -0.05 to 5 mm a^{-1} (Fig. 3.5). Along the glacier, basal deposition is highest in the three upper glacier sections and steadily decreases downglacier to a minimum value near the terminus (Fig. 3.3).

The effectiveness of the debris sink term to allow for a steady-state glacier was explored numerically. The model uses the boundary conditions for Khumbu Glacier including an ELA at 5700 m. The mass balance gradient, $\frac{d\dot{b}_z}{dz}$, is set to 0.01 a^{-1}. Debris accumulates at the glacier surface using the melt rate parameterization from Eq. 11. In Fig. 3.6, the resulting debris thickness profile is plotted for three cases. The first case assumes no debris sink, neither at the terminus nor along the glacier profile. In this case, very thick debris piles up at the glacier terminus; the glacier never reaches steady state and continues to advance. In the second case, a basal sink of debris was applied along the glacier guided by observations presented in Fig. 3.5. In this case, thickened debris still forms at the glacier terminus, as the basal sink is low in this location. The modeled glacier never reaches steady state, although the advance is much slower than the case with zero sinks. The final case assumes that debris is lost both along the glacier and at the terminus. The terminal sink rate was set using measurements from Chapter 2 that calculated the volume of the terminal debris infilling. The rate of debris removal assumed the debris had accumulated over 10 ka (Richards et al., 2000). An initial debris sink was set at 0.15 m a^{-1} and was modified until the glacier converged to steady state, which occurred at 0.26 m a^{-1}.

3.5.4 LIA and LGM glacier conditions

Next, we simulate the LIA and LGM stages of Khumbu Glacier. The coupled flow model was run to steady state under constant climate conditions until the glacier profile matched the LIA extent and closely approximated the surface profile set by the LIA moraines (Fig. 3.7a). The model uses the same mass balance gradient as other models but uses an ELA position that was initially set at 5480 m (Kayastha and Harrison, 2008), roughly 220 m lower

than the modern ELA. Ultimately, an ELA set to 5540 m yielded the most realistic values for the extent and thickness of the glacier during the LIA. For reference, the sensitivity of ELA rises and falls is explored in section 4.6. As with all models, the debris sink acts along the entire glacier and at the terminus. At the surface, debris accumulates based on the local-melt rule (Eq. 10) and begins with zero surface debris. The growth of melt-out surface debris begins at a location just north of EBC, corresponding to the location where modern debris starts. This location is fixed in all models, except the LGM solution, because surface debris is not expected to form in the ice-fall due to it being steep and heavily crevassed, even though parts of it are below the ELA. To facilitate comparison with other recent numerical studies, our reference model uses values for the key parameters that are nearly identical to those used by Anderson and Anderson (2016), including the flow law parameter, Glen's constant, shape factor, time-step, grid spacing and surface mass balance gradient.

At the most stable position for the glacier terminus, the LIA glacier has ~29% more volume than the modern state, indicating that there has been a substantial volume loss since the late 1800s. The model results also highlight the post-LIA decrease in ice flux (Fig. 3.7b); at Gate 1, the LIA ice flux was about 27% higher, whereas at Gate 7, it was 95% higher. We attribute this downglacier decrease in the ice flux since the LIA to the extremely low slope and surface velocities.

While modeling the LIA glacier provides confidence in the flow model we seek additional support by exercising the model to simulate the glacier extent from the LGM (~18 ka) and examine the state of a much larger glacier. As before, we use the observed moraines, which indicate glacier thickness and extent. In contrast with previous simulations, the LGM glacier is modeled assuming that the valley debris infill was eroded and evacuated during the

glacial advance (Fig. 3.8). The glaciers corresponding to the oldest well dated moraines, which are 30 ka and older would have filled the entire lower portion of Khumbu Valley, rather than only the central portion that is currently occupied by the modern, underfit Khumbu Glacier. We expect that the broader valley had to be excavated during this and similar glacial advances, and hence that any unconsolidated debris would have been removed during the extended ice advance over this area.

Similar to the LIA model, we assume that the surface debris is best modeled as a coherent layer using the local-melt rule because we do not expect thick surface debris and extensive thermokarst to develop during the culmination of the LGM due to the increased ice flux and the reduced transit time through the ablation zone. We set the initial LGM ELA at 5400 m, which is in accordance with published values (Owen and Benn, 2005; Gayer et al., 2006; Asahi, 2010) and adjust it to explore the sensitivity. We also adjusted the mass balance gradient until the glacier reached a steady-state profile that closely matched the LGM moraines; with the ELA at 5450 m, the optimal mass balance gradient was 0.09 a^{-1}.

The most realistic simulation of the LGM glacier, according to the moraines, is shown in Fig. 3.8. At the location of the modern-day terminus, ice during the LGM is ~375 m thick, about 10 times the modern ice thickness at the terminus. Along the glacier profile, the LGM surface is at a similar elevation to the LIA moraines, but the ice is much thicker, especially near the current terminus, due to the removal of subglacial debris. The thickness profile of supra-glacial debris during the LGM is similar to that during the LIA, reaching just over a meter of debris near the terminus.

3.5.5 Perturbing the LIA state to achieve modern and potential future states

The LIA surface is used as the initial, steady-state condition and the ELA is progressively raised from 5540 to 5700 m to approach the modern state of the glacier. During the simulation, the ELA is raised 1.1 m a^{-1} for the first 150 years and then kept constant at 5700 m. We run the simulation for 500 years starting at the end of the LIA to explore the long-term model behavior and show time slices at 0, 75, 150, 250, and 500 years; the 150 year results are those corresponding most closely to modern conditions. We examine the impact of the treatment of the debris influence on the mass balance on the glacier evolution by comparing glacier profiles using the two distinct melt rules. The differences in elevation between modeled glacier profiles and the LIA reference model, and in the corresponding debris thickness profiles are shown in Fig. 3.9 and 3.10.

Evolution of glacier during an ELA rise using the local-melt rule

The first case uses the local-melt relationship (Eq. 3.9). The glacier shrinks due to the ELA rise. The initial debris mantle developed in the LIA simulation efficiently slows melting, and therefore, changes in glacier and debris thickness, are entirely controlled by the divergence in the ice flux where the surface debris thickness exceeds ~50 cm. Fig. 3.10a shows that the debris thickness changes near the terminus are not substantial.

Fig. 3.9 shows that the post-LIA surface subsidence increases downglacier rapidly where debris begins to form, and then declines progressively. The maximum difference between the LIA surface and this model is roughly near EBC, which conflicts with field observations. In the upper third of the ablation area, the 150-year profile approximates the current day surface closely, but the thinning rate averages over the entire ablation zone only 0.19 m a^{-1} over the modeled 150-year timespan (Table 1). Even over the shorter 75-year

timespan, the average surface thinning rate is only 0.18 m w.e. a^{-1}, just under half of the 0.38 ± 0.07 m a^{-1} thinning rate measured over the time period 1970—2007 (Bolch et al., 2011). Furthermore, the LIA moraine suggests that, on average over the ablation zone, the glacier surface has subsided 45 m at a rate of 0.3 m a^{-1} in the last 150 years.

Evolution of glacier during an ELA rise using the large-scale melt rule

In this model case, the glacier evolves from the LIA state using the large-scale melt rule (Eq. 12). Surface debris thickens over time as rapid ice melt supplies debris to the glacier surface; it approaches about 3 m by 150 yr, which compares favorably with debris thickness measurements that show several meters of debris in the lower part of the glacier (Fig. 3.10b). As with the local melt rule, the post-LIA surface subsidence increases downglacier rapidly in the upper reach of the ablation area but continues to increase far past the point where the subsidence derived using the local rule switches trend (Fig 3.9), which is considerably more consistent with field observations shown in Fig 3.9. This subsidence gradually decreases downglacier from the highpoint and becomes nearly constant in the lowest 5 km of the glacier.

The average rate of thinning closely resembles modern-day rates for the entire ablation area; however, near the glacier terminus, the rate for both the 75 and 150 year time-steps was about 0.2 m a^{-1}. The glacier continues to subside even after the ELA becomes stable at timepoint 150. For a glacier averaging 150-300 m and with terminus ablation at 5-10 m a^{-1}, the response time is 15-60 years. At Khumbu, glacier thinning is about 0.1 m a^{-1} at the terminus and averages 0.5 m a^{-1} over the entire ablation zone. The average thickness is about 150 to 200 m, which yields a response time of 300 to 2000 years. Although the final model output is 500 years, the model reached steady state at about 425 to 450 years (i.e., 275

to 300 years after the ELA stopped rising), which is reasonable considering the response time of the glacier.

3.5.6 Model Sensitivity

In addition to the model results shown above, we ran additional simulations to explore the sensitivity of model parameters (i.e., ELA change, mass balance gradient, englacial debris concentration). Glacier length is more sensitive to the mass balance gradient than for changes in englacial debris concentrations as the melt out of debris is dependent on the melt rate. In Fig. 3.11, the temporal sensitivity of the overall glacier length using the large-scale and local melt rules is shown for various stepwise perturbations in ELA. An asymmetry exists between rises and drops in ELA for both cases; however, it is more pronounced for the local melt rule. The asymmetry indicates that rises in ELA have less of an influence on glacier length and highlights the role that surface debris has on glacier evolution.

3.6 Discussion

This study leverages considerable field data to quantify multiple facets of Khumbu Glacier that bear directly on the "debris-covered glacier anomaly" (i.e., equivalent thinning for both debris-covered and clean glaciers) including: 1) the development of a new melt-rate parameterization based on modern-glacier observations 2) the treatment of debris sinks on the glacier and 3) modern glacier dynamics at the glacier terminus. To my knowledge, this study is the first to implement a spatially varying debris sink along the glacier that complements the loss of debris at the glacier terminus. Without the debris sinks, a thick layer of debris forms at the glacier terminus resulting in continuous glacier advance as the melt

rate vanishes. Moreover, the terminal sink is not dependent on the local melt rate, which better reflects conditions at Khumbu Glacier where the entire glacier toe is completely covered with debris.

Repeat GPS surveys of sites on the lower glacier have shed light on changes in regions of very thick debris. Except for one site, all showed slow surface subsidence (vertical velocity of about -0.05 m a^{-1}) despite the positive emergence velocity expected to approach ~0.5 m a^{-1} due to the convergence of ice. This unambiguous result indicates subsidence of the debris layer at about 0.55 m a^{-1}, which is not likely caused by ice melt below the surface boulders at the debris-ice interface due to the very thick nature of the debris. Using the average temperature profile in 2.5 m of debris, Conway and Rasmussen (1980) estimated the average flux of energy through the debris was sufficient to melt 2 mm day^{-1} of ice, or roughly 0.01 m a^{-1} over a 100 day melt season. We suggest that the solution to this conundrum may lie in an extensive network of englacial or subglacial conduits, which have been documented at Khumbu Glacier (Benn et al., 2009). Closure or collapse of conduits sufficiently below the glacier surface would lead to generally coherent subsidence, as our measurements suggest, rather than local collapses in the immediate vicinity of the GPS sites. Moreover, emergence velocities would have been overestimated if the conduits effectively render the glacier compressible, rendering the ice continuity equation inappropriate as used here; incompressibility is assumed implicitly in using Eq. 1.

In model simulations, time-slice 150 represents the modern-day glacier and is therefore most suitable for assessing the transient model (Fig. 3.12). We stress that a number of characteristics of the modern glacier figure in this assessment of model results, including thick surface debris (~3-6 m) near the terminus, variable surface thinning rate that is

dampened by surface debris, gentle to near-horizontal glacier surface near the terminus, and little or no retreat since the LIA. For the local-melt rule, the modeled glacier thins on average ~24 m, and at most ~50 m since the LIA, and the thinning rate averages 0.16 m a^{-1} over the entire ablation zone and 0.1 m a^{-1} near the terminus. Slow thinning implicit in the local-melt rule would add only a few centimeters of debris near the terminus. Fig. 3.7 shows the surface debris thickness increases very slightly from its starting state at the LIA and reaches only ~1 m near the terminus, considerably less than the 4 m debris cover, and up to 12 m in some places (Chapter 2).

In the large-scale melt rule model, at time 150, the glacier thins on average, 65 m, with a maximum of ~90 m (Fig. 3.6). The average thinning rate is 0.43 m a^{-1}, consistent with remotely derived contemporary rates averaged over the entire Khumbu ablation zone: 0.37 m w.e. a^{-1} (Bolch et al. 2011) . Near the terminus, modeled thinning is slower, ranging 0.1 to 0.16 m a^{-1}. These rates are similar to thinning rates measured from repeat GPS surveys, which averaged 0.08 ± .07 m a^{-1} in the same region (Fig. 3.4). Debris, albeit thicker than the local-melt rule, reaches ~4 m thick near the terminus suggesting that even with the elevated ice-melt rate, there are still elements that warrant future work. Including a debris sink resulted in less debris cover and a larger glacier retreat and increasing the concentration of debris led to small changes in surface debris thickness but the overall effect was small due to the feedback between ice melt and debris thickness.

Our results show that the large-scale melt rule is more realistic then the commonly used local rule for Khumbu Glacier, and by inference for other glaciers with a thick mantle of debris and distinctive thermokarst surface. For the entire glacier, from the LIA to the present (at time-step 150 years) the volume loss modeled using the large-scale rule is 20% the LIA

volume. This calculated volume loss is comparable to the actual loss, 17%, estimated using the surface drop from the LIA moraines to the modern surface and neglecting the very slight glacial retreat since the LIA. In contrast, Rowan et al. (2015) predicted a volume change of 38% and unrealistically large ice retreat from the LIA to the present; note that they assume a 500 yr timeframe for the change from the LIA to present. Assuming no further climate change, they predict a further loss of 8-10% of the present-day glacier volume by AD2100. Our study predicts similar results, about 6% volume change by AD2100, largely in the upper and middle part of the glacier, and small change in the terminus ice thickness and extent.

The performance of the large-scale melt rule with respect to the local melt rule indicates that a model that captures the character of the surface may be more important than the debris thickness. At Khumbu, the lowest two kilometers show both a coherent, low-relief surface and a hummocky, karst like surface. The thermokarst surface begins at the proglacial stream outlet and increases across the glacier northward. This is shown in Fig. 3.1b as the dark surface containing GPS sites 6-9; east and north of the sites the glacier surface has a lighter color and is more dissected by surface streams. Increased warming beyond what we see today will exacerbate thinning in the thermokarst parts of the glacier, while the thick, coherent layer of debris near the terminus will stagnate and thin much more slowly. While we do not predict complete detachment of the lower glacier, it suggests the likelihood of formation of a major supraglacial lake, consistent with early work (Naito et al., 2000) as the central part of the ablation area is thinning about four times faster than the lowest section.

Although the studies in the preceding paragraph, and that by Shea et al. (2015), which predicts a total volume loss of 73 to 96% due to sustained warming by the year 2100, yield contrasting results they all point to a future in which Khumbu Glacier will have lost a

substantial part of its volume by AD2100. Using results of our most realistic simulation, the volume of water stored in the glacier as ice starting in the LIA decreases by 0.25, 0.45 , 0.70 and 1 km^3, respectively, in 50, 150, 250 and 350 years, which is roughly 200 years into the future. The contribution of ice melt to the proglacial stream discharge is also important for local populations. From Chapter 2, water discharge measured, averaged over two years, for the proglacial stream was ~3.8×10^7 m^3 yr^{-1}. Using the ice-melt rate from Fig. 3.2 for debris-covered ice and Eq. 9 for clean ice, the expected contribution of ice melt to the proglacial discharge is about 1.5×10^7 m^3 yr^{-1} or about 40% of the proglacial discharge. Not only does this define a future of diminishing glacier volume, but it also means a serious reduction of freshwater storage that is supremely important locally for regions with prolonged dry periods, and important on much large scales for the large river systems emanating from high alpine areas and for sea-level change.

3.7 Conclusions

We have used published estimates of ELA, present and past, as input for a coupled ice flow and debris evolution model to explore the response of debris-covered glaciers to climate change. We leverage a wealth of existing information combined with novel datasets gathered in this study to validate a model of Khumbu Glacier. Our study is the first to define quantitatively the influence of a thick debris cover, exceeding a few decimeters in thickness, on the melt rate. Relative to influence of thin debris layer, melting is enhanced primarily due to thermokarst processes that underlie the "debris-covered glacier anomaly" (Kääb et al., 2012). Horizontal GPS measurements on surface boulders indicate that the glacier is actively flowing, even in the lowest reaches of the glacier. Vertical velocities show that the debris cover is subsiding, even though a positive emergence velocity is expected due to ice

convergence throughout the lower section of the glacier. This expectation, however, stems from the assumption that the glacier is incompressible, which may be false for the ablation area due to a network of englacial conduits created by the thermokarst activity.

Results of a glacial flow model illuminate the overall influence of surface debris and sinks of debris on the evolution of both the glacier and the surface debris thickness and character (i.e., continuous or interspersed with thermokarst features). When the climate is unfavorable for the glacier growth and ice motion is relatively slow, the debris influenced on melting is best modeled using a large-scale melt rule that represents relatively rapid ice loss where the glacier surface is karst-like and lakes and ice cliffs contribute significantly to ice losses. Under more favorable condition, during steady periods or advances, such as during the LGM, the best fit between simulation and records of past extent and ELA required the use of a local-melt rule; using a large-scale melt rule required the ELA to be 75 to 100 m lower.

Since the LIA, the glacier has thinned at rates averaging 0.4 m w.e. a^{-1} indicating that there is no apparent acceleration in glacier shrinkage. Thinning near the terminus is considerably slower, ~0.1 to 0.15 m w.e. a^{-1}, and matches GPS measured rates of surface lowering for the same region. In this area, the contribution of debris from melt-out is small, which highlights the significant contribution from dynamic thickening. Our model results agree with studies (Shea et al., 2015; Rowan et al., 2015), although our magnitudes differ, suggesting that Khumbu Glacier will continue to thin for several decades to come, even if the current climate persists.

3.8 Supplement

More Sensitivity: Comparing a clean ice model to debris model

In this section, we model the response of a glacier with and without debris to explore glacier sensitivity to debris cover. We start with a glacier similar to the LIA Khumbu and raise the ELA by 1 m a^{-1} for 200 years. The glacier surface profiles at time increments of 50 years are shown in Fig. 3.13. The debris-covered case uses the large-scale melt rule. The retreat is slower in the debris case and it flattens the glacier surface, producing a glacier profile similar to that of the current Khumbu glacier. The clean glacier maintains the convex-up profile typical of the ablation zone of steady-state glaciers.

Figures for Chapter 3

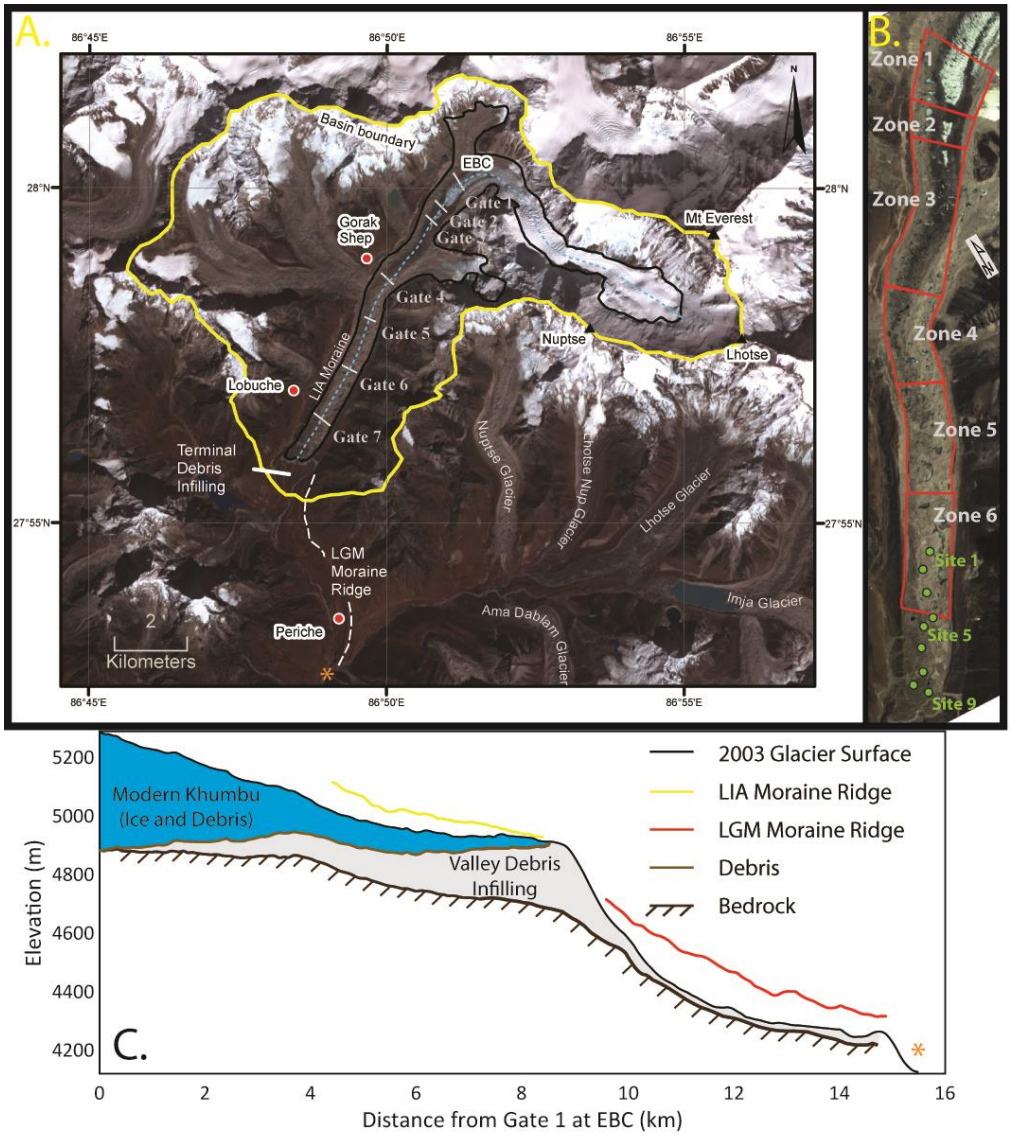

Fig. 3.4. – A. Multiband composite satellite image of Khumbu Basin (ASTER—3 Oct 2003). Settlements (red dots), Everest Base Camp (EBC), nearby glaciers, and major peaks are identified. Transverse white lines, labeled as gates, locate ice-thickness radar surveys by Gades et al (2000). The blue dotted line outlines the glacier centerline. Periche, about 5 km downvalley of the current terminus, is nested within the moraines marking the extent of Khumbu Glacier during the LGM (white dashed line outline the left lateral moraine). B. Inset on right shows glacier zones discussed in text; bounded by LIA lateral moraines and ice-thickness gates. Green dots identify GPS sites repeatedly surveyed to calculate surface velocities in a region of slow motion. C. Schematic downvalley cross-section of Khumbu Glacier from EBC, at far left of schematic, to the proglacial valley; the end of the profile is shown as the orange star in A. A thick valley debris infill, reaching over 100 m at the terminus, is inferred under the modern glacier. The moraine crests (taken from 2013 DEM) of the LIA and LGM moraines are shown as the yellow and red lines, respectively (Finkel et al., 2003; Barnard et al., 2006).

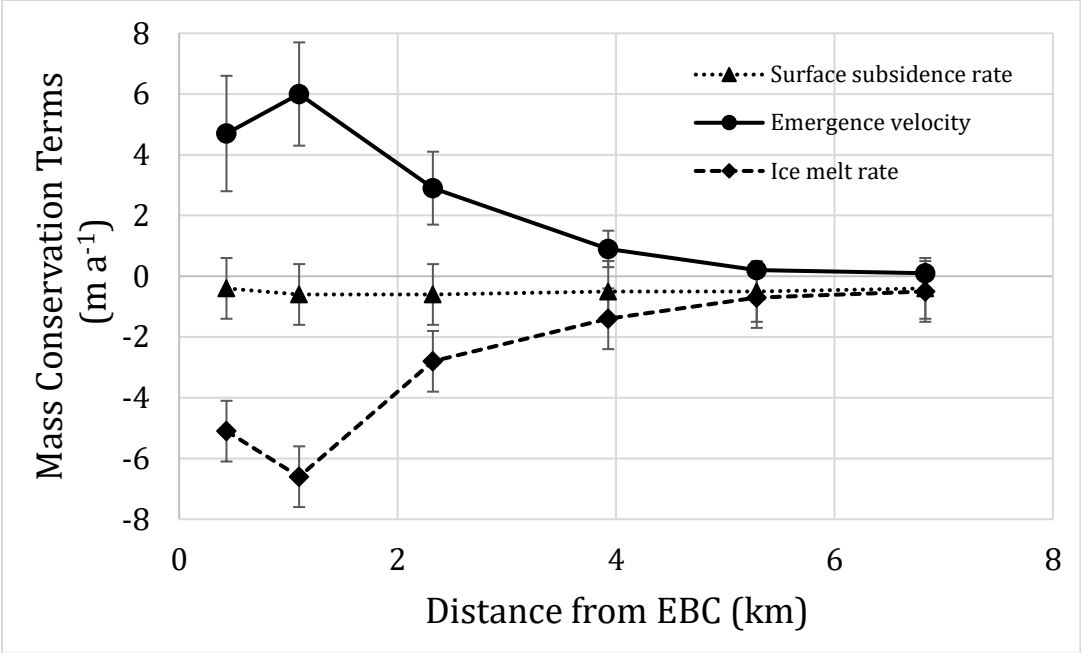

Fig. 3.2 – Components of the conservation of mass equation (Eq. 1) averaged within each glacier zones (see Fig. 3.1). For reference, zone 1 extends downglacier from the highest radar survey, Gate 1 near EBC.

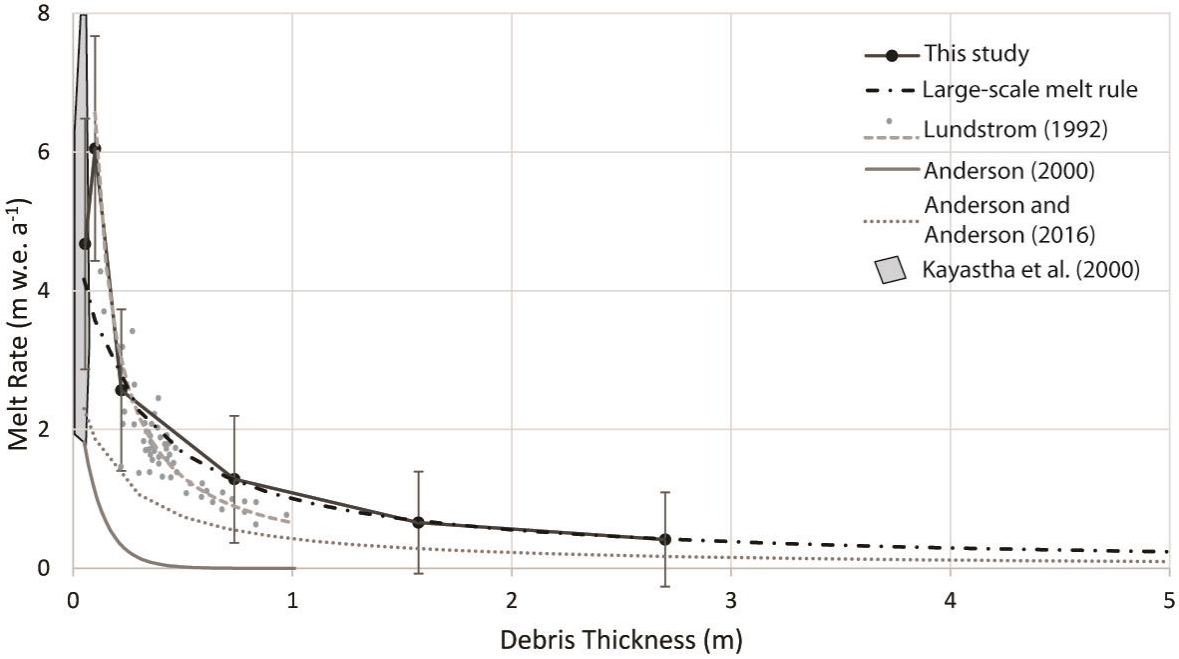

Fig. 3.3 – Relationships between melt rate and debris thickness for Khumbu Glacier. The grey dashed line is fitted to a global set of measurements (grey circles) compiled by Lundstrom (1992) of ice melt beneath debris layers; note that no data exist for debris over 1 m thick. The solid black line shows melt rates derived in this study using the sum of the emergence velocity and surface subsidence rate (error bars show uncertainties in the measurements) and the corresponding new large-scale melt rule developed for Khumbu Glacier (Eq. 12). The black polygon shows the range in ice-melt values for bare ice and ice covered with up to 5 cm of debris at EBC from May 22nd to June 1st 1999 (Kayastha et al., 2000); these values are annualized assuming that they are representative of the 5 warmest months (May – Sept.) and that melting is insignificant during colder months. The solid and dotted gray lines represent melt-rate parameterizations used in Anderson (2000) and Anderson and Anderson (2016), respectively. The dash-dot black line represents the new large-scale melt rule developed for Khumbu Glacier.

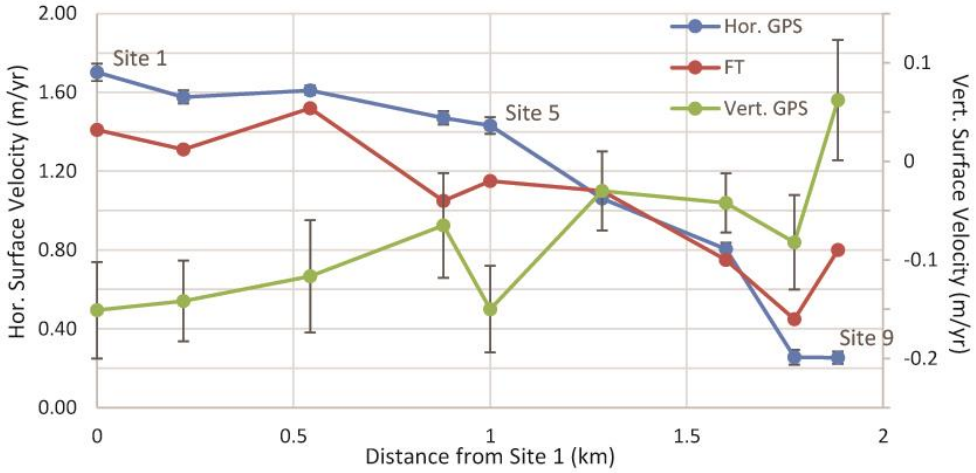

Fig. 3.4 – Horizontal and vertical surface speeds derived from GPS measurements and feature tracking (FT) for the lower reach of Khumbu Glacier. FT are from scenes spanning January to May 2008 and March to May 2008. GPS surveys were in May 2012 and April 2015.

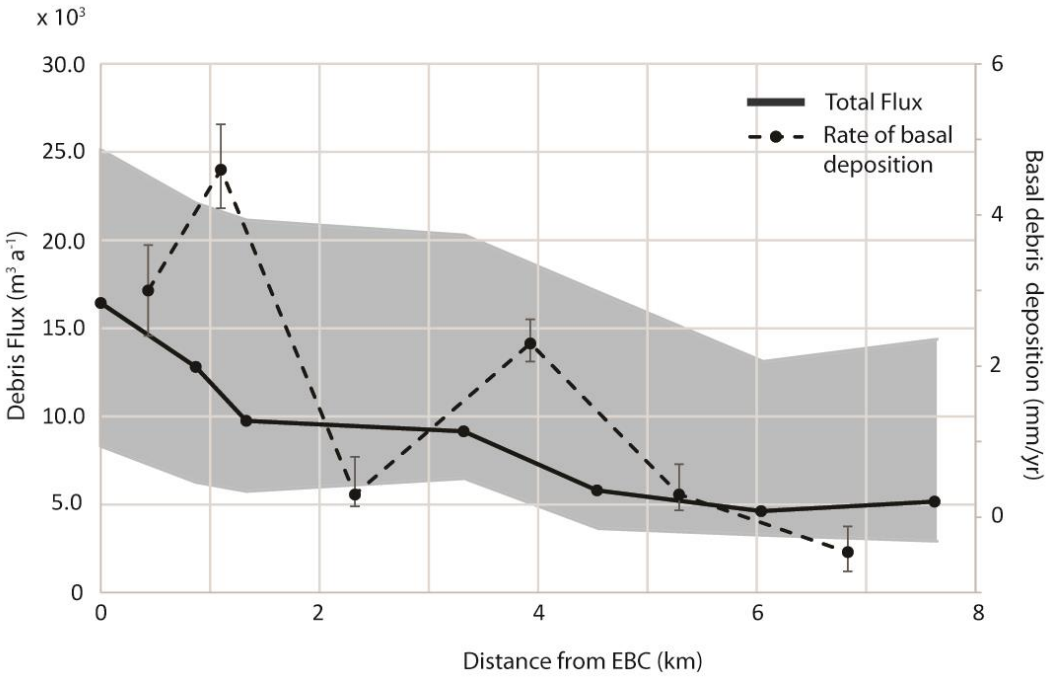

Fig. 3.5 – Total debris flux (solid line; range in flux estimates shown as shaded gray area) downglacier from near EBC (site of highest ice-penetrating radar profile; see Fig. 3.1) to ~ 2 km upglacier from the terminus where the lowest radar profile was surveyed. Rate of basal debris deposition and uncertainties averaged over each of the glacier sections shown in Fig. 3.1 (dashed line; vertical axis on right) plotted between each ice-thickness survey site.

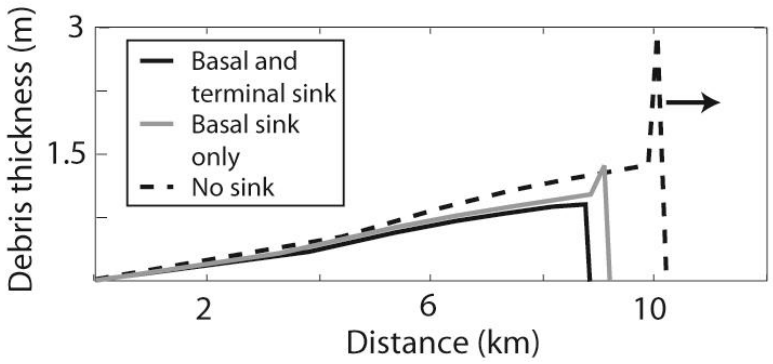

Figure 3.6 – Debris thickness profile for three cases that investigate debris sink terms. The dotted line has zero debris sinks causing a thick pile of debris at the terminus and the arrow indicates that the glacier continues to advance. The gray line uses a debris sink along the entire length of the glacier, which still resulted in a thickened terminal debris layer. The solid black lines uses both the basal sink and the terminal sink and reached steady state.

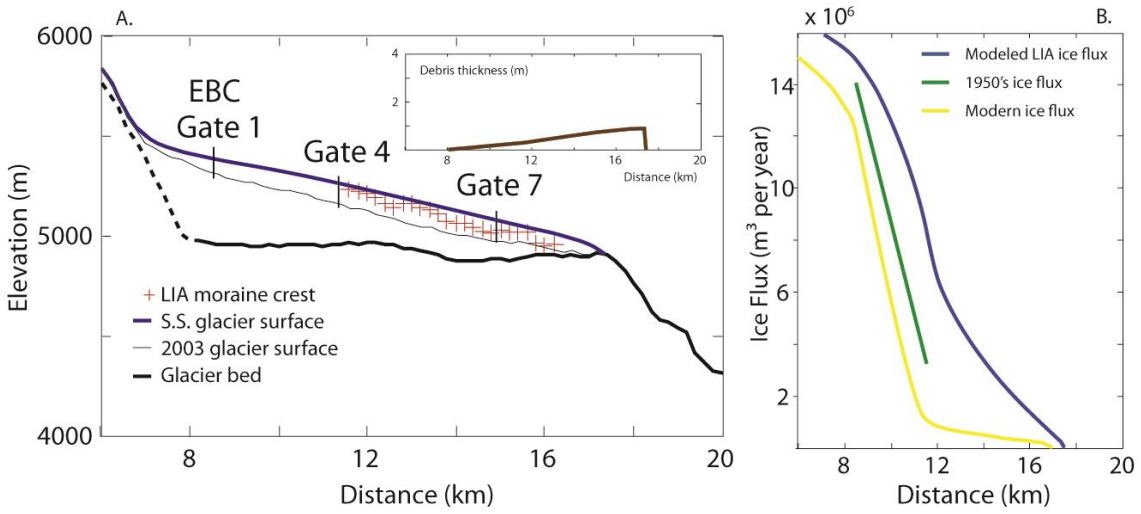

Fig. 3.7 – A) Modeled steady-state surface profile of Khumbu Glacier that matches glacier extent and approaches the profile of the LIA moraine crests. We exclude upglacier results to ease interpretation. Thin and thick black lines show the 2003 glacier surface, and bed interpolated from ice thickness data (Gades et al., 2000); where line is dashed, ice-thickness was calculated assuming a constant basal shear stress. Gates identify locations of glacier characteristics for the LIA and modern glacier shown in Table 3.3. Modeled debris thickness at steady state is shown as the inset panel. B) Modern and 1950's ice fluxes were guided by measurements of surface velocity (Müller, 1968) and ice thickness.

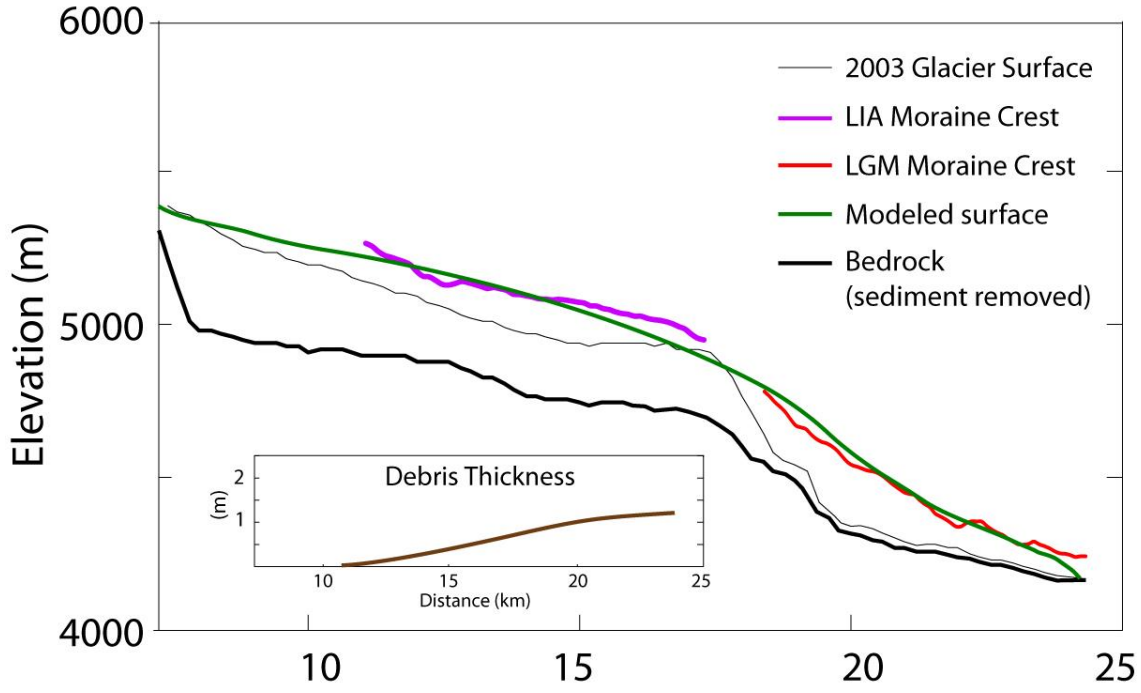

Fig. 3.8 – LGM extent of Khumbu Glacier. During this state, we assume the debris cover is thin but continuous at all scales, and hence use the local-melt rule. For this case, the valley fill is removed and the glacier now moves over bedrock. Debris thickness is shown in the inner panel and is barely over 1 m thick near the terminus. The surface of the LGM glacier is at about the same level as the LIA moraines but is thicker due to the lack of subglacial debris. Note that the upper reaches of the model are not included in the presentation.

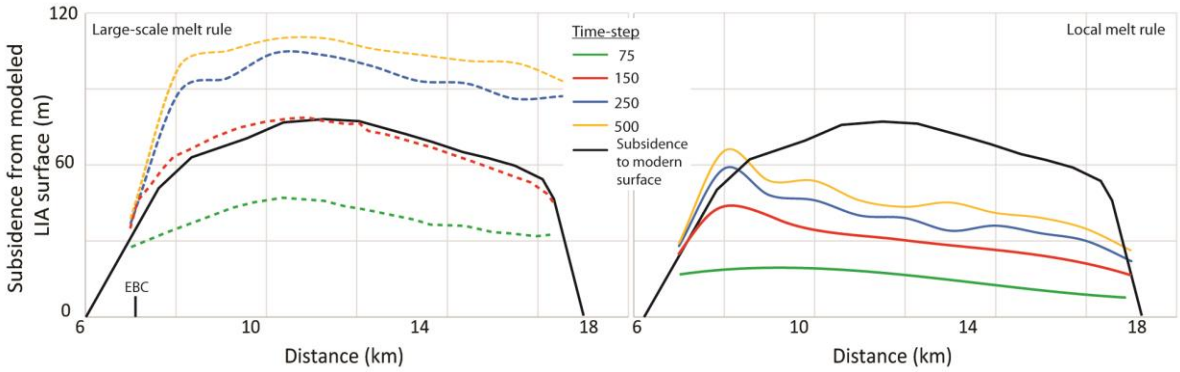

Fig. 3.9 – Surface subsidence for both the large-scale melt rule (at left) and local melt rule (at right) relative to the modeled LIA surface. The red line corresponds to the modern time in the model. For comparison the distance between the modern glacier surface and the modeled LIA surface is shown as the thick black line.

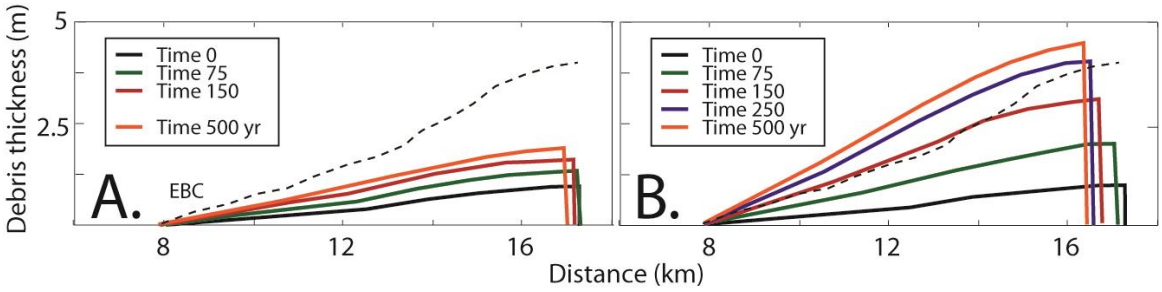

Fig. 3.10 – Debris thickness evolution for the A) local melt rule and B) large-scale melt rule. Time 250 is not shown in A to improve visualization. Dotted line shows debris thickness profile for Khumbu (Chapter 2).

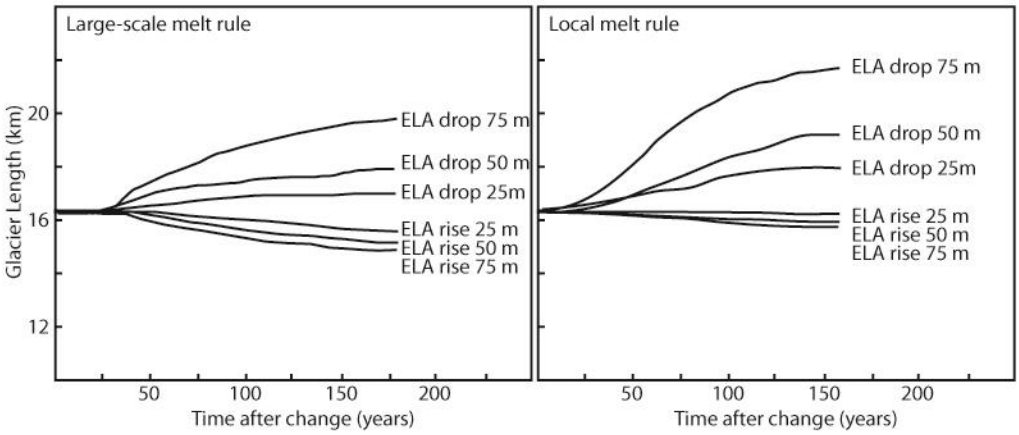

Figure 3.11 – Spatial and temporal response of glacier after a rise/fall in ELA. Glacier model uses the local-melt rule (Eq. 10).

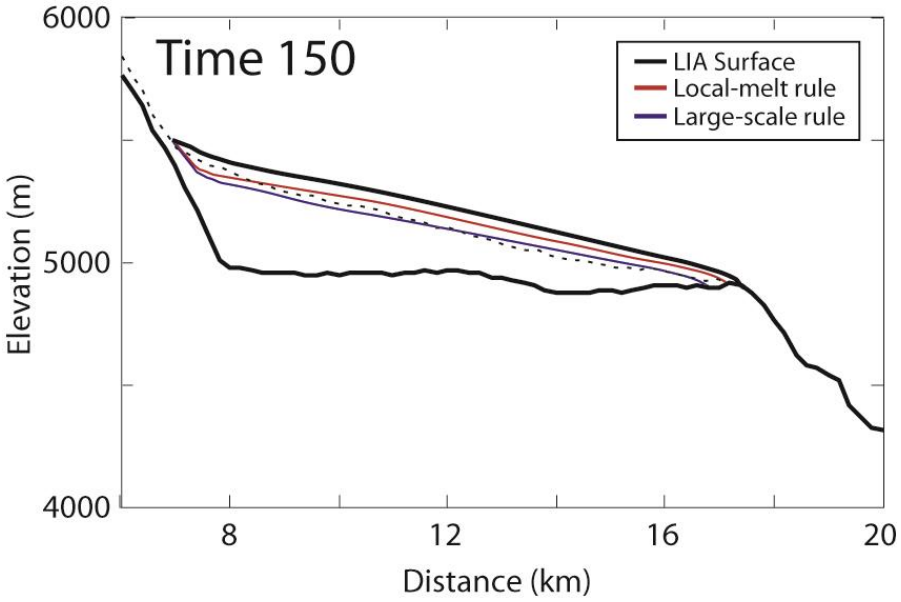

Fig. 3.12 – Model runs at time-point 150 years, which should approach the modern Khumbu (dashed line).

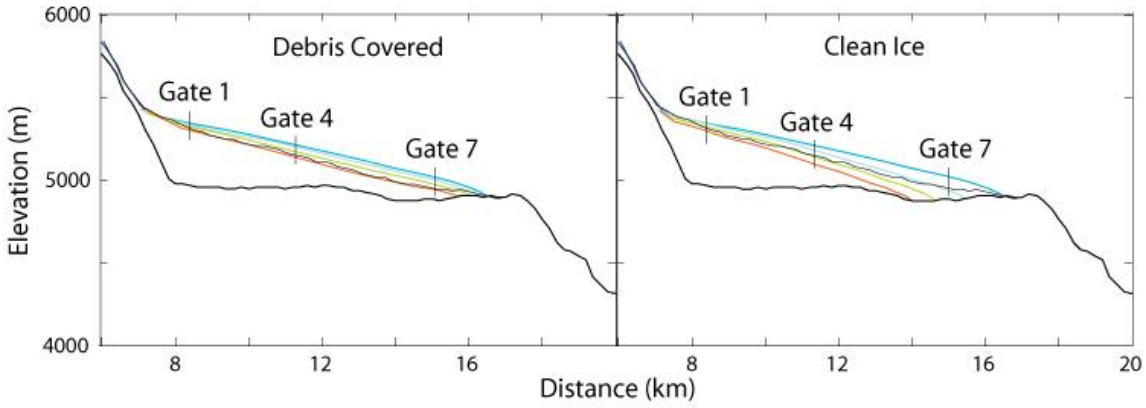

Fig. 3.13 – Glacier evolution for both debris and no debris cases. The left panel is the debris-covered case and evolves using the large-scale melt rule. The right panel is the clean glacier case and evolves without debris cover. Colors ranging from blue to green to orange correspond to initial, intermediate and final stages.

Tables for Chapter 3

Table 3.1 – Summary of differences in surface elevation

Table 3.1. Summary of differences in surface elevation averaged over the ablation zone between LIA profile and modeled profile*.

	75		150		250	
	Surface subsidence	Thinning rate	Surface subsidence	Thinning rate	Surface subsidence	Thinning rate
	m	m w.e. a^{-1}	m	m w.e. a^{-1}	m	m w.e. a^{-1}
Local-melt rule	15	0.18	28	0.15	39	0.14
Large-scale rule	37	0.45	66	0.40	97	0.36

* For comparison, the LIA moraine suggests that, on average over the ablation zone, the glacier surface subsided 45 m at a rate of 0.3 m a^{-1} in the last 150 years.

Table 3.2 – Summary of modern glacier variables

Table 3.2. Summary of modern glacier variables and zone-averaged dynamic thickening.

Gate	$\bar{u}$	H	w	Q	Δx	Emergence Velocity	Zone
	m a^{-1}	m	m	m^3 a^{-1}	m	m a^{-1}	
1	34	390	900	1.2×10^7			
2	30	340	800	8.2×10^6	880	4.7 ± 1.9	Zone 1
3	25	320	750	5.9×10^6	450	6.0 ± 1.7	Zone 2
4	14	135	690	1.8×10^6	2100	2.9 ± 1.2	Zone 3
5	5	110	630	3.2×10^5	1350	0.9 ± 0.6	Zone 4
6	3	85	600	1.0×10^5	1550	0.2 ± 0.09	Zone 5
7	1	40	600	2.4×10^4	1585	0.1 ± 0.05	Zone 6

Table 3.3 – Model LIA glacier

Table 3.3. Model LIA glacier and modern characteristics

	Ice thickness difference (m)	LIA Model ice flux (x 10^6 m^3 a^{-1})	Modern measured ice flux (x 10^6 m^3 a^{-1})	1950's measured ice flux (x 10^6 m^3 a^{-1})	LIA Model debris thickness (m)	Measured debris thickness (m)
Gate 1	65	19.0	12.0	14.0	0.01	0.03
Gate 4	95	4.8	1.8	3.3	0.35	0.5
Gate 7	105	0.87	0.04	-	0.8	3.4

Chapter 4: Orogen-wide rates of glacial erosion during major (~100-kyr) glacial cycles in the St. Elias Mountains, SE Alaska

4.1 Abstract

Localized convergence between tectonic plates and rapid erosion have created the highest coastal range in the world - the St. Elias Mountains, SE Alaska. The spatial and temporal distribution of glacial erosion rates, the dominant form of erosion in the region, however, remains poorly defined and understood. Herein, we numerically simulate the distribution of glacial erosion rates throughout the St. Elias Mountains for two time scales, contemporary, based on the current dynamics and configuration of the principal existing glaciers in the study region, and long-term, the last 10^5 to 10^6 years during which the regional ice masses have undergone major cyclic fluctuations. For the long term, we calculate erosion rate as a function of time and space for one representative cycle using an ice sheet model that is validated through comparisons of model results for the current climate with the characteristics of existing glaciers in the region. We hypothesize that the rate of erosion scales with the glacier power, the amount of energy available for erosion per unit time and per unit area of the glacier bed. Long-term model results show that, in general, erosion rates averaged for the principal glaciers in the range are relatively constant in time, and that the location of rapidly eroding domains is relatively stable due to topographic controls despite the large glacier fluctuation. These domains of rapid erosion do not spatially correlate with the time-averaged position of the equilibrium line (EL). The erosion model results are compared to published exhumation rate data inferred from thermochronology to test our hypothesis and the erosion model. When averaged over an entire major (~100-kyr glacial

cycle), glacier power accounts for nearly 70% of the variation in the exhumation rate data throughout this orogen. This is quite surprising because of variations in bedrock characteristics and in uplift that are expected to be large. The strong correlation between exhumation data and glacier power validates the hypothesis that the rate of erosion scales with power and the numerical erosion model. It also enables calibration of the relationship between glacier power and erosion rate for the St. Elias region.

4.2 Introduction

The rugged mountains of SE Alaska have recently received considerable attention because of the interest in the interplay between climate, erosion, and tectonics. In particular, the St. Elias Mountains constitute an ideal natural laboratory for studying this interplay where the dominant geomorphic agent eroding the region and carving the landscape is glacial ice. Moreover, a well-preserved offshore sediment record and relatively constant tectonic convergence rates constrain mass flux estimates and shed light on temporal variations in erosion rates (e.g., Gulick et al., 2015). Prevailing winds off the northeastern Pacific, together with orographic effects, result in heavy precipitation and, at high altitudes, thick snow that sustains the largest temperate glaciers on the planet and fuels rapid erosion. Moreover, the region exhibits some of the most extreme relief resulting from ongoing oblique relative motion (~55 mm/yr) between the Pacific and North American plates coupled with focused, vigorous mass wasting and glacial erosion, which is evident in some of the largest known sediment yields anywhere (Hallet et al., 1996, Jaeger et al., 1998; Sheaf et al., 2003).

The orogen formed by collision and accretion of the Yakutat terrane into the transitional corner that links subduction at the Aleutian megathrust to strike-slip motion

along the Fairweather fault (e.g., Plafker, 1987; Bruhn et al., 2004; Pavlis et al., 2014). The complex tectonic setting has resulted in major differences in the style of deformation across the orogen (Bruhn et al. (2004). In the eastern part, dextral strike-slip faulting on the Fairweather fault along with crustal contraction drives deformation forming the narrow coastal range (Bruhn et al., 2012). At the syntaxial corner, the plate boundary bends westward; the north-dipping Chugach-St. Elias fault sutures the Yakutat terrane and southern Alaska forming foreland, and offshore (the Pamplona Zone) fold and thrust belts. GPS measurements straddling the main faults indicate the fault-perpendicular motion is distributed between shortening offshore and in the orogen with significant structural faulting/rotation, high strain concentration, and rapid uplift (Figure 4.1; Elliot et al., 2013). In the western part, structures curve southwestward toward the Aleutian Trench in a region of thick-skinned folding and faulting (Bruhn et al., 2004). The evolution of the syntaxial orogen strongly depends on this complicated tectonic setting as well as the lithospheric rheology and climate-tectonics interactions (Zeitler et al., 2001; Koons et al., 2010; 2012).

Despite the widespread recognition of the importance of glacial erosion in the evolution of high mountains, little precise information is available about the role of glaciers, and rates of glacial erosion are defined only by sparse data representing averages over single or multiple basins spanning up to 5000 km2. For example, numerous field studies of sediment accumulation in SE Alaska fjords (e.g., Koppes and Hallet, 2002; 2006; Love et al., 2016), on the continental shelf (Jaeger et al., 1998; Sheaf et al., 2003) and in the deep sea of the Gulf of Alaska (Gulick et al., 2015) have, respectively, documented spatially averaged erosion rates over multiple timescales for individual glacier systems and regional rates. Perhaps the highest well-documented rates derive from Tyndall Glacier in Icy Bay, a

tidewater glacier, west of Malaspina Glacier. Koppes and Hallet (2006) estimated the long-term, basin-wide erosion rate to be 9 ± 2 mm/yr based on the sediment yield from Tyndall Glacier averaged over ~50 years after applying a large correction factor (~3) to reduce the rates, in an effort to account for the probable acceleration of ice flow and release of stored sediment associated with glacial retreat. On the shelf, sediment accumulation rates averaged nearly 8 mm/yr corresponding to an erosion rate of 5.1 mm/yr averaged over the last 104 years, which Sheaf et al., (2003) attributed to efficient erosion by glaciers. The authors suggest that their estimated rates are not typical of the entire 5 Myr history of mountain building and represent only the last interglacial period. Recently, Gulick et al. (2015), reporting on seismically derived offshore sediment volumes that represent nearly 3 Myr of accumulation, underscored the significance of climate driving erosion rates, and suggest that the high sediment flux leaving the mountains exceeds tectonic inputs. Collectively, the studies of sediment accumulation in fjords, on the shelf, and in the deep sea show that erosion rates in SE Alaska are among the highest in the world.

Numerous other studies have addressed the spatio-temporal evolution of rock exhumation using multiple thermochronometers from bedrock and detrital samples; they yielded valuable data that were discussed in the context of the climate and glaciers in the region (e.g., Berger et al., 2008; Berger and Spotila, 2008; Enkelmann et al., 2008, 2009, 2010, 2015, 2017; Spotila and Berger, 2010; Pavlis et al., 2012; Grabowski et al., 2013; Falkowski et al., 2014). We note that in the St. Elias region, tectonics are dominated by convergence and, therefore, we do not expect tectonic exhumation; hence, for simplicity, we equate exhumation and erosion to conservatively assess long-term erosion rates. Much of the exhumation research was part of the Saint Elias Erosion/tectonics Project (STEEP), which

addresses the St. Elias orogen and the interaction of regional plate tectonic processes, structural development, and rapid erosion. In a review of tectonics and climate research, Whipple (2009) noted that Berger et al. (2008) and other STEEP studies represent "the most convincing case so far" for a climate influence on tectonics by documenting a shared temporal evolution of deformation and climate. Moreover, Berger and Spotila (2008) drew attention to the spatial coincidence of rapid exhumation localized along the south, windward side of the range and the general position of the mean Quaternary equilibrium line (EL) to suggest a simple explanation for the location of the rapid exhumation: glacier erosion rates peak near the EL where ice fluxes are highest, as expected on theoretical grounds (e.g. Anderson et al. 2006). However, the extent, dynamics, and spatial distribution of erosion is poorly constrained for glaciers and ice sheets such as the Cordilleran that were typical during the Quaternary. This topic merits elaboration, and will revisited in the discussion.

At the scale of a single valley, Headley et al., (2012) examined the dynamics of the ice and, in particular, the spatial distribution in basal conditions that control erosion rates within the Seward Throat, where the ice flow is exceptionally rapid and crosses major structures between Seward and Malaspina Glaciers (Figure 4.1). Merrand (2013) also examined the spatial distribution of erosion rates for the Seward-Malaspina system, and did so for a full 100-kyr cycle using a simple, 2-D glacier flow model. Despite these studies, the spatial distribution of glacial erosion rates and the influence of rock strength and crustal deformation on erosion rates throughout the orogen remain poorly known.

Whereas, the previous paragraph focuses on the spatial distribution of glacial erosion rates, other studies investigate the controls on erosion rates in diverse tectonic settings. Over geologic timescales, Yanites and Ehlers (2016) developed a calibrated erosion model for

sliding velocity and exhumation rate for the southern Coast Mountains of British Columbia, which were primarily uplifted during the late Neogene (Parrish, 1983). The results of the study confirmed that sliding influences the rate of glacial erosion; however, only the high elevation of the region remains ice covered throughout the model runs. Over the majority of time, ~80 to 90%, the model domain is either ice-free or covered with cold-based ice, whereas, the principal glaciers in SE Alaska are present over the entire 115-kyr model. In the Southern Alps of New Zealand, Herman et al. (2015) reported that the glacial erosion rate is proportional to the ice-sliding velocity squared based on 5 months of measurements of glacial velocities and suspended sediment load at Franz Josef Glacier near the Alpine Fault. The result agrees with theoretical predictions for glacial abrasion (Hallet, 1979), which suggests that glacial abrasion may be the dominant erosional process for fast-flowing glaciers over weak rock and is contrary to field observations suggesting that quarrying is the principal process of glacial erosion (Iverson, 2012 and references therein).

Herein, we present model results on glacial erosion rates for two timescales, the present-day and the longer-term; the latter represents of the past ~100-kyr when much larger ice masses covered the study area and underwent large oscillations, extending from current glacier margins near the present coastline to the edge of the continental shelf. We hypothesize that the rate of erosion increases with the glacier power, the amount of energy available for erosion per unit time and per unit area of the glacier bed, which has the advantage of representing the strength of the ice-bed coupling, the basal shear stress, as well as the sliding rate. For the present-day, glacier power is derived from modern-glacier characteristics and mass conservation principles, much as is commonly done in studies of bedrock incision by rivers (e.g., Finlayson et al., 2002). The model of glacier power is

validated by comparison with results from a full-stress 2-D model of glacier flow and sliding (Headley et al., 2012). For the long-term, we use results from an ice sheet model to define the spatial and temporal distribution of the erosion rate for ice masses that have undergone massive changes during the Quaternary. By averaging the modeled erosion rate over a complete ~100-kyr representative of the late Quaternary, we define a spatially continuous quantitative index of the erosion rate representative of the longer-term, and then compare the modeled index with geologic data that define exhumation rates in the region, to test our hypothesis that glacial erosion scales with power, and to assess and calibrate the erosion model..

4.3 Methods

We seek to define the orogen-wide spatial distribution of glacial erosion rates based on the hypothesis that the rate of erosion increases with the amount of energy available for erosion per unit time and per unit area of the glacier bed (i.e., the glacier power per unit area). We consider two states of the glaciers in the region, the contemporary glacier configuration and fluctuating glaciers over a complete, major glacial cycle. We then compare the glacier power distribution time-averaged over the cycle, assumed to represent the late-Quaternary distribution, with published values of exhumation rates from samples collected near major, long-lived glacier systems to test the hypothesis that the rate of glacial exhumation scales with glacier power, and calibrate the power-rate relationship. Note that glacier power would be more precisely described as the glacial basal power; however, we use the shortened version, which, in form, parallels river power.

Our approach is similar to that used commonly in studies that assume the erosion rate to increase with sliding speed (e.g., Harbor et al., 1988; Anderson et al., 2006; Herman et al.,

2015). With regard to erosion by ice sheets such as the Cordilleran, glacier power is preferable to sliding speed because basal shear stress may vary from around 105 Pa, comparable to those typical of alpine valley glaciers (Cuffey and Paterson, 2010), to as low as 103 Pa, where the lubricating effect of water or soft-sediments reduce erosion rates, as well as basal shear stresses. In such regions, erosion rates would more likely vary with glacier power. The glacier-power approach has been used in other studies investigating subglacial erosion beneath ice sheets (Pollard and Deconto, 2009; Hallet et al., 2011; Melanson et al., 2013); however, in these studies, the erosion law proportionality constant and exponent are poorly constrained. A further advantage of this approach is that it decreases reliance on mechanistic models of abrasion (Hallet, 1979) and quarrying (Hallet, 1996; Iverson, 2012) that address erosion on small scales (generally <10-100 m) but require detailed information that is largely unavailable about the geometry and strength of the bedrock under the ice; they are not suited for studies of erosion of large regions because of the low spatial resolution of the models used (4 km in long-term model), and of poorly known basal conditions, bed properties, and large changes in glacial cover and basal conditions over glacial cycles.

In the contemporary glacier model for the whole range, the product of the current glacier surface slope and balance flux serves as a convenient index of the glacier power per unit area. The balance flux is the distribution of mass flux that would exist if the glacier were in steady state; it derives from simple mass-conservation principles. The balance flux at any glacier cross-section is the product of the area of the basin upglacier of that section and the integrated net mass balance, derived from the contemporary climatology (Fricker et al., 2000). Note that the balance flux divided by the cross-section width and depth yields the

average balance ice speed; it exceeds the rate of basal ice motion, but only slightly so for many of the fast-moving glaciers in SE Alaska, such as the Seward Glacier, where the contribution of internal ice deformation to the overall velocity is small (Headley et al., 2012). Comparison of the balance flux with the current flux determined directly from ice thickness measurements (Rignot et al., 2013) and flow velocities (Burgess et al., 2013) showed that balance fluxes closely approximate (<7% difference) ice fluxes for the principal glaciers in the St. Elias Range. The balance flux for Seward/Malaspina and Hubbard Glaciers exceed the measured flux by 7% or less, whereas for Bering Glacier it is 12% lower than the current ice flux; mismatches on this order or larger are not surprising especially for glaciers known to undergo major surges (e.g., Molnia and Post, 2010) and for fast-moving glaciers in rugged terrain where airborne radar measurements of ice thickness are challenging (e.g., M. Truffer, 2016, pers. communication).

For the long-term model, the glacier power field is calculated through the last major glaciation, starting 115 kyr ago and ending now, for the entire orogen as the glacier systems grow and shrink. The evolution of the Cordilleran Ice Sheet is simulated using the University of Maine ice-sheet model, UMISM (Fastook and Prentice, 1994; Fastook et al., 2008). UMISM is a 2.5 D finite-element mass and momentum ice dynamics solver with embedded components for calculating isostasy, thermodynamics, basal sliding, simple calving, and surface mass balance. The spatial resolution of the model is 4 km. The glacier portion of the long-term model is validated based on glacial geology investigations. At the LGM, the model yields glaciers reaching the shelf edge and, for most of the study region, reaching the LGM extent consistent with geologic observations (Figure 4.2; Manley and Kaufman, 2002).

Much like the glacial geology studies of ice extent that were used to assess the validity of the ice-sheet model for LGM conditions, model results for contemporary conditions were assessed by comparing the modeled glacier thickness for the current conditions with direct measurements of the thickness of existing glacier using low-frequency radar soundings (Rignot et al., 2013). Figure 4.3 shows the ice-thickness differences, modeled - measured. The median of the absolute value of the thickness difference is 140 m with a standard deviation of 80 m. This amounts to ~20% of the ice thickness in the active reaches of the principal glaciers, and hence, constitutes reasonable agreement, providing confidence in the UMISM model as implemented herein.

In the UMISM model, climate is defined from gridded input consisting of monthly mean surface temperature and total precipitation. Surface mass-balance is calculated from a degree-day method based on gridded monthly inputs of temperature and precipitation (Birkel et al., 2012; Putnam et al., 2013; Schaefer et al., 2015). Within a UMISM simulation, surface temperature at each gridcell is scaled to calculated ice surfaces using a fixed atmospheric lapse rate of 5 °C/km, thus providing a means for accumulation areas to expand or contract with evolving surface topography. The model initializes with ice-free terrain.

To develop a 115-kyr simulation, climate boundary conditions were shifted between LGM and modern end members paralleling a time-series forcing signal of paleo-temperature. The gridded end-member temperature and precipitation fields were derived from existing climatologies. For the modern climate, we used the 2 km (scaled to 4 km) 1961-1990 monthly climatology for Alaska and western Canada from PRISM (Daly et al., 1997). PRISM (Parameter-elevation Regressions on Independent Slopes Model) is a knowledge-based system that uses point measurements of temperature, precipitation, and other

parameters to produce realistic gridded estimates of surface climate conditions, including orographic precipitation. Annual snow accumulation is found by summing precipitation amounts for all months when the temperature is ≤ 0 °C. A temperature forcing function is supplied by scaling the global sea-level signal from Shackleton et al. (2000) such that LGM values register -7 °C relative to mean Holocene scaled to 0 °C. Model output fields were generated every 500 years for the duration of the experiment. PRISM, which has undergone rigorous validation (e.g., Daly et al., 2000; Wang et al., 2006), is better suited to provide model boundary conditions than reanalysis (e.g., North American Regional Reanalysis [NARR]; Mesinger et al., 2006) mainly because of its high resolution (2-4 km PRISM versus 32 km NARR). Reanalysis, however, was used over ocean areas, as PRISM coverage exists only over land. In comparison with another study that uses the same climate forcing scenarios, our study shows synchronous advance/retreat phases (Seguinot et al., 2015).

The representation of glacier sliding in UMISM, which bears directly on erosion and sediment production, is a general relationship for beds at the melting point originally formulated by Weertman (1964), and modified to incorporate the strong effect of basal water and effective pressure on sliding rates. A 2D solution for conservation of water at the bed allows for basal water movement down the subglacial hydraulic potential gradient (Johnson, 2002). For coastal glaciers, a number of factors including water depth, terminal ice flux, calving rate, and melting at the ice face (Motyka et al., 2003) control the terminal position. UMISM does not include a physical treatment of ice shelves or calving at ice grounding-lines. In order to prevent ice margins from extending beyond the continental shelf, a calving parameterization was used in which a 115-m water equivalent mass loss is imposed at all

elements where the grounding-line water depth is less than 500 m below present mean sea level. LGM sea level was prescribed at 130 m below present mean.

4.4 Results

4.4.1 Contemporary distribution of glacier power

Figure 4.4 shows the spatial distribution of the relative erosion rates assuming they increase with glacier power based on contemporary glacier characteristics (i.e., glacier surface slope and balance flux) for the entire orogen. Power is only defined regions covered by large, modern glaciers. Two clear erosion hotspots stand out; as will be discussed later, they coincide with areas where exhumation is rapid (Enkelmann et al., 2015). One is the Seward Throat where the Malaspina/Seward glacier system cuts across the east-west trending high range that culminates with Mt St. Elias. The other is further east, about 10 km from the terminus of the Hubbard glacier close to where strike-slip motion along the Fairweather fault transitions to convergence across many E-W-trending structures.

In Figure 4.5, results from our contemporary erosion model are compared with those from a full-stress 2-D model of glacier flow, sliding and erosion through a small region of special interest because of the exceptionally rapid ice flow, the Seward Throat (see Figure 4.4; Headley et al., 2012). The longitudinal variation of erosion rates, normalized to the maximum value, is shown for different representations of glacial erosion. The dominant features in our results generally resemble those of the full-stress numerical model; both studies show three peaks throughout the throat, with the highest peak located at the southern end of the Seward Throat. The relative erosion rate is low both up-valley and down-valley of

the Seward Throat due the strong control of the basin geometry (valley width) on the spatial distribution of ice speed and erosion rates.

4.4.2 Quantitative glacier power averaged over a full glacial cycle

Having considered the distribution of relative glacial erosion rates for contemporary conditions and glacier extent and gained confidence in our approach, we now investigate this distribution at 4 km resolution through a complete 100-kyr glacial cycle, using UMISM. Figure 4.6 shows the modeled glacier power, the product of the UMISM-calculated basal ice speed and basal shear stress for each time-step averaged over the full glaciation. The highest time-averaged glacier power is located in regions of high relief, primarily where basal ice speed is high as ice is channeled through narrow valleys. These regions coincide with the particularly active portions of the contemporary glacier systems and suggest that rapid erosion is sustained in the areas of Bering/Bagley, Seward/Malaspina, and Hubbard Glaciers through a 100-kyr glacial cycles, and by inference, through much of the Quaternary. Outside of the St. Elias area, rapid glacial erosion is also expected in other major mountain systems including the Alaska Range, Wrangell Mountains, Chugach Mountains, and in Glacier Bay.

The offshore glacier power results should be viewed with caution as the parameterization for basal ice motion in UMISM is guided by the characteristics of existing glaciers that do not extend offshore. Moreover, the erosion model is suitable for bedrock terrain rather than substrates of unlithified sediments, and the shielding effect of sediments on bedrock erosion is not taken into account. This distinction between bedrock and sediment substrate over the broad continental shelf is important because glaciers advancing offshore well beyond the coast line would generally not to be in contact with bedrock; instead, they would override extensive outwash plains, comprised of the glacio-fluvial sediments that have

accumulated to form the shelf. Offshore model results show that as the ice advances across the shelf, ice streams emanating from the major glacial systems on land continue southward along sea valleys and shelf-crossing troughs (Figure 4.6), which represent high sediment-flux pathways for eroded material onto the shelf and, in some cases, into deep waters via the Surveyor Fan (Reece et al., 2011; Elmore et al., 2013).

The modeled spatial distribution of glacier power per unit area averaged over a major glaciation representative of the late Quaternary can be compared to available geologic data. Figure 4.7 shows the glacial power for the sub-region illustrated in Figure 4.6, where exhumation rates have been determined using low temperature thermochronology (Enkelmann et al., 2015; 2017; and references therein). Only thermochronometric measurements from sites adjacent to the modern glaciers or within a 10 km-wide zone from the northern glacier boundary are included in Figure 4.7. At many of the sites, samples were collected a few kilometers from the glaciers; we assume they represent glacially driven erosion because 1) over long time scales, we expect subaerial processes to lower hillslope at same rate as glacial erosion, and 2) the thermochronologic data are sensitive to exhumation over domains spanning several horizontal kilometers (Ehlers and Farley, 2003; Yanites and Ehlers, 2016). No direct samples of bedrock were taken under the ice, and the detrital samples are assumed representative of the bedrock for the entire catchment area. The northern 10 km-zone incorporates regions dissected by smaller glaciers, or that may have been under vigorous glacier systems before being advected northward due to the rapid convergence (~40 mm/yr) between the SE Alaska and the Yakutat block (Elliot et al., 2013). In Figure 4.7, bedrock and detrital apatite U-Th/He and fission track (FT) samples are grouped by age; young cooling ages are scattered along the southern flank of the range facing

the Pacific Ocean. For reference, apatite FT ages between 2 and 4 Ma correspond, respectively, to exhumation rates of about 2 and 1 km/Myr (assuming a 30°C/km temperature gradient and a closure temperature of 110°C), and ages between 2 and 0.1 Ma correspond to rates of about 2 to 6 km/Myr (i.e., 2-6 mm/yr; Enkelmann et al., 2015).

Figure 4.8 shows the basin-wide average glacier power per unit area over time for the three principal glacier systems. Over much of the glaciation, glacier power in each basin is remarkably constant; the magnitude of glacier power varies within a range of 2 W/m^2 or less and shows little trend. Exceptions include an increase in glacier power for Bering Glacier at the start of the model simulation when the glacier expands beyond Bagley icefield and grows over time. For the Seward and Hubbard glacier systems, the glaciers form quickly at the beginning of the simulation. At 30 ka, the sharp increase in glacier power for Bering Glacier reflects a major expansion of the glacier; the basin area nearly doubles because the drainage divide shifts northward as the ice sheet thickens during the build-up to the LGM. Another transient increase, at ~50 ka, reflects the initial stages of another major advance. The spike in glacier power dissipates quickly after the ice caps grows and may reflect low basal shear stress due to the thicker yet more gently sloping ice cap. Starting at 10 ka, the onset of LGM deglaciation, glacier power increases significantly for all three basins due to the dominant effect of the steepening ice surface on the basal shear stress. For instance, at Hubbard Glacier the ice thinned by ~150 m near the glacier terminus from the LGM peak thickness; however, the velocity sped up about 35% during the same period. Similar changes (i.e., thinning of ice coincident with increased ice velocity) occurred within Seward Throat and at the Bagley/Bering confluence.

4.5 Discussion

4.5.1 Assessing the erosion model

Model results document the spatial distribution of erosion rates in SE Alaska, for contemporary glacier conditions and for conditions averaged over the major ~100-kyr glaciations representative of the long-term, the Quaternary. The long-term model also yields the temporal pattern of erosion rates through major glaciations. A major factor generally limiting the usefulness of, and confidence in, glacial erosion models is that they cannot be validated and calibrated because of the paucity or lack of local erosion rate data. Herein, we validate the hypothesis that erosion rates increase with glacier power and the UMISM-linked erosion model of long-term erosion rates for the entire orogen, using extensive thermochronometric data that define site-specific exhumation rates. The large range of both glacier characteristics and erosion rates also enables us to calibrate the erosion model for the study region.

Figure 4.9 compares exhumation rates derived from thermochronometry to the corresponding modeled glacier power per unit area averaged over a complete glaciation. The exhumation rates were derived from apatite U-Th/He and FT ages shown in Figure 4.7 assuming a 30 °C/km geothermal gradient (Enkelmann et al., 2015; 2017). AHe closure temperatures were calculated for each sample by inputting grain radii and computed cooling rates into the CLOSURE program (Brandon et al, 1998; Enkelmann et al., 2017). Additionally, Enkelmann et al. (2017) corrected for the long wavelength topographic influence on shallow isotherms in active mountain ranges by adjusting them to the relative local (10 km radius from each sample) mean elevation (Stüwe et al., 1994; Mancktelow and Grasemann, 1997). For the region, apatite ages, as well as detrital zircon FT ages that not

shown in Figure 4.9, reveal that exceptionally rapid exhumation (~2-5 mm/yr) is primarily localized in the lower reaches of the Hubbard and Seward-Malaspina Glacier systems (Enkelmann et al., 2015). Error bars incorporate sources of uncertainty for both the glacier model (horizontal bars) and the cooling ages (vertical bars). Model uncertainty was derived from the mismatch between model results of ice flux and modern ice-flux measurements; on average, they differed by ~15%; however, we double the uncertainty to 30% to provide a more conservative estimate. Sources of uncertainty for the cooling ages, which differ for each thermochronometer, include ranges in cooling depths and temperatures as well as uncertainty in the geothermal gradient. In Figure 4.9, cooling age uncertainty is taken from errors reported by Enkelmann et al., 2015; 2017).

In Figure 4.9, an orogen-wide trend in glacier power and exhumation rate is clear and significant (p-value < 0.001), which validates the hypothesis that erosion rate increases with glacier power, and seems to do so linearly within the limits of the data. Glacier power accounts for nearly 70% of the variation in exhumation rates. Two clusters stand out from the general trend, each defined by three points: the Bering cluster above, and a cluster distinctly below the trendline. The latter represents the northern reaches of the study region where glacier power is high, 4-5 W/m^2, despite the location in the rain shadow of the St. Elias Mountains, and exhumation is unusually slow presumably due to the bedrock being relatively resistant to erosion. In this region, crystalline and sedimentary rocks were incorporated into the plate margin prior to the Yakutat plate collision and were metamorphosed ca. 50 Ma at greenschist and amphibolite grade pressure and temperature (Plafker, 1987; Plafker et al., 1994; Bruhn et al., 2012). In addition, as suggested by Koppes et al. (2015) for glaciers in another region, the relatively low precipitation and surface input

of liquid water in the rain shadow would tend to slow erosion even if sliding rates and glacier power are elevated.

In contrast, the outliers around Bering Glacier represent faster erosion, over twice as fast as expected from the trend, which is likely due to the bedrock assemblage being relatively "weak" and easily eroded in this part of the orogen. This is not surprising because it includes thick, folded, and faulted sedimentary units that have experienced only shallow burial, insufficient to reset zircon-FT ages (Enkelmann et al., 2010), and little or no metamorphism (Figure 4.1). Bering Glacier also overlies a tectonic boundary inferred to be an active thrust or oblique-slip thrust fault, the Bering Glacier fault. Moreover, the region west of the glacier, where the samples yield young cooling ages, is seismically active (Bruhn et al., 2010; 2012).

In actively deforming orogens, material weakening due to crustal strain likely plays an important role in rapid erosion due the pervasive fracturing of rock and reduced resistance to erosion (Molnar et al., 2007; Koons et al., 2012). In the St. Elias, crustal strains are expected to increase toward the eastern part of the orogen near the transition from oblique transform motion to normal convergence at the plate boundary corner due to changing crustal velocities and the intersection of orogen scale structures (Koons et al., 2010). We would expect a corresponding eastward decrease in resistance to erosion and an increase in the ratio of exhumation rate to glacier power. Figure 4.9 does not show this trend, however; even in the western part of the orogen, the region is highly erodible as indicated by the Bering cluster, presumably due to the bedrock being inherently weak. Moreover, the rapid erosion for the Seward and Hubbard glaciers in the eastern part is commensurate with the high glacier power there. We suggest that an eastward strain-related trend is not evident because the bedrock

assemblage is inherently so heterogeneous, ranging from poorly lithified sedimentary units to metamorphic and plutonic rocks. Additionally, bedrock is pervasively weakened through the entire width of the orogen by the rapid crustal convergence, as well as the extensive shearing associated with hundreds of kilometers of advection of the Yakutat terrane to the northwest along the Fairweather fault.

4.5.2 Temporal variation in basin-wide erosion rates through a glacial cycle

Over the full glacial cycle, the model suggests that glacier power for the three basins in Figure 4.8 is relatively constant compared to the large variations in the extent, thickness, and speed of the ice masses, suggesting offsetting changes in factors affecting glacial erosion during the different glacial phases. Thicker glaciers with gentle surfaces typical of major glacial advances seem to erode at roughly the same rate as smaller, steeper glaciers during inter-glacial periods. Transients occur during times of rapid advance (i.e., the peak at 50 ka), significant retreat, or large changes in basin area such as large increase in basin area for Bering Glacier at 30 ka (Figure 4.7). For the latter, glacial ice that previously flowed away from Bering Glacier reversed flow into the glacier, which increased ice discharge south of the Bering/Bagley confluence. Over the course of the glaciation, this ice rerouting occurred only once but caused a significant increase in glacier power between 30 to 20 ka, doubling the glacier power for Bering Glacier. Subsequently, power sharply decreased at the approximate time of the post-LGM retreat for glaciers in southern Alaska (Barclay et al., 2009).

Surprisingly, glacier power for all three major glaciers is faster than the long-term average beginning at the start of the Holocene, at ~ 10ka (Figure 4.8). Yet during the early to middle Holocene, glaciers in Alaska were relatively drawn back (Barclay et al., 2009), which

was likely due to warmer and drier summer conditions than today's around the Gulf of Alaska between 9 and 6 ka (Mann et al., 1998). In fact, glacier power increases over this period and only begins to lower during the Neoglaciation period of glacier expansion after 5-6 ka. During much of the Holocene, the modeled glacier extent is similar to the present day extent. In this smaller state, ice flow is more rapid due to increased surface slope and is concentrated into steep and narrow valleys (e.g., the Seward Throat & the lower reaches of Hubbard Glacier), which are favorable for rapid erosion due to fast flow of thick ice. In addition, these valleys are likely underlain by heavily damaged bedrock, as they often trace major structures (regional thrust faults) and zones with abundant seismicity.

4.5.3 Is the EL a useful metric of erosion rate?

In an important paper providing the first documentation of the spatial distribution of exhumation rates in the St. Elias Orogen, Berger and Spotila (2008) brought attention to the apparent spatial relationship between zones of rapid erosion and the ELA position. However, caution is in order when considering this relationship for ice masses undergoing large changes in extent and thickness. Berger and Spotila (2008) define an ELA front, the zone between the modern and the LGM ELA, based on glacial geology studies in the interior of Alaska (Péwé, 1975). In projecting this ELA front onto modern topography, however, they neglect to account for the large increase in the elevation of the accumulation areas of the glaciers relative to the present day for the thick ice that covered the region over much of the last 115 kyr. In a study investigating the retreat of the Laurentide ice sheet, Hooke and Fastook (2007) used the UMISM model to calculate ice-sheet profiles at various times and showed that an ELA drop of less than 1 km displaced the equilibrium line position southward toward the glacier margin 600 km. Similarly, in SE Alaska a drop in ELA would displace

the equilibrium line southward, which is likely limited in the south because glaciers cannot extend into the Pacific beyond the edge of the shelf because of the efficient loss of ice where the terminus is in deep water. In Figure 4.6, we show the modern ELA and the average position of the equilibrium line during the last major glaciation representative of the Quaternary; it extends to near the edge of the shelf where the loss of ice due to calving in the open ocean vastly dominates other mass losses. We stress that, on average over much of the period exhumation, the equilibrium line is 10s of km offshore from the locus of rapid exhumation along the range-front and in the syntaxial corner. Hence, the ELA position on the modern landscape is not a useful indicator of the location of zones rapidly eroded by glaciers undergoing large changes in thickness. Moreover, ELA-based approaches suffer from general limitations; the location of the equilibrium line on large fluctuating glaciers is sensitive to the ice thickness changes, and hence is poorly known in the absence of numerical results with sufficient resolution to represent topographic control on ice flow, and it does not consider other factors controlling erosion rates aside from ice flux, including basal conditions and bedrock characteristic.

4.5.4 Implications for controls on erosion rates

This study and two others (Herman et al., 2015; Yanites and Ehlers, 2016) report relationships between rates of erosion and either glacier power, or glacier sliding (the latter two studies). In particular, using an approach that parallels ours, Yanites and Ehlers (2016) showed a general agreement between the spatial distribution of the temporally averaged sliding velocity over a glacier-interglacial cycle and exhumation rates based on thermochronometric data. They reported a linear relationship between rates of exhumation and a glacial erosion model based on sliding velocities; however, their results were also

consistent with the power-law relationship of erosion and glacial sliding similar to the result reported by Herman et al. (2015). Differences in the type of relationship (i.e., linear vs. power-law) indicate the sparse validation and point to need for additional studies. Drawing conclusions about the dominant process of glacial erosion (i.e., abrasion vs. quarrying) is likely premature especially considering the lack of information about bed characteristics including basal coupling. The glacier power model used in our study is, however, more general because it accounts for the sliding velocity and the strength of the coupling between the glacier and substrate, which is especially important in areas where water or soft-sediments underlie the glacier.

The proportionality factor in erosion laws, which are effectively indices of bedrock erodibility, and exponent are particularly uncertain (e.g., Herman et al., 2015). We expect the erodibility to be highly variable in space because of differences in lithology and bedrock strength. For the St. Elias Range, we define the erodibility as the ratio of erosion rate to glacier power, is 2.8 x 10-11 Pa-1 and ranges between 4.7 x 10-12 Pa-1 to 1.4 x 10-10 Pa-1, which yields the first validated and calibrated glacial erosion law based on glacier power for a tectonically active mountain range. We note that Herman et al. (2015) also validated their erosion model for basal sliding for a tectonically active range with modern glaciers, and did so with a promising novel approach but their results may not be robust; because of the very short duration (i.e., 5 months) of their study at Franz Joseph glacier, the results may not be representative of long-term erosion and the erosion rates inferred limited suspended sediment flux data could easily be confounded slight changes in sediment storage within the basin.

For comparison, we computed the bedrock erodibility for the Coast Range of British Columbia using results from Yanites and Ehlers (2016). We converted their modeled sliding velocities to glacier power per unit area assuming a constant basal shear stress of 105 Pa, a typical value for alpine glaciers (Cuffey and Paterson, 2010), which yields an erodibility constant of 5.6 x 10-13 Pa-1. The result is a 50-fold difference from our value of bedrock resistance to erosion; however, the difference may not be unreasonable considering the difference in material strength between the two study regions. Following the same approach, the erodibility constant for Herman et al. (2015) using glacier power is 6.6 x 10-10 Pa-1, which falls within our range of erodibility values. The range in erodibility constants likely relates to the local geology and tectonic history. At Franz Joseph Glacier, highly fractured bedrock borders the Alpine Fault; whereas, the Coast Range of British Columbia consists of relatively intact pre-Tertiary metamorphosed rock of a coherent crustal terrane and igneous plutons (Parrish, 1983). In SE Alaska there is a wide-range of rock types, including sedimentary rocks, that have a complex history of strain damage.

4.5.5 Model limitations and caveats

Our model addresses glacier evolution and erosion for a broad region over an entire 115-kyr cycle of glaciation; however, the model is simple and guided only by sparse observations and, hence, several limitations warrant attention.

The ice sheet model, UMISM, generates the spatial distribution of erosion rates broadly resolved both in space and time. The model uses a time step of 500 years and, hence, only low frequency temporal variations can be resolved. High frequency variations, including seasonal fluctuations in conditions and processes at the glacier bed that affect glacier sliding and erosion, are not resolved. In particular, the evolving pattern of subglacial

hydraulics, which changes on seasonal to glacial cycle time scales is known to cause large changes in effective stress (Merrand, 2013) and sliding velocity, both of which impact rates of quarrying (Iverson, 1991; Hallet, 1996) and evacuation of erosion-derived sediments. The model spatial resolution, 4 km, is adequate for defining the broader patterns of ice flow and glacial erosion; the corresponding spatial averaging is advantageous as the modeled erosion rates can be compared to exhumation rate data averaged over this length scale, decreasing the variability in data caused by the inherent variability in substrate characteristics (e.g., lithology and damage density, differential uplift, and bed roughness). Most of the elements of the alpine topography are, however, below the model resolution.

The long-term ice sheet model also does not take into account changes in 1) climatology due to the growth and decay of large ice masses, 2) local sea level due to crustal loading by ice and sediments, 3) transients, including glacial surges, and 4) bed elevation due to erosion and deposition over a full glacial cycle lasting >105 years, and yet, even with the 104 years of the Holocene, sedimentation on the shelf reaches up to nearly 300 m locally (Worthington et al., 2010).

For the relationship between exhumation and glacier power, we focus on regions that are currently glaciated and have been glaciated throughout the entire glaciation; however, there are a few domains where exhumation is fast in currently unglaciated areas (e.g., Berger et al., 2008) but erosion is known to extend well beyond the glaciers to the topographic divides due to avalanches and other subaerial mass wasting processes. Moreover, the analysis focuses on the principal glaciers; it does not include smaller glaciers, such as Tyndall Glacier in Icy Bay that is currently eroding at 10 mm/yr or more (Koppes and Hallet, 2006) and the associated mass wasting. The latter includes the massive landslide that

collapsed recently on the terminus of Tyndall Glacier (October 17, 2015; http://www.ldeo.columbia.edu/news-events/detecting-landslides-few-seismic-wiggles). In addition, the exhumation signal is blurred spatially by the northward crustal advection due to high convergence rates, 20-30 mm/yr, across the St. Elias range (Elliot et al., 2013). Nevertheless, the long-term model constitutes a powerful and rarely used tool for examining tectonic-glacier interactions and for interpreting results from exhumation studies.

4.6 Conclusions

The St. Elias range in SE Alaska is an ideal region for examining the spatial variation in glacial erosion rates for both the contemporary state of the glaciers, and for the fluctuating states through major glaciations typical of the late Quaternary. Moreover, a wealth of existing data sheds light on glacial and erosional processes, on the complex geologic and geophysical setting that can affect bedrock resistance and erosion, and on the tempo of exhumation throughout the study region. Importantly, the region is also home to the largest and most erosive alpine glaciers on the planet. They provide valuable guidance for the parameterization in the ice-sheet model and for validating the results. We find a significant linear relationship between average glacier power per unit area and exhumation; the averaging here is temporal and over a full ~100-kyr glacial cycle typical of the late Quaternary. The variation in glacier power accounts for ~70% of the observed range of observed exhumation rates despite the large range of substrate characteristics expected in the study region. The results validate the hypothesis that the rate of erosion scales with the glacier power, and provide calibration for the St Elias range. Compared to regions with coherent bedrock (i.e., the Coast Range of BC), bedrock erodibility is relatively high 2.8 x 10-11 Pa-1 due to the local crustal assemblage consisting of either weakly lithified sediments

or diverse metamorphic and plutonic rocks that have been pervasively weakened by large strains.

Model results also dispel the notion that zones of rapid exhumation are spatially coincident with the position of the EL; over much of the model duration, the average position of the EL is displaced horizontally well south of zones of rapid exhumation, near the continental shelf break in the Gulf of Alaska. According to the model, rapid erosion is currently concentrated into two clear regions, the Seward Throat and the lower reaches of Hubbard Glacier. They coincide closely with areas of rapid exhumation (e.g., Enkelmann et al., 2015; 2017). Regionally, the highest rates of exhumation and basal energy expenditure occur in the eastern portion of the orogen near the transition from strike-slip motion along the Fairweather fault to convergence along the Chugach-St. Elias fault.

Figures for Chapter 4

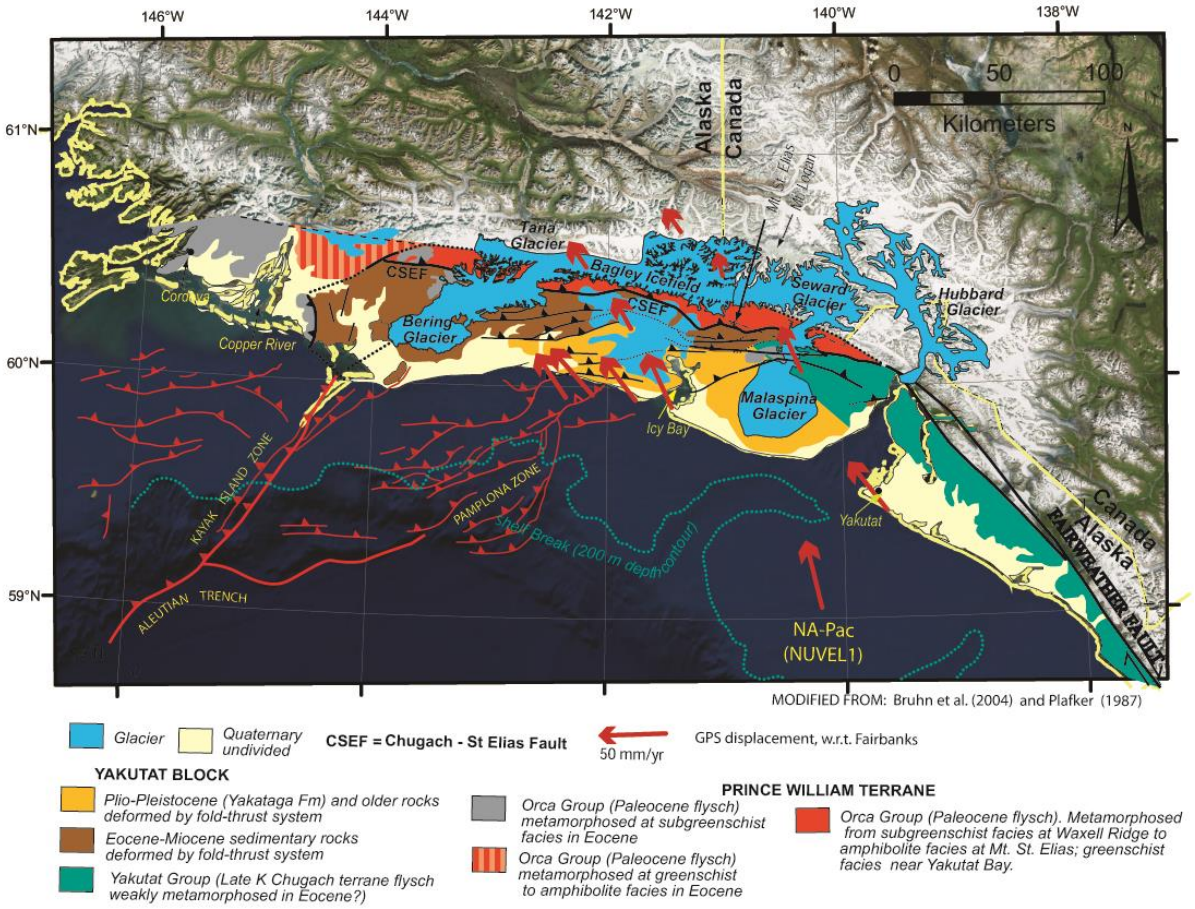

Figure 4.1. Geologic map of SE Alaska with major geological units, onshore and offshore faults, major glaciers, and geographic locations. GPS displacements, red arrows, Elliot et al., 2013.

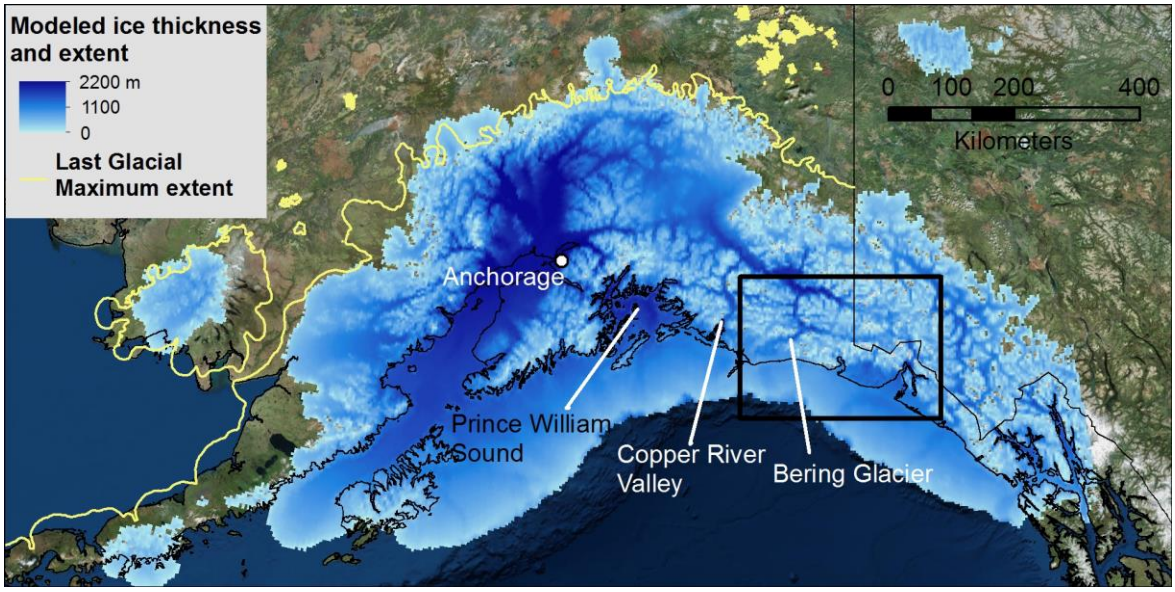

Figure 4.2. Modeled ice thickness at maximum glacier extent. Mapped extent of LGM glacier limit shown as solid yellow line (Manley and Kaufman, 2002) and solid black line indicates international boundary and modern shoreline. The black box locate the areas shown in Figs. 4.4 and 4.7. Major geographic features shown for reference.

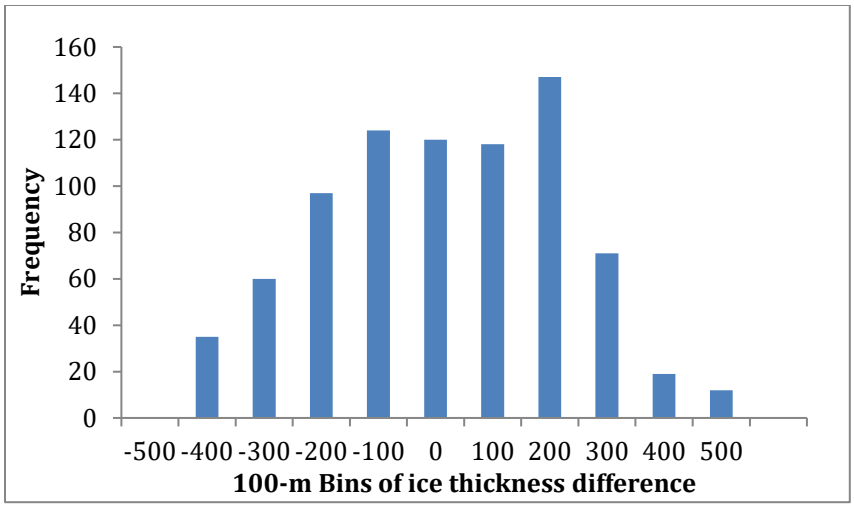

Figure 4.3. Histogram of ice-thickness differences between modeled values for current conditions and low-frequency radar derived measurements of ice thickness (Rignot et al., 2013). A positive value indicates that the modeled glaciers are thicker.

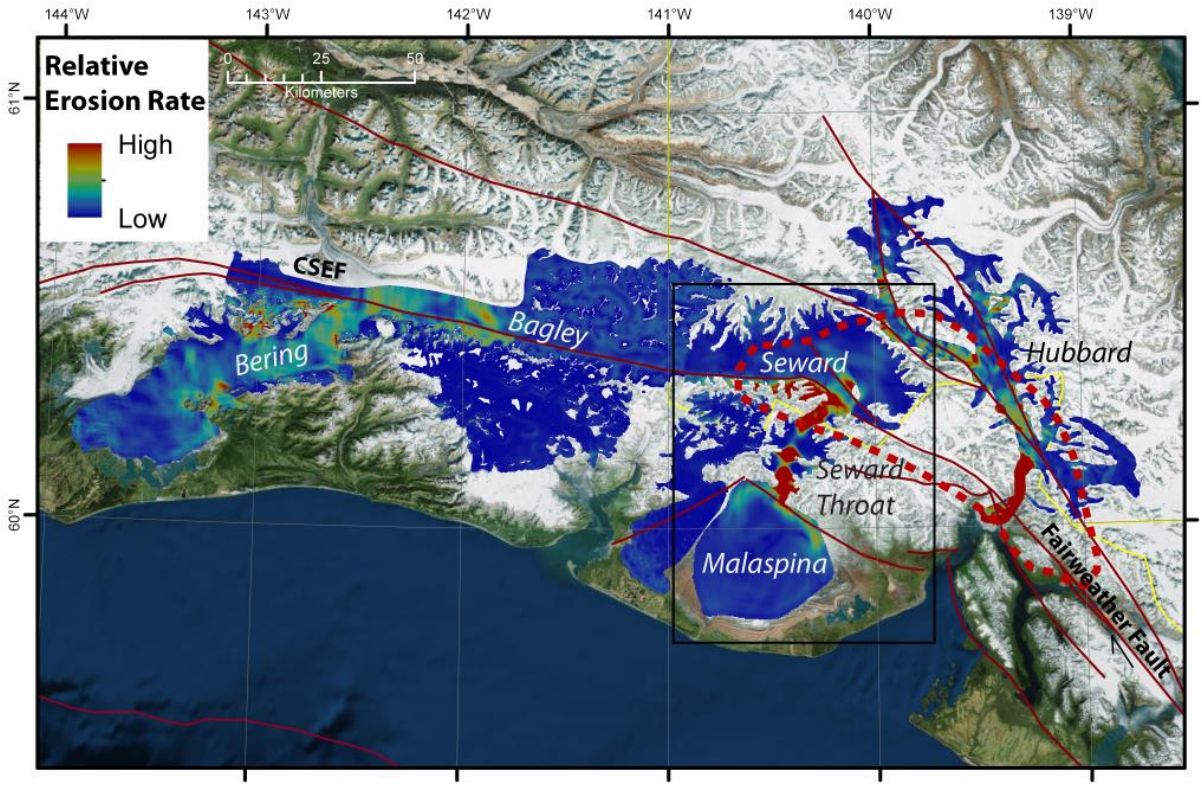

Figure 4.4. Distribution of the relative erosion rate based on the glacial power derived for the principal glaciers using their current geometry and mass balance. The area of rapid exhumation reported by Enkelmann et al. (2015) is outlined with heavy red dashes. Onshore, red lines represent major faults including the Fairweather and Chugach-Saint Elias Faults. Offshore, the thin red line shows the LGM extent of glacial ice (Manley and Kaufman, 2002). The black box is the area in Figure 4.5. Base map from ESRI World Imagery: Esri, DigitalGlobe, GeoEye, i-cubed, USDA FSA, USGS, AEX, Getmapping, Aerogrid, IGN, IGP, swisstopo and the GIS User Community.

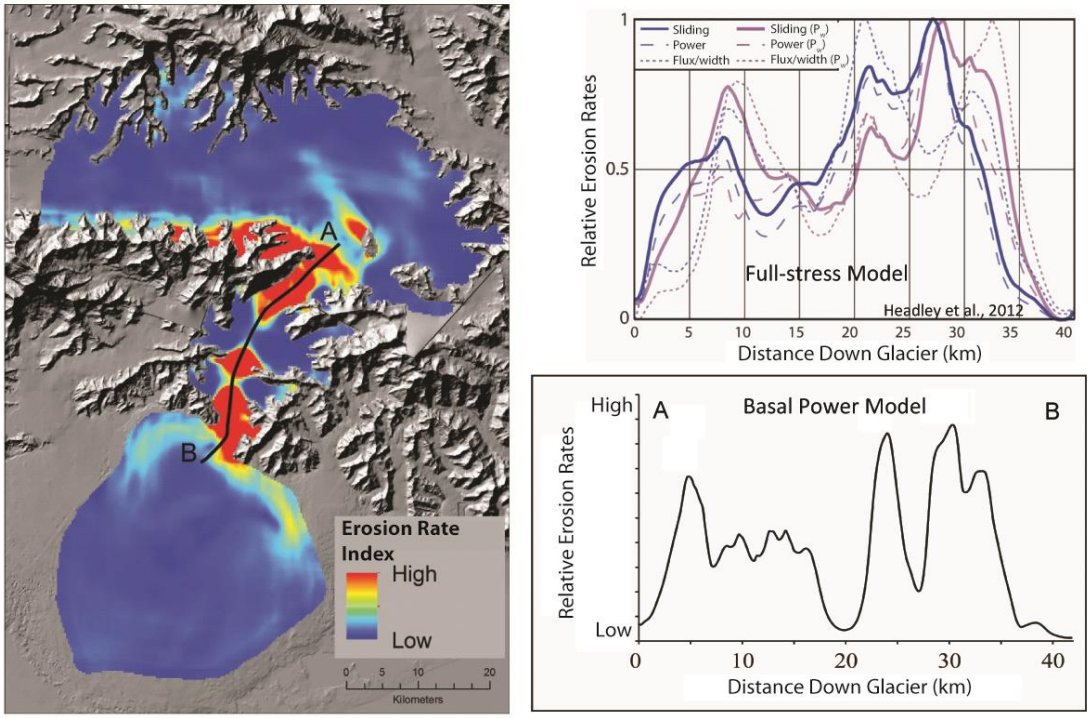

Figure 4.5. Comparison of relative erosion rates, normalized to the maximum value, for the Seward Throat. Top-right: Relative erosion rates for multiple erosion rules computed in a higher order model and, in general, show three peaks through the throat (Headley et al., 2012). Bottom-right: The glacier power from this study, which also shows three peaks in the same relative position as the more complex model.

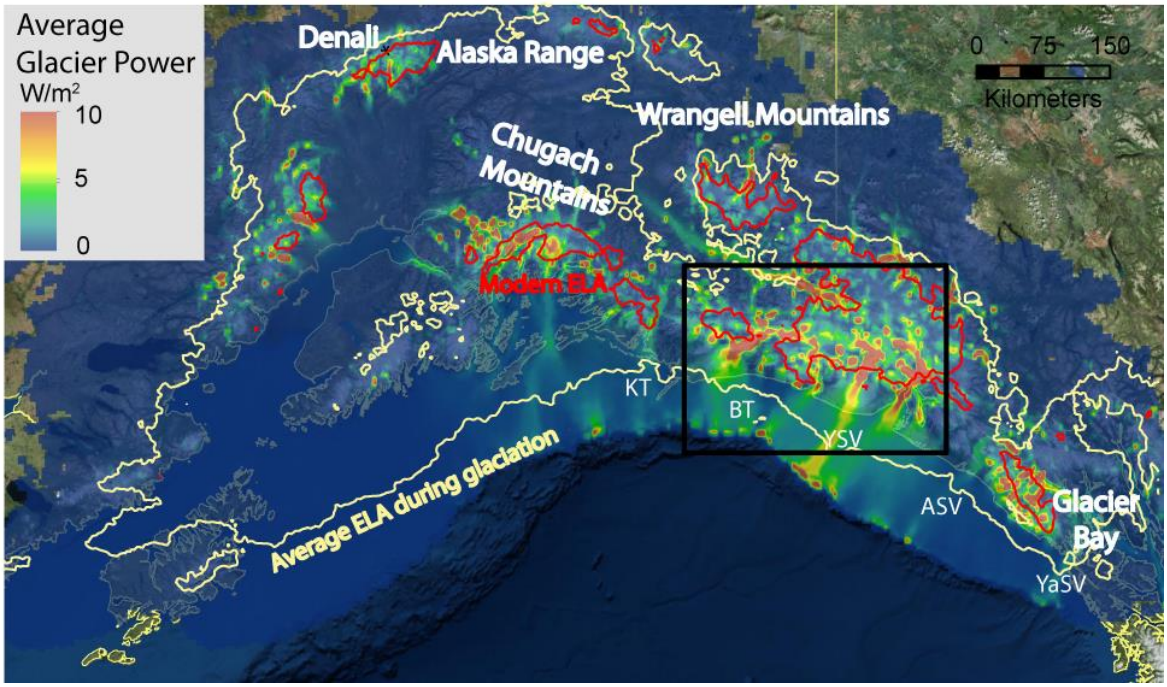

Figure 4.6. Spatial distribution of the time-averaged glacier power through a major glaciation. Hot colors indicate areas where much energy is available to drive erosion, and hence, where erosion in bedrock areas is expected to be rapid. Yellow lines show the modern shoreline and USA-Canada national boundary and the black box shows the area of Figures 4.1 and 4.7. Sea valleys and glacial shelf-crossing troughs are abbreviated as: ASV—Alsek Sea Valley; BT—Bering Trough; KT—Kayak Trough; YSV—Yakutat Sea Valley; YaSV—Yakobi Sea Valley (Elmore et al., 2013). Irregular lines show the modern ELA, in red, and time-average ELA, in yellow, over the full glaciation.

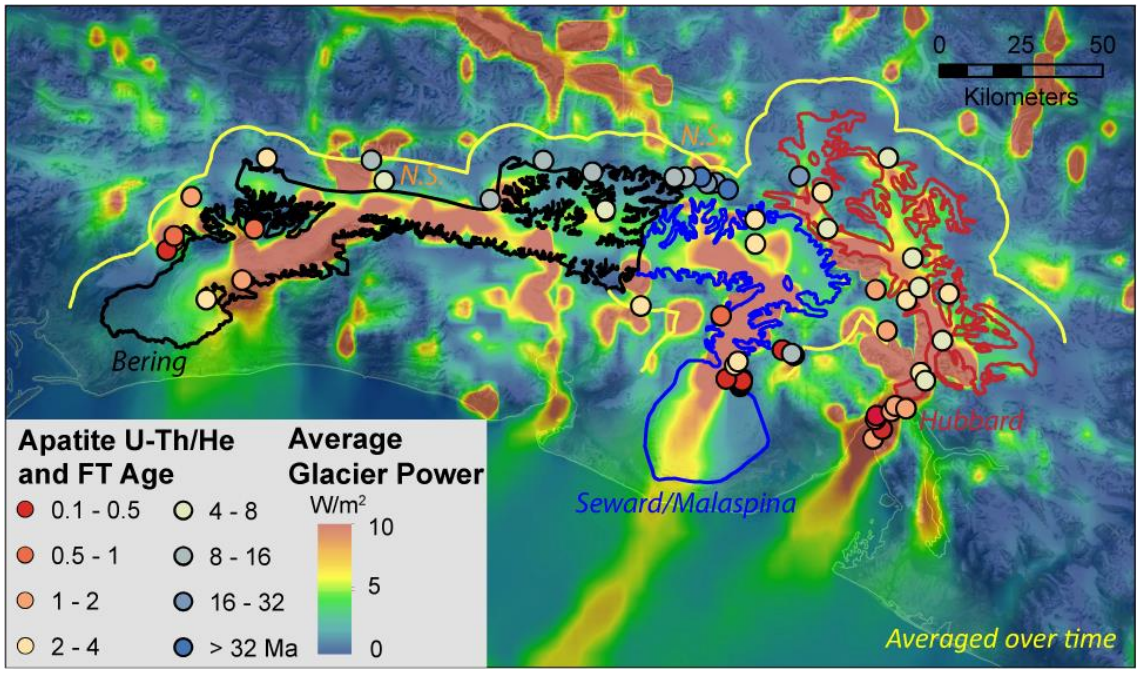

Figure 4.7. Glacier power, an index of the time-averaged erosion rate, during a complete glaciation, and exhumation rate data for the same region as shown in Figure 4.1. Colored dots are bedrock and detrital apatite U-Th/He and fission track ages from Enkelmann et al. (2015). Ages that overlap the modern glacier boundaries (shown as solid black lines) or those within a 10-km buffer zone (yellow line) are shown. The red star near the Hubbard terminus shows the location for which the basal characteristics were tracked through time in Figure 4.8.

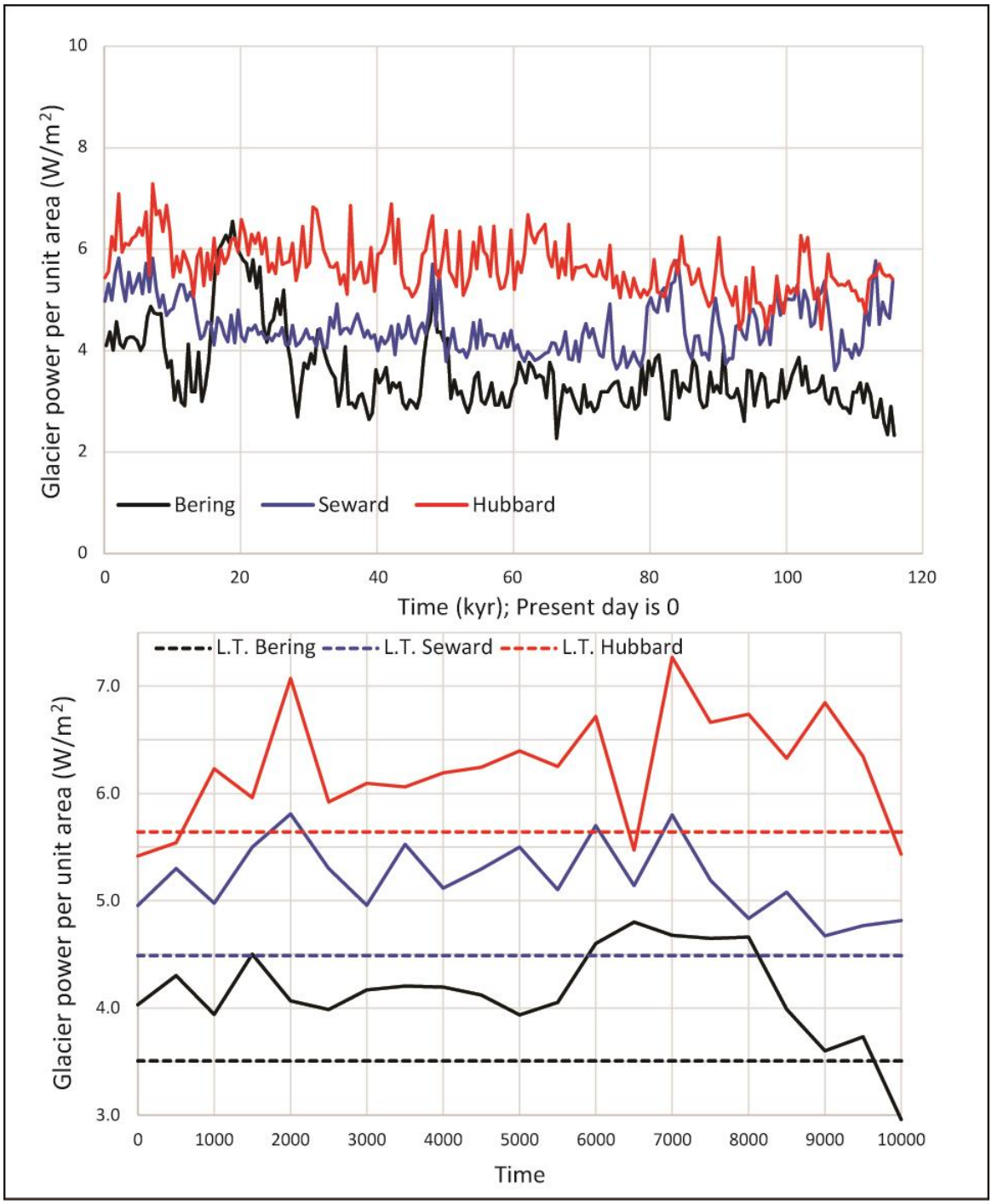

Figure 4.8. <u>Upper panel</u>: Time-series of glacial power for the three principal glacier basins. Present-day corresponds to time 0. <u>Lower panel</u>: Time-series for the last 10k years along with the long-term average (dotted line).

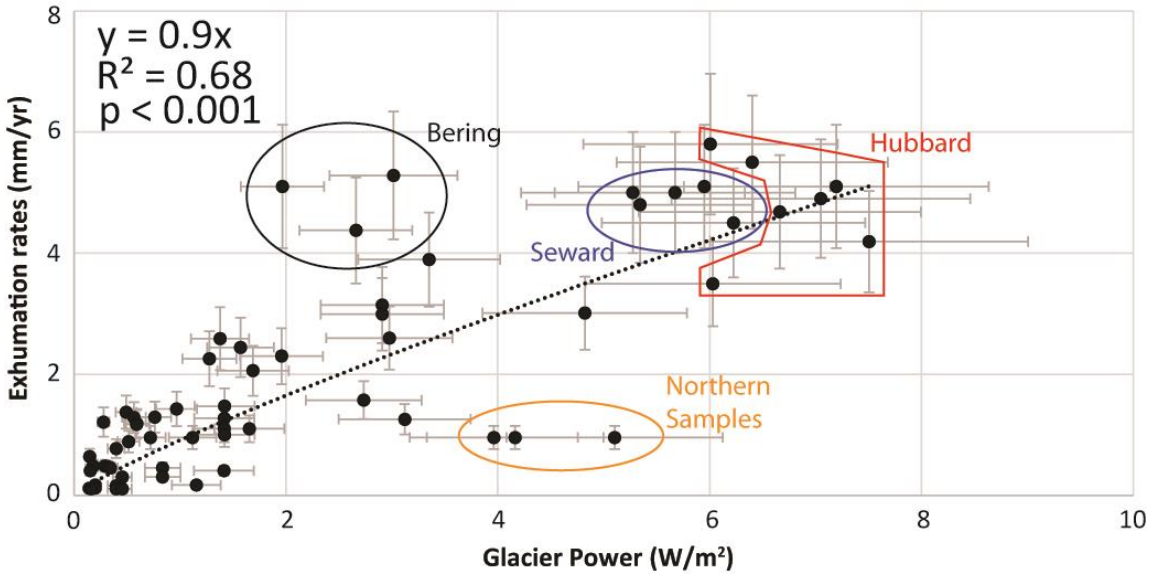

Figure 4.9. Glacier power averaged over 115 kyr, the duration of the last major cycle, versus exhumation rates for nearby sites derived from apatite U-Th/He and fission track ages from Enkelmann et al. (2015). The regression equation expresses the relationship between the exhumation rate, y, based on thermochronological estimates, and the modeled glacier power per unit area, x, averaged over a full glacial cycle.

Chapter 5: Summary and conclusions

5.1 Tempo of erosion at the top of the world

In Chapter 2, I investigated the rate at which ice sculpts the highest parts of our globe, and considered the co-evolution of valley glaciers and topography. Much as the flow of the glaciers is sustained by snow accumulation at high elevations, the downvalley movement of ice-entrained debris is sustained by input of debris to the glaciers. This input must result from glacial and periglacial erosion of the catchment. In the Mount Everest area, and other regions with glaciers deeply covered in debris, a substantial portion of the products of erosion accumulates on the lower reaches of the glacier and is deposited locally, filling in the valley and forming a massive moraine complex that typically initiated in the early Holocene. In less arid glaciated areas (e.g., SE Alaska), the glaciers flow faster due to greater snow accumulation and more debris is lost from the basin being flushed away in meltwater streams and rivers.

In order to determine erosion rates, I spent several field seasons in Nepal collecting data and field checking observations derived from remote sensing data. A significant dataset resulting from this work is the downglacier variation in debris thickness, which was used in Chapters 2 to determine the surface debris flux and in Chapter 3 to establish a relationship between ice melt and debris thickness. I determined the debris thickness using a variety of techniques including geophysical imaging techniques (i.e., electrical resistivity tomography and ground-penetrating radar), as well as direct visual observations. Other fieldwork included monitoring stream discharge and suspended sediment flux in the proglacial stream, and measuring surface albedo, temperature gradients in the surface debris, and surface displacements with sequential GPS surveys.

Two surprises emerged from my study. First, erosion rates are similar to exhumation rates, and they show no significant changes over time scales ranging from 10 to 107 years. Taken together with paleo-elevation evidence that shows an absence of long-term surface uplift, the results suggest a self-organized balance achieved as the surface and tectonic systems mutually adjust to remove rock mass from the crest of the range at roughly the same rate as the rock uplift. The second surprise wat that over the last 104 years, the bulk of debris produced by erosion remains under and in the vicinity of Khumbu Glacier, suggesting that although erosion rates of the basin do not vary appreciably in time, debris evacuation and transfer down valley are likely be highly variable in time and peak during major glacial advances. The current accumulation of debris beneath Khumbu Glacier represents a sink of supraglacial debris that curtails the accumulation of debris on the glacier surface; as this is likely representative of other glaciers in the region, this basal debris accumulation, has important implications for estimates of ice volumes, and predictions of glacier evolution and future fresh-water resources.

5.2 Debris-covered glaciers and climate change

In Chapter 3, I investigated how debris-laden glaciers respond to their changing environment. Beyond the fundamental scientific interest in glacier response to climate change, understanding the future of debris-covered glaciers has important practical consequences, including fresh-water availability, global sea-level change, and environmental hazards. Moreover, the study quantitatively addressed unexpected observations by Kääb et al. (2012) that thinning of debris-covered glaciers over a 5-year span was not statistically different from thinning of relatively debris-free (clean) glaciers. To investigate this “debris-covered glacier anomaly”, as well as the behavior of Khumbu Glacier, I developed an ice-

flow model that is coupled with surficial and internal debris. I validated the model using the former glacier extents and thicknesses that are well recorded by the lateral moraines, as well as considerable field measurements of debris thickness and surface displacements using GPD, remote sensing studies, and DEM analysis. My approach parallels Rowan et al. (2015), who developed a model that used the Little Ice Age (LIA) moraines as a steady-state target; however, in my study, I calibrated the model using both the LIA and the Last Glacial Maximum (LGM) moraines and leveraged significant field measurements.

The study further departs from other debris-covered glacier modeling studies in that I developed a new relationship between debris thickness and the rate of ice melting. The approach assumed that the long-recognized insulating effect of debris acts on local scales of continuous debris cover, but not over the scale of the entire debris-covered tongue where ice loss is rapid due to thermokarst processes. This is important because the rough, thick cover layer of debris of Khumbu Glacier likely reflects this behavior. The relationship was quantified using existing and new observations of thinning rates, surface velocity, and the thickness of both ice and debris. It reflects processes occurring on a scale larger than the distinct thermokarst roughness elements; thus, it is named the "large-scale melt rule".

Results of the glacier-flow model illuminate the overall influence of surface debris and sinks of debris on the evolution of both the glacier and the surface debris thickness and character (i.e., continuous or interspersed with thermokarst features). Model results suggest that when the climate is unfavorable for glacier growth and ice motion is relatively slow, the debris influence on melting rates is best modeled using the large-scale melt rule that yields relatively rapid melting even under thick debris due to enhanced melting from exposed ice cliffs, surface lakes, and englacial water conduits. Under more favorable conditions, during

steady periods or advances, such as during the LGM, the best fit between simulation and records of past extent and ELA required the use of a local-melt rule, as used in most other debris-covered glacier models.

For the entire glacier, from the LIA to the present the volume loss modeled using the large-scale rule is 20% of the LIA volume. This calculated volume loss is comparable to the actual loss, 17%, estimated using the surface lowering from the LIA moraines to the modern surface and neglecting the very slight glacial retreat since the LIA. In contrast, Rowan et al. (2015) predicted a volume change of 38% and unrealistically large ice retreat from the LIA to the present. Assuming no further climate change, they predict a further loss of 8-10% of the present-day glacier volume by AD2100. I predict a slightly smaller ice loss, about 6% volume change by AD2100, largely in the central part of the glacier, and little change in the terminus ice thickness and extent.

This study is the first to define quantitatively the influence of a thick debris cover, exceeding a few decimeters in thickness, on the melt rate. Relative to the insulating influence of a thin cover of debris, melting is enhanced primarily due to thermokarst processes that contribute to the debris-covered glacier anomaly. Since the LIA, the glacier has thinned at rates averaging 0.4 m w.e./yr indicating that there is no apparent acceleration in glacier shrinkage and, importantly, Khumbu Glacier will continue to thin until at least AD2300. Thinning near the terminus is considerably slower, ~0.1 to 0.15 m w.e./yr, and matches GPS measured rates of surface lowering for the same region. Model results agree with other studies in general (Shea et al., 2015; Rowan et al., 2015), but differ in detail: they all suggest that under the present climatic trend, the glacier will thin for at least the next one hundred years and likely beyond.

5.3 Spatial distribution of erosion rates in SE Alaska

In Chapter 4, I considered the spatial and temporal distribution of glacial erosion rates in SE Alaska. The study benefitted from published estimates of glacial erosion that were estimated using diverse methods including monitoring sediment yields from streams, estimating offshore sediment volumes, and using thermochronometric methods. Members of the multidisciplinary Saint Elias Erosion/tectonic Project (STEEP), which included several researchers from the University of Washington, laid much of the strong foundation of work. Despite the wealth of data, major gaps in our knowledge remain and invalidated speculations exist in the literature. For example, the general spatial correlation between the inferred long-term position of the equilibrium line (ELA) and zones of rapid exhumation has been used to suggest that the two are interrelated. Such suggestions, however, are not sound because they do not consider the large variations in the location of the equilibrium line over major glacial cycles, or in erosion rates within individual basins.

The aim of my SE Alaska study was to develop numerical models of glacial erosion in collaboration with the University of Maine to advance understanding of the rate of glacial erosion, and hence sediment production, on the orogen scale as a function of glacier characteristics. My part in the project led to the development of two models. The first, the contemporary model, led to the first orogen-wide spatially continuous index of erosion rates, which was hypothesized to be glacier power per unit area; it is the product of the speed of basal motion and the strength of the glacier-bed coupling. In the model, the balance flux and glacier surface slope were used as proxies for basal motion and bed coupling, respectively. Results show that erosion is concentrated into two clear hotspots corresponding to the Seward Throat and Hubbard Terminus, which coincides with areas where exhumation is

rapid (Enkelmann et al., 2015). At the Seward Throat, the model was validated with and showed remarkable agreement with a full-stress model developed by Headley et al. (2012).

Whereas the contemporary model was based on the current configuration of glaciers, the long-term model considers the state of, and erosion by, the much larger ice masses that likely prevailed over much of the Quaternary. For this model, I calculated the glacier power field as the product of the basal ice velocity and basal shear stress at discrete times for the entire orogen as the glacier systems grow and shrink through a full 100-kyr glacial cycle. The late Quaternary evolution and dynamics of the northern sector of the Cordilleran Ice Sheet were simulated using the University of Maine Ice-Sheet Model, UMISM. Long-term model results show that, in general, for the principal glaciers in the range basin-wide averaged erosion rates are relatively constant in time, and that the location of rapidly eroding domains is relatively stable due to topographic controls despite the large glacier fluctuations. These domains of rapid erosion do not spatially correlate with the time-averaged position of the equilibrium line.

An important outcome of this work is a novel glacial erosion rule, which contrasts with comparable rules in the literature in two ways. First, this new rule relates erosion rates to glacier power per unit area, whereas, in other studies, the erosion rate is generally assumed to scale with the sliding rate. Second, whereas existing rules and models generally lack both validation or calibration, the novel rule was validated and calibrated using published exhumation rates; using this rule, glacier power accounts for ~70% of the observed range of observed exhumation rates despite the diversity of geologic terrains and large range of substrate characteristics expected in the study region. The proportionality factor in our erosion law, effectively an index of bedrock erodibility, is 2.8 x 10-11 Pa-1, yielding the first

validated and calibrated glacial erosion law based on glacier power for a tectonically active mountain range.

5.4 Summary

This thesis strives to shed light on glacial erosion in two settings using diverse methods and techniques. At Khumbu Glacier, Nepal, erosion of the catchment has on average maintained a steady pace over the past 10^4 yr. Moreover, the rate of erosion is similar to published long-term (O ~ 10^7 yr) exhumation rates derived from thermochronometric data in the Khumbu region. In the course of this research, I also became interested in the long-term storage of debris in the upper catchment and episodic evacuation, and in the role of the eroded material on the response of the glacier to climate change, which I explored using a numerical model. The results are the first to address the debris-covered glacier anomaly quantitatively. In Alaska, my work led to the first validated and calibrated glacial erosion rule based on glacier power, and the first spatially continuous determination of the distribution of glacial erosion rates for an entire orogen averaged over a major glacial cycle.

Bibliography

Adhikari, S. and P. Huybrechts, Numerical modelling of historical front variations and the 21st-century evolution of glacier AX010, Nepal Himalaya, Ann. Glaciol., 50(52), 27-34, (2009).

Alley, R.B., D.E. Lawson, E.B. Evenson, G.J. Larson, Sediment, glaciohydraulic supercooling, and fast glacier flow, Ann. Glaciol., 36(1), 135-141, (2003).

Anandakrishnan S., D.D. Blankenship, R.B. Alley, P.L. Stoffa, Influence of subglacial geology on the position of a West Antarctic ice stream from seismic observations, Nature, 394, 62-65, (1998).

Anderson, L.S. and R.S. Anderson, Modeling debris-covered glaciers: response to steady debris deposition, The Cryosphere, 10(3), 1105-1124, doi: 10.5194/tc-10-1105-2016, (2016).

Anderson, R.S., A model of ablation-dominated medial moraines and the generation of debris-mantled glacier snouts, J. Glaciol., 46(154), 459-469, (2000).

Anderson, R.S., P. Molnar, M.A. Kessler, Features of glacial valley profiles simply explained, J. Geophys. Res., 111, (2006).

Asahi, K., Equilibrium-line altitudes of the present and Last Glacial Maximum in the eastern Nepal Himalayas and their implications for SW monsoon climate, Quatern. Int., 212(1), 26-34, (2010).

Barclay, D.J., G.C. Wiles, P.E. Calkin, Holocene glacier fluctuations in Alaska, Quaternary Sci. Rev., 28, 2034-2048, (2009).

Barnard, P.L., L.A. Owen, R.C. Finkel, Quaternary fans and terraces in the Khumbu Himal south of Mount Everest: their characteristics, age and formation, J. Geol. Soc., 163, 383-399, (2006).

Barnard, P.L., L.A. Owen, R.C. Finkel, K. Asahi, Landscape response to deglaciation in a high relief, monsoon-influenced alpine environment, Langtang Himal, Nepal, Quaternary Sci. Rev., 25, 2162-2176, (2006).

Beaumont, C., R.A. Jamieson, M.H. Nguyen, B. Lee, Himalayan tectonics explained by extrusion of a low-viscosity crustal channel coupled to focused surface denudation, Nature, 414, 738-742, (2001).

Benn, D.I., N. Hulton, R. Mottram, "Calving laws", 'sliding laws' and the stability of tidewater glaciers, Ann. Glaciol., 46, 123-130, (2007).

Benn, D.I. and A. Evans, Glaciers and Glaciation, Arnold Publishing, London, Ed. 2, (2010).

Benn, D., T. Bolch, K. Hands, J. Gulley, A. Luckman, L. Nicholson, D. Quincey, S. Thompson, R. Toumi, S. Wiseman, Response of debris-covered glaciers in the Mount Everest region to recent warming, and implications for outburst flood hazards, Earth-Sci. Rev., 114(1), 156-174, (2012).

Berger, A.L. and J.A. Spotila, Denudation and deformation in a glaciated orogenic wedge: The St. Elias orogen, Alaska, Geology, v. 36, p. 523-526, (2008).

Berger, A.L., J.A. Spotila, J. Chapman, T.L. Pavlis, E. Enkelmann, N.A. Ruppert, J.T. Buscher, Architecture, kinematics, and exhumation of a convergent orogenic wedge: A thermochronological Investigation of tectonic-climatic interactions within the central St. Elias Orogen, Alaska: Earth Planet. Sci. Lett., v. 270, p. 13-24, (2008).

Birkel, S.D., A.E. Putnam, G.H. Denton, P.O. Koons, J.L. Fastook, D.E. Putnam, K.A. Maasch, Climate Inferences from a Glaciological Reconstruction of the Late Pleistocene Wind River Ice Cap, Wind River Range, Wyoming, Arct. Antarct. Alp. Res., 44, 265-276, (2012).

Bolch, T., M.F. Buchroithner, J. Peters, M. Baessler, S. Bajracharya, Identification of glacier motion and potentially dangerous glacial lakes in the Mt. Everest region/Nepal using spaceborne imagery, Nat. Hazards, 8(6), 1329-1340, doi: 10.5194/nhess-8-1329-2008, (2008a).

Bolch, T., M. Buchroithner, T. Pieczonka, A. Kunert, Planimetric and volumetric glacier changes in the Khumbu Himal, Nepal, since 1962 using Corona, Landsat TM and ASTER data, J. Glaciol., 54(187), 592-600, (2008b).

Bolch, T., T. Pieczonka, D.I. Benn, Multi-decadal mass loss of glaciers in the Everest area (Nepal Himalaya) derived from stereo imagery, The Cryosphere, 5(2), 349-358, doi: 10.5194/tc-5-349-2011, (2011).

Bolch, T., A. Kulkarni, A. Kaab, C. Huggel, F. Paul, J.G. Cogley, H. Frey, J.S. Kargel, K. Fujita, M. Scheel, S. Bajracharya, M. Stoffel, The state and fate of Himalayan glaciers, Science, 336(6079), 310-314, doi: 10.1126/science.1215828, (2012).

Bookhagen, B., D. Fleitmann, K. Nishiizumi, M.R. Strecker, R.C. Thiede, Holocene monsoonal dynamics and fluvial terrace formation in the northwest Himalaya, India, Geology, 34(7), 601-604, (2006).

Bollasina, M., L. Bertolani, G. Tartari, Meteorological observations in the Khumbu Valley, Nepal Himalayas, 1994-1999, Bull. Glac. Res., 19, 1-11, (2002).

Boulton, G.S., Processes and patterns of glacial erosion, in Glacial Geomorphology, edited by D.R. Coates, Allen and Unwin, St. Leonards, N.S.W., Australia, (1974).

Braithwaite, R.J., V.P. Singh, (Ed.), U.K. Haritashya, (Ed.), Degree-days, In Encyclopedia of snow, ice and glaciers, Springer-Verlag, (2011).

Braithwaite, R.J. and O.B. Olesen, Detection of climate signal by inter-stake correlations of annual ablation data Qamanarssup Sermia, West Greenland, J. of Glaciol., 35(120), 253-259, (1989).

Brandon, M.T., M.K. Roden-Tice, J.I. Garver, Late Cenozoic exhumation of the Cascadia accretionary wedge in the Olympic Mountains, northwest Washington State, Geol. Soc. Am. Bull., 110, 985-1009, (1998).

Braun, J., D. Zwartz, J. Tomkin, A new surface-processes model combining glacial and fluvial erosion, Ann. Glaciol., 28, 282-290, (1999).

Brewer, I.D., D.W. Burbank, K. V. Hodges, Downstream development of a detrital cooling-age signal: Insights from 40Ar/39Ar muscovite thermochronology in the Nepalese Himalaya, Geol. Soc. Am. Spec. Paper, 398, 321-338, (2006).

Briner, J.P. and T.W. Swanson, Using inherited cosmogenic ^{36}Cl to constrain glacial erosin rates of the Cordilleran ice sheet, Geology, 26, 3-6, (1998).

Bruhn, R.L., T.L. Pavlis, G. Plafker, L. Serpa, Deformation during terrane accretion in the Saint Elias orogen, Alaska, Geol. Soc. Am. Bull., 116, 771-787, (2004).

Bruhn, R.L., R.R. Forster, A.L.J. Ford, T.L. Pavlis, M. Vorkink, Structural geology and glacier dynamics, Bering and Stellar Glaciers, Alaska, *in* Shuchman, R.A. and E.G. Josberger, eds., Bering Glacier, interdisciplinary studies of earth's largest temperate glacier, Geol. Soc. Am. Spec. Paper, 462, 217-233, (2010).

Bruhn, R.L., J. Sauber, M.M. Cotton, T.L. Pavlis, E. Burgess, N. Ruppert, R.R. Forster, Plate margin deformation and active tectonics along the northern edge of the Yakutat Terrane in the Saint Elias Orogen, Alaska and Yukon, Canada, Geosphere, 8, 1384-1407, (2012).

Burbank, D.W., J. Leland, E. Fielding, R.S. Anderson, N. Brozovic, M.R. Reid, C. Duncan, Bedrock incision, rock uplift and threshold hillslopes in the northwestern Himalayas, Nature, 379, 505-510, (1996).

Burbank D.W., A.E. Blythe, J. Putkonen, B. Pratt-Sitaula, E. Gabet, M. Oskin, A. Barros, T.P. Ojha, Decoupling of erosion and precipitation in the Himalayas, Nature, 426, 652-655, (2003).

Burbank D.W., B. Bookhagen, E. J. Gabet, J. Putkonen, Modern climate and erosion in the Himalaya, C. R. Geosci., 344, 610-626, (2012).

Burgess, E.W., R.R. Forster, C.F. Larsen, Flow velocities of Alaskan glaciers, Nat Commun., 4, (2013).

Casey, K.A., A. Kääb, D.I. Benn, Geochemical characterization of supraglacial debris via in situ and optical remote sensing methods: a case study in Khumbu Himalaya, Nepal, The Cryosphere, 6, 85-100, (2012).

Chamberlain, T.C., The rock-scorings of the great ice invasion, U.S. Geol. Survey, Seventh Ann. Rept., 197-200, (1885).

Clark, M.K., L. M. Schoenbohm, L.H. Royden, K.X. Whipple, B.C. Burchfiel, X. Zhang, W. Tang, E. Wang, L. Chen, Surface uplift, tectonics, and erosion of eastern Tibet from large-scale drainage patterns, Tectonics, 23, (2004).

Clark, P.U., A.S. Dyke, J.D. Shakun, A.E. Carlson, J. Clark, B. Wohlfarth, J.X. Mitrovica, S.W. Hostetler, A.M. McCabe, The Last Glacial Maximum, Science, 325(5941), 710-714, doi: 10.1126/science.1172873, (2009).

Cohen, D., T.S. Hooyer, N.R. Iverson, J.F. Thomason, M. Jackson, Role of transient water pressure in quarrying: A subglacial experiment using acoustic emissions, J. Geophys. Res., 111, (2006).

Conway, H. and L.A. Rasmussen, Summer temperature profiles within supraglacial debris on Khumbu Glacier, Nepal, in: Debris-covered Glaciers, IAHS Publ., (2000).

Cottle, J.M., M.J. Jessup, D.L. Newell, M.P. Searle, R.D. Law, M.S.A. Horstwood, Structural insights into the early stages of exhumation along an orogen-scale detachment: The south Tibetan detachment system, Dzakaa Chu section, eastern Himalaya, J. Struct. Geol., 29, 1781–1797, (2007).

Cottle, J.M., M.P. Searle, M.S.A. Horstwood, D.J. Waters, Timing of midcrustal metamorphism, melting and deformation in the Mount Everest region of southern Tibet revealed by U (-Th)-Pb geochronology, J. Geol., 117, 643–664, (2009).

Cottle, J.M., D.J. Waters, D. Riley, O. Beyssac, M.J. Jessup, Metamorphic history of the south Tibetan detachment system, Mt. Everest region, revealed by RSCM thermometry and phase equilibria modeling, J. Metamorph. Geol., 29, 561–582, (2011).

Cowan, E.A., K.C. Seramur, R.D. Powell, B.A. Willems, S.P.S. Gulick, J.M. Jaeger, Fjords as temporary sediment traps: History of glacial erosion and deposition in Muir Inlet, Glacier Bay National Park, southeastern Alaska, Geol. Soc. Am. Bull., 122, 1067-1080, (2010).

Cuffey, K.M. and W.S.B. Paterson, The physics of glaciers, Academic Press, (2010).

Daly, C., G. Taylor, W. Gibson, The PRISM Approach to Mapping Precipitation and Temperature, 10th Conf. on Applied Climatology, Reno, NV, American Meteorological Society, 10-12, (1997).

Dodson, M.H., Closure temperature in cooling geochronological and petrological systems, Contrib. Mineral. Petr., 40(3), 259-274, (1973).

Egholm, D.L., S.B Nielson, V.K. Pedersen, J.-E. Lesemann, Glacial effects limiting mountain height, Nature, 460, 884-887, (2009).

Egholm, D.L., M.F. Knudsen, C.D. Clark, J.E. Lesemann, Modeling the flow of glaciers in steep terrains: The integrated second-order shallow ice approximation (iSOSIA), J. Geophys. Res., 116, F02012, doi: 10.1029/2010JF001900, (2011).

Elhers, T.A. and K.A. Farley, Apatite (U-Th)/He thermochronometry: methods and applications to problems in tectonic and surface processes, Earth Planet. Sci. Lett., 206, 1-14, (2003).

Elliott, J., J.T. Freymuller, C.F. Larsen, 2013, Active tectonics of the St. Elias orogen, Alaska, observed with GPS measurements. J. Geophys. Res., (2013).

Elmore, C.R., S.P.S. Gulick, B. Willems, R. Powell, Seismic stratigraphic evidence for glacial expanse during glacial maxima in the Yakutat Bay Region, Gulf of Alaska, Geochem. Geophys. Geosyst., 13, 1294-1311, (2013).

Elverhøi, A., R.L. Hooke, A. Solheim, Late Cenezoic erosion and sediment yield from the Svalbard-Barents Sea region: Implications for understanding erosion of glacierized basins, Quat. Sci. Rev., 17, 209-241, (1998).

Enkelmann, E., J.I. Garver, T.L. Pavlis, Rapid exhumation of ice-covered rocks of the Chugach-St. Elias orogen, Southeast Alaska, Geology, 36, 915-918, doi: 10.1130/G2252A.1, (2008).

Enkelmann, E., P.K. Zeitler, T.L. Pavlis, J.I. Garver, K.D. Ridgway, Intense localized rock uplift and erosion in the St Elias orogen of Alaska, Nature Geosci., 2, 360-363, doi: 10.1038/ngeo502, (2009).

Enkelmann, E., P.K. Zeitler, J.I. Garver, T.L. Pavlis, B.P. Hooks, The Thermochronological Record of Tectonic and Surface Process Interaction at the Yakutat-North American Collision Zone in Southeast Alaska, Am. J. Sci., 310, 231-260, doi: 102475/04.2010.01, (2010).

Enkelmann E., T.A. Ehlers, P.K. Zeitler, B. Hallet, Denudation of the Namche Barwa antiform, eastern Himalaya, Earth Planet. Sci. Lett., 307, 323-333, (2011).

Enkelmann, E., P.G.Valla, J.-D Champagnac, Low-temperature thermochronology of the Yakutat Plate corner, St. Elias Range (Alaska): bridging short-term and long-term deformation. Quaternary Sci. Rev., (2014).

Enkelmann, E., P.O. Koons, T.L. Pavlis, B. Hallet, A. Barker, J. Elliott, J.I. Garver, S.P.S. Gulick, R.M. Headley, G.L. Pavlis, K.D. Ridgway, N. Ruppert, H.J.A. Van Avendonk, Cooperation among tectonic and surface processes in the St. Elias Range, Earth's highest coastal mountains, Geophys. Res. Lett., 42(14), 5838-5846, doi: 10.1002/2015GL064727, (2015).

Enkelmann, E, A. Piestrzeniewicz, S. Falkowski, K. Stübner, T.A., Ehlers, thermochronology in southeast Alaska and southwest Yukon: Implications for North American Plate response to terrane accretion, Earth Planet. Sci. Lett., 457, 348-358, (2017).

Falkowski, S., E. Enkelmann, T.A. Ehlers, Constraining the area of rapid and deep-seated exhumation at the Yakutat plate corner, southeast Alaska, Tectonics, DOI: 10.1002/2013TC003408, (2014).

Fastook, J.L. and M. Prentice, A finite-element model of Antarctica: Sensitivity test for meteorological mass balance relationship, J. Glaciol., 40(134), 167-175, (1994).

Fastook, J.L., J.W. Head, D.R. Marchant, F. Forget, Tropical mountain glaciers on Mars: Altitude-dependence of ice accumulation, accumulation conditions, formation times, glacier dynamics, and implications for planetary spin-axis/orbital history, Icarus, 198(2), 305-317, (2008).

Fernandez, R.A., J.B. Anderson, J.S. Wellner, B. Hallet, Timescale dependence of glacial erosion rates: A case study of Marinelli Glacier, Cordillera Darwin, southern Patagonia, J. Geophys. Res., 116, (2011).

Fernandez, R.A., J.B. Anderson, J.S. Wellner, R.L. Minzoni, B. Hallet, R.T. Smith, Latitudinal variation in glacial erosion rates from Patagonia and the Antarctic Peninsula (46°S-65°S), Geol. Soc. Am. Bull., doi:10.1130/B31321.1, (2016).

Finkel, R.C., L.A. Owen, P.L. Barnard, M.W. Caffee, Beryllium-10 dating of Mount Everest moraines indicates a strong monsoon influence and glacial synchroneity throughout the Himalaya, Geology, 31, 561-564, (2003).

Finlayson, D.P., D.R. Montgomery, B. Hallet, Spatial coincidence of rapid inferred erosion with young metamorphic massifs in the Himalayas, Geology, 30(3), 219-222, doi: 10.1130/0091-7613(2002)030<0219:SCORIE>2.0.CO;2, (2002).

Finnegan, N.J., B. Hallet, D.R. Montgomery, P.K. Zeitler, J.O. Stone, A.M. Anders, L. Yuping, Coupling of rock uplift and river incision in the Namche Barwa-Gyala Peri massif, Tibet, Geol. Soc. Am. Bull., 120, 142-155, (2008).

Finnegan N.J., R. Schumer, S. Finnegan, A signature of transience in bedrock river incision rates over timescales of 104-107 years, Nature, 505, 391-394, (2014).

Fowler, A.C. and D.A. Larson, On the Flow of Polythermal Glaciers. I. Model and Preliminary Analysis, P. Roy. Soc. Lond. A. Mat., 363(1713), 217-242, doi: 10.1098/rspa.1978.0165, (1978).

Fricker, H.A., R.C. Warner, I. Allison, Mass balance of the Lambert Glacier Amery Ice Shelf system, East Antarctica: a comparison of computed balance fluxes and measured fluxes, J. Glaciol., 46, 561-570, (2000).

Fushimi, H., Glaciations in the Khumbu Himal (2); Glaciological Expedition of Nepal, Contribution No. 57, Seppyo, 40, 71-77, (1978).

Fushimi, H., M. Yoshida, O. Watanabe, B.P. Upadhyay, Distributions and grain sizes of surface debris in the Khumbu Glacier, Khumbu Region, East Nepal, Seppyo, 41(Special), 18-25, (1980).

Gabet, E.J., D.W. Burbank, B. Pratt-Sitaula, J. Putkonen, B. Bookhagen, Modern erosion rates in the High Himalayas of Nepal, Earth Planet. Sci. Lett., 267, 482-494, (2008).

Gades, A., H. Conway, N. Nereson, N. Naito, T. Kadota, Radio echo-sounding through supraglacial debris on Lirung and Khumbu Glaciers, Nepal Himalaya, in: Debris-covered Glaciers, IAHS Publ., (2000).

Gallagher, K., R. Brown, C. Johnson, Fission Track Analysis and its Applications to Geological Problems, Annu. Rev. Earth Planet. Sci., 26(1), 519-572, doi: 10.1146/annurev.earth.26.1.519, (1998).

Ganti, V., C. von Hagke, D. Scherler, M.P. Lamb, W.W. Fischer, J.-P. Avouac, Time scale bias in erosion rates of glaciated landscapes, Sci. Adv., 2, e1600205, (2016).

Gardelle, J., E. Berthier, Y. Arnaud, A. Kääb, Region-wide glacier mass balances over the Pamir-Karakoram-Himalaya during 1999–2011, The Cryosphere, 7(4), 1263-1286, doi: 10.5194/tc-7-1263-2013, (2013).

Gardner, J.S. and N.K. Jones, Sediment transport and yield at the Raikot Glacier, Nanga Parbat, Punjab Himalaya. In: J. F. Shroder Jr. (Ed.), Himalaya to the Sea. Routledge, London, pp. 184–197, (1993).

Garzanti, E. G. Vezzoli, S. Andò, J. Lavé, M. Attal, C. France-Lanord, P. DeCelles, Quantifying sand provenance and erosion (Marsyandi River, Nepal Himalaya), Earth Planet. Sci. Lett., 258, 500-515, (2007).

Gébelin, A., A. Mulch, C. Teyssier, M.J. Jessup, R.D. Law, M. Brunel, The Miocene elevation of Mount Everest, Geology, 41, 799-802, (2013).

Glen, J.W. and W.V. Lewis, Measurements of side-slip at Austerdalsbreen, 1959, J. Glaciol., 3(30), 1109-1122, (1961).

Godard, V., D.W. Burbank, D.L. Bourlès, B. Bookhagen, R. Braucher, G.B. Fisher, Impact of glacial erosion on 10Be concentrations in fluvial sediments of the Marsyandi catchment, central Nepal, J. Geophys. Res., 117, (2012).

Grabowski, D., E. Enkelmann, T.A. Ehlers, Evaluation of the spatial extend of rapid exhumation in the St. Elias syntaxis region, SE Alaska, J. Geophys. Res., 118, 1-18. doi:10.1002/jgrf.20136, (2013).

Gulick, S.P.S., J.M. Jaeger, A.C. Mix, H. Asahi, H. Bahlburg, C.L. Belanger, G.B.B. Berbel, L. Childress, E. Cowan, L. Drab, M. Forwick, A. Fukumura, S. Ge, S. Gupta, A. Kioka, S. Konno, L.J. LeVay, C. März, K.M. Matsuzaki, E.L. McClymont, C. Moy, J. Müller, A. Nakamura, T. Ojima, F.R. Ribeiro, K.D. Ridgway, O.E. Romero, A.L. Slagle, J.S. Stoner, G. St-Onge, I. Suto, M.D. Walczak, L.L. Worthington, I. Bailey, E. Enkelmann, R. Reece, and J.M. Swartz, Mid-Pleistocene climate transition drives net mass loss from rapidly uplifting St. Elias Mountains, Alaska, P. Natl. Acad. Sci. USA, 112(49), 15042-15047, doi: 10.1073/pnas.1512549112, (2015).

Gulley, J.D., D. I. Benn, D. Müller, A. Luckman, A cut-and-closure origin for englacial conduits in uncrevassed regions of polythermal glaciers, J. Glaciol., 55, 66-80, (2009).

Gustavson, T.C. and J.C. Boothroyd, A depositional model for outwash, sediment sources, and hydrologic characteristics, Malaspina Glacier, Alaska: a modern analog of the southeastern margin of the Laurentide Ice Sheet, Geol. Soc. Am. Bull., 99, 187-200, (1987).

Haeberli, W., J.-C. Alean, P. Müller, M. Funk, Assessing risks from glacier hazards in high mountain regions: some experiences in the Swiss Alps, Annals Glaciol., 13, 96-102, (1988).

Hallet, B., A theoretical model of glacial abrasion, J. Glaciol., 23(89), 29-50, (1979).

Hallet, B., Glacial abrasion and sliding: their dependence on the debris concentration in basal ice, Ann. Glaciol., 2(1), 29-33, (1981).

Hallet, B., Glacial Quarrying: A Simple Theoretical Model, J. Glaciol., 22(1), 1-8, (1996).

Hallet, B., Glacial erosion assessment, Tech. Rep., OPG's Deep Geologic Repository for Low and Intermediate Level Waste, (2011).

Hallet, B., L. Hunter, J. Bogen, Rates of erosion and sediment evacuation by glaciers: A review of field data and their implications, Global Planet. Change, 12, 213-235, (1996).

Hambrey, M.J., D.J. Quincey, N.F. Glasser, J. M. Reynolds, S. J. Richardson, S. Clemmens, Sedimentological, geomorphological and dynamic context of debris-mantled glaciers, Mount Everest (Sagarmatha) region, Nepal, Quaternary Sci. Rev., 27, 2361-2389, (2008).

Harbor, J.M., Numerical modeling of the development of U-shaped valleys by glacial erosion, Geol. Soc. Am. Bull., 104(1), 1364-1375, (1992).

Harper, J.T. and N.F. Humphrey, High altitude Himalayan climate inferred from glacial ice flux, Geophys. Res. Lett., 30(14), doi: 10.1029/2003GL017329, (2003).

Headley, R., B. Hallet, G. Roe, E.D. Waddington, E. Rignot, Spatial distribution of glacial erosion rates in the St. Elias range, Alaska, inferred from a realistic model of glacier dynamics, J. Geophys. Res., F03027, doi:10.1029/2011JF002291, (2012).

Heimsath, A.M. and R. McGlynn, Quantifying periglacial erosion in the Nepal high Himalaya, Geomorphology, 97, 5-23, (2008).

Herman, F. and J. Braun, Evolution of the glacial landscape of the Southern Alps of New Zealand: Insights from a glacial erosion model, J. Geophys. Res., 113, (2008).

Herman, F., D. Seward, P. G. Valla, A. Carter, B. Kohn, S. D. Willett, T. A. Ehlers, Worldwide acceleration of mountain erosion under a cooling climate, Nature, 504, 423–426, (2013).

Herman, F., O. Beyssac, M. Brughelli, S.N. Lane, S. Leprince, T. Adatte, J. Lin, J.-P. Avouac, S.C. Cox, Erosion by an alpine glacier, Science, (2015).

Herman, F. and J. Champagnac, Plio-Pleistocene increase of erosion rates in mountain belts in response to climate change, Terra Nova, 28, 2-10, (2016).

Hodges, K.V., Tectonics of the Himalaya and southern Tibet from two perspectives, Geol. Soc. Am. Bull., 112, 324–350, (2000).

Hodges, K.V., C. Wobus, K. Ruhl, T. Schildgen, K. Whipple, Quaternary deformation, river steepening, and heavy precipitation at the front of the Higher Himalayan ranges, Earth Planet. Sci. Lett., 220, 379-389, (2004).

Hooke, R.LeB. and J. Fastook, Thermal conditions at the bed of the Laurentide ice sheet in Maine during deglaciation: implications for esker formation, J. Glaciol., 53(183), 646-658, (2007).

Hren, M.T., C.P. Chamberlain, G.E. Hilley, P.M. Blisniuk, B. Bookhagen, Major ion chemistry of the Yarlung Tsangpo–Brahmaputra river: Chemical weathering, erosion, and CO2 consumption in the southern Tibetan plateau and eastern syntaxis of the Himalaya, Geochim. Cosmochim. Acta, 71, 2907-2935, (2007).

Humphrey, N.F. and C.F. Raymond, Hydrology erosion and sediment production in a surging glacier, Variegated Glacier, Alaska, 1982-83, J. Glaciol., 40(136), 539-552, (1994).

Huntington K.W., A.E. Blythe, K.V. Hodges, Climate change and Late Pliocene acceleration of erosion in the Himalaya, Earth Planet. Sci. Lett., 252, 107-118, (2006).

Hutter, K., The Effect of Longitudinal Strain on the Shear Stress of an Ice Sheet: In Defence of Using Stretched Coordinates, J. Glaciol., 27(95), 39-56, (1981).

Immerzeel, W.W., L.P.H. van Beek, M.F.P. Bierkens, Climate Change Will Affect the Asian Water Towers, Science, 328(5984), 1382-1385, doi: 10.1126/science.1183188, (2010).

Inoue, J., Mass budget of Khumbu Glacier, Seppyo, 32, 15-19, (1977).

Inoue, J. and M. Yoshida, Ablation and Heat Exchange over the Khumbu Glacier; Glaciological Expedition of Nepal, Seppyo, 41, 26-33, (1980).

Iverson, N.R., Potential effects of subglacial water-pressure fluctuations on quarrying, J. Glaciol., 37, 27-36, (1991).

Iverson, N.R., A theory of glacial quarrying for landscape evolution models, Geology, 40(8), 679-682, (2012).

Iverson, N.R. and L.K. Zoet, Experiments on the dynamics and sedimentary products of glacier slip, Geomorphology, 244, 121-134, (2015).

Iwata, S., Late Pleistocene and Holocene Moraines in the Sagarmatha (Everest) Region, Khumbu Himal; Glaciological Expedition to Nepal, Contribution No. 23, Seppyo, 38, 109-114, (1976).

Jaeger, J.M., C.A Nittrouer, N.D. Scott, and J.D. Milliman, Sediment accumulation along a glacially impacted mountainous coastline: north-east Gulf of Alaska, Basin Res., 10, 155–173, (1998).

Johnson, J.V., A basal water model for ice sheets, Thesis (Ph.D.), University of Maine, (2002).

Joughin, I., D.R. MacAyeal, S. Tulaczyk, Basal shear stress of the Ross ice streams from control method inversions, J. Geophys. Res., 109, B09405, (2004).

Juen, M., C. Mayer, A. Lambrecht, H. Han, S. Liu, Impact of varying debris cover thickness on ablation: a case study for Koxkar Glacier in the Tien Shan, The Cryosphere, 8(2), 377-386, doi: 10.5194/tc-8-377-2014, (2014).

Kääb, A., E. Berthier, C. Nuth, J. Gardelle, Y. Arnaud, (2012), Contrasting patterns of early twenty-first-century glacier mass change in the Himalayas, Nature., 488(7412), 495-498, (2012).

Kaspari, S., P. Mayewski, S. Kang. S. Sneed, S. Hou, R. Hooke, K. Kreutz, D. Introne, M. Handley, K. Maasch, D. Qin, J. Ren, Reduction in northward incursions of the South Asian monsoon since ~1400 AD inferred from a Mt. Everest ice core, Geophys. Res. Lett., 34, (2007).

Kayastha, R.B., Y. Takeuchi, M. Nakawo, Y. Ageta, Practical prediction of ice melting beneath various thickness of debris cover on Khumbu Glacier, Nepal, using a positive degree-day factor, in: Debris-covered Glaciers, IAHS Publ., (2000).

Kayastha, R. B. and S. P. Harrison, Changes of the equilibrium-line altitude since the Little Ice Age in the Nepalese Himalaya, Ann. Glaciol.,, 48, 93-99, (2008).

Kessler, M.A., R.S. Anderson, J.P. Briner, Fjord insertion into continental margins driven by topographic steering of ice, Nature Geosci., 1, 365-369, (2008).

Kirchner, J.W., R. C. Finkel, C. S. Riebe, D. E. Granger, J. L. Clayton, J. G. King, W. F. Megahan, Mountain erosion over 10 yr, 10 k.y., and 10 m.y. time scales, Geology, 29, 591-594, (2001).

Konrad, S.K. and N.F. Humphrey (2000), Steady-state flow model of debris-covered glaciers (rock glaciers), in: Debris-covered Glaciers, IAHS Publ., (2000).

Koppes, M.N. and B. Hallet, Influence of rapid glacial retreat on the rate of erosion by tidewater glaciers, Geology, 30, 47-50, (2002).

Koppes, M. and B. Hallet, Erosion rates during rapid deglaciation in Icy Bay, Alaska, J. Geophys. Res., 111, (2006).

Koppes, M.N., B. Hallet, E. Rignot, J. Mouginot, J. Smith-Wellner, K. Boldt, Observed latitudinal variations in glacial erosion as a function of ice dynamics, Nature, (2015).

Koons, P.O., P.K. Zeitler, C.P. Chamberlain, D. Craw, A.S. Meltzer, Mechanical links between erosion and metamorphism in Nanga Parbat, Pakistan Himalaya, Am. J. Sci., 302(9), 749-773, (2002).

Koons, P.O., B.P. Hooks, T.L. Pavlis, P. Upton, A.D. Barker, Three-dimensional mechanics of Yakutat convergence in the southern Alaskan plate corner, Tectonics, 29, TC4008, doi: 10.1029/2009TC002463, (2010).

Koons, P.O., P. Upton, A.D. Barker, The influence of mechanical properties on the link between tectonic and topographic evolution, Geomorphology, 137, 168-180, (2012).

Koons, P.O., P.K. Zeitler, B. Hallet, Tectonic aneurysms and mountain building, In: Shroder, J. (Editor in Chief), Owen, L.A. (Ed.), Treatise on Geomorphology, Academic Press, San Diego, vol 5, 318-349, (2013).

Kuhle, M., Glacial geomorphology and ice ages in Tibet and the surrounding mountains, Isl. Arc, 14(4), 346-367, doi: 10.1111/j.1440-1738.2005.00501.x, (2005).

Lang, K.A., K.W. Huntington, D.R. Montgomery, Erosion of the Tsangpo Gorge by megafloods, Eastern Himalaya, Geology, 41, 1003-1006, (2013).

Larsen, I.J. and D.R. Montgomery, Landslide erosion coupled to tectonics and river incision, Nature Geosci., 5, 468-473, (2012)

Love, K.B., B. Hallet, T.L. Pratt, S. O'Neel, Observations and modeling of fjord sedimentation during the 30 year retreat of Columbia Glacier, AK, J. Glaciol., 62(234), 778-793, (2016).

Luckman, A., D.J. Quincey, S. Bevan, The potential of satellite radar interferometry and feature tracking for monitoring flow rates of Himalayan glaciers. Remote Sens. Environ., 111, 172–181, (2007).

Lundstrom, S.C., The budget and effect of superglacial debris on Eliot Glacier, Mount Hood, Oregon, Ph.D. thesis, University of Colorado, Boulder, (1992).

MacGregor, K.R., R.S. Anderson, S.P. Anderson, E.D. Waddington, Numerical simulations of glcial-valley longitudinal profile evolution, Geology, 28, 1031-1034, (2000).

Mancktelow, N.S. and B. Grasemann, Time-dependent effects of heat advection and topogrpahy on coolling histories during erosion, Tectonophysics, 270, 167-195, (1997).

Manley, W.F. and D.S. Kaufman, Alaska PaleoGlacier Atlas: Institute of Arctic and Alpine Research (INSTAAR), University of Colorado, v. 2, (2002).

Mann, D.H., A.L. Crowell, T.D. Hamilton, B.P. Finney, Holocene geographic and climatic history around the Gulf of Alaska, Arctic Anthropol., 35, 112-131, (1998).

Meier, M.F. and A. Post, Fast tidewater glaciers, J. Geophys. Res., 92(B9), 9051-9058, (1987).

Melanson, A., T. Bell, L. Tarasov, Numerical modelling of subglacial erosion and sediment transport and its application to the North American ice sheets over the Last Glacial cycle, Quaternary Sci. Rev., 68, 154-174, doi:http://dx.doi.org/10.1016/j.quascirev.2013.02.017, (2013).

Merrand, Y., Glacier erosion at convergent margins: a numerical and field study in the Chugach-St. Elias Mountains of South Alaska, Thesis (Ph.D.), University of Washington, (2013).

Mesinger, F., G. DiMego, E. Kalnay, K. Mitchell, et al., North American regional reanalysis, Bull. Am. Meteo. Soc., 278, 343-360, (2006)

Mey, J., D. Scherler, G. Zeilinger, M. R. Strecker, Estimating the fill thickness and bedrock topography in intermontane valleys using artificial neural networks, J. Geophys. Res., 120, 1301-1320, (2015).

Mihalcea, C., C. Mayer, G. Diolaiuti, C. D'agata, C. Smiraglia, A. Lambrecht, E. Vuillermoz, G. Tartari, Spatial distribution of debris thickness and melting from remote-sensing and meteorological data, at debris-covered Baltoro glacier, Karakoram, Pakistan, Ann. Glaciol., 48(1), 49-57, (2008).

Molnar, P., Late Cenezoic increase in accumulation rates of terrestrial sediment: How might climate change have affected erosion rates?, Annu. Rev. Earth Planet. Sci., 32,, 67-89, (2004).

Molnar, P. and P. England, Late Cenozoic uplift of mountain ranges and global climate change: chicken or egg?, Nature, 346, 29-34, (1990).

Molnar, P., R.S. Anderson, S.P. Anderson, Tectonics, fracturing of rock and erosion, J. Geophys. Res., 112, (2007).

Molnia, B.F. and A. Post, Surges of Bering Glacier, Geol. Soc. Am. Spec. Paper, 462, 291-316, (2010).

Motyka, R.J., W.P. Dryer, J. Amundson, M. Truffer, M. Fahnestock, Rapid submarine melting driven by subglacial discharge, LeConte Glacier Alaska, Geophys. Res. Lett., 40(19), 1-5, (2013).

Müller, F., Mittelfristige Schwankungen der Oberflachengeschwindingkeit des Khumbugletshers am Mount Everest. Scheweizerische Bauzeitung, Jahrg, 86, 569-574, (1968).

Naito, N., M. Nakawo, T. Kadota, C.F. Raymond, Numerical simulation of recent shrinkage of Khuinbu Glacier, Nepal Himalayas, in: Debris-covered Glaciers, IAHS Publ., (2000).

Nakawo, M. and G.J. Young, Field experiments to determine the effect of a debris layer on ablation of glacier ice, Ann. Glaciol., 2, 85-91, doi: 10.3189/172756481794352432, (1981).

Nakawo, M., S. Iwata, O. Watanabe, M. Yoshida, Processes which distribute surface debris on the Khumbu Glacier, Nepal Himalaya, 8, 129-131, Ann. Glaciol., (1986).

Nakawo, M., H. Yabuki, A. Sakai, Characteristics of Khumbu Glacier, Nepal Himalayas: recent changes in the debris covered area, Annals Glaciol., 28, 118–122, (1999).

Nicholson, L. and D.I. Benn, Calculating ice melt beneath a debris layer using meteorological data, J. Glaciol., 52(178), 463-470, (2006).

Nicholson, L. and D.I. Benn, Properties of natural surface debris in relation to modelling sub-debris ice ablation, Earth Surf. Proc. Land., 38, 490-501, (2013).

Nick, F.M., C.J. van der Veen, J. Oerlemans, Controls on advance of tidewater glaciers: results from numerical modeling applied to Columbia Glacier, J. Geophys. Res., 112, 1-11, (2007).

Østrem, G., Ice Melting under a Thin Layer of Moraine, and the Existence of Ice Cores in Moraine Ridges, Geogr. Ann., 41, 228– 230, (1959).

Owen, L.A. and D.I. Benn, Equilibrium-line altitudes of the Last Glacial Maximum for the Himalaya and Tibet: an assessment and evaluation of results, Quatern. Int., 138–139, 55-78, (2005).

Owen, L.A., R. Robinson, D.I. Benn, R.C. Finkel, N.K. Davis, C. Yi, J. Putkonen, D. Li, A.S. Murray, Quaternary glaciation of Mount Everest, Quaternary Sci. Rev., 28, 1412-1433, (2009).

Parrish, R.R., Cenozoic thermal evolution and tectonics of the Coast Mountains of British Columbia: 1. Fission track dating, apparent uplift rates, and patterns of uplift, Tectonics, 2, (1983).

Pavlis, T.L., J.B. Chapman, R.L. Bruhn, K. Ridgway, L.L. Worthington, S.P.S. Gulick, J. Spotila, Structure of the actively deforming fold-thrust belt of the St. Elias orogeny with implications for glacial exhumation and three-dimensional tectonic processes, Geosphere, 8, 991–1019, (2012).

Pavlis, T.L., E. Enkelmann, S.P.S. Gulick, G.L. Pavlis, Introduction: Neogene tectonics and climate-tectonic interactions in the southern Alaskan orogen themed issue, Geosphere, 10, 424-427, (2014).

Peizhen, Z., P. Molnar, W.R. Downs, Increased sedimentation rates and grain sizes 2-4 Myr ago due to the influence of climate change on erosion rates, Nature, 410, 891-897, (2001).

Péwé, T.L., Quaternary geology of Alaska, U.S. Geological Survey Professional Paper, 835, 145 pp., (1975).

Plafker, G., Regional geology and petroleum potential of the northern Gulf of Alaska continental margin, *in* Scholl, D.W., A. Grantz, and J.G. Vedder, eds., Geology and resource potential of the continental margin of western North America and adjacent ocean basins; Beaufort Sea to Baja

California: Circum-Pacific Council for Energy and Mineral Resources, Earth Science Series, Houston, 229-268, (1987).

Plafker, G., J.C. Moore, G.R. Winkler, Geology of the southern Alaskan margin, *in* Plafker, G. and H.C. Berg,, eds., The geology of Alaska: Geology of North America, vol. G-1: Geological Society of America, 389-449, (1994).

Pollard D. and R.M. Deconto, A coupled Ice-Sheet/Ice-Shelf/Sediment model applied to a marine-margin flowline: forced and unforced variations, M.J. Hambrey (Ed.), Glacial Sedimentary Processes and Products, Blackwell Publishing Ltd, pp. 37–52, (2009).

Pratt-Sitaula, B., D.W. Burbank, A. Heimsath, T. Ojha, Landscape disequilibrium on 1000–10,000 year scales Marsyandi River, Nepal, central Himalaya, Geomorphology, 58, 223-241, (2004).

Putnam, A.E., J.M. Schaefer, G.H. Denton, D.J. Barrell, S.D. Birkel, B.G. Andersen, M.R. Kaplan, R.C. Finkel, R. Schwartz, A.M. Doughty, The last local glacial maximum at 44°S documented by a 10BE moraine chronology at Lake Ohau, Southern Alps of New Zealand, J. Quat. Sci. Rev., 62, 114-141, (2013).

Quincey, D.J., A. Luckman, D. Benn, Quantification of Everest region glacier velocities between 1992 and 2002, using satellite radar interferometry and feature tracking, J. Glaciol., 55, 596-606, (2009).

Rahaman, W., S.K. Singh, R. Sinha, S.K. Tandon, Climate control on erosion distribution over the Himalaya during the past ~100 ka, Geology, 37, 559-562, (2009).

Rasmussen, L.A., H. Conway, R.M. Krimmel, R. Hock, Surface mass balance, thinning and iceberg production, Columbia Glacier, Alaska, 19482007, J. Glaciol., 57(203), 431-440, (2011).

Reece, R.S., S.P.S. Gulick, B.K. Horton, G.L. Christeson, L.L. Worthington, Tectonic and climatic influence on the evolution of the Surveyor Fan and Channel system, Gulf of Alaska, Geosphere, 7, 830-844, (2011).

Reynolds, J.M., Dielectric behaviour of firn and ice from the Antarctic Peninsula, Antarctica, J. Glaciol., 31, 253-262, (1985).

Reznichenko, N., T. Davies, J. Shulmeister, M. McSaveney, Effects of debris on ice-surface melting rates: an experimental study, J. Glaciol., 56(197), 384-394, (2010).

Richards, B., D.I. Benn, L.A. Owen, E.J. Rhodes, J.Q. Spencer, Timing of late Quaternary glaciations south of Mount Everest in the Khumbu Himal, Nepal, Geol. Soc. Am. Bull., 112, 1621-1632, (2000).

Richardson, S.D. and J.M. Reynolds, An overview of glacial hazards in the Himalayas, Quaternary International., 65–66, 31-47, (2000).

Rignot, E., J. Mouginot, C.F. Larsen, Y. Gim, D. Kirchner, Low-frequency radar sounding of temperate ice masses in Southern Alaska, Geophys. Res. Lett., 40(20), 5399-5405, doi: 10.1002/2013GL057452, (2013).

Rignot, E., I. Fenty, Y. Xu, C. Cai, I. Velicogna, C. Ó Cofaigh, J.A. Dowdeswell, W. Weinrebe, G. Catania, D. Duncan, Bathymetry data reveal glaciers vulnerable to ice-ocean interaction in Uummannaq and Vaigat glacial fjords, west Greenland, Geophys. Res. Lett., 43(6), 2667-2674, (2016).

Röthlisberger, H. and A. Iken, Plucking as an effect of water-pressure variations at the glacier bed, Ann. Glaciol., 2, 57-62, (1981).

Rounce, D.R. and D.C. McKinney, Debris thickness of glaciers in the Everest area (Nepal Himalaya) derived from satellite imagery using a nonlinear energy balance model, The Cryosphere., 8(4), 1317-1329, doi: 10.5194/tc-8-1317-2014, (2014).

Rowan, A.V., D.L. Egholm, D.J. Quincey, N.F. Glasser, Modelling the feedbacks between mass balance, ice flow and debris transport to predict the response to climate change of debris-covered glaciers in the Himalaya, Earth Planet. Sc. Lett., 430, 427-438, (2015).

Sadler, P.M., Sediment accumulation rates and the completeness of stratigraphic sections, J. Geol., 89, 569–584, (1981).

Sadler, P.M. and D.J. Jerolmack, Scaling laws for aggradation, denudation and progradation rates: the case for time-scale invariance at sediment sources and sinks, Geol. Soc. London Spec. Publ., 404, 69-88, (2014).

Sakai, A., N. Takeuchi, K. Fujita, M. Nakawo, Role of surface ponds in the ablation process of a debris-covered glacier in the Nepal Himalayas, in: Debris-covered Glaciers, IAHS Publ., (2000).

Sakai, H., M. Sawada, Y. Takigami, Y. Orihashi, T. Danhara, H. Iwano, Y. Kuwahara, Q. Dong, H. Cai, J. Li, Geology of the summit limestone of mount Qomolangma (Everest) and cooling history of the yellow band under the Qomolangma detachment, Isl. Arc, 14, 297–310, (2005).

Salerno, F., E. Buraschi, G. Bruccoleri, G. Tartari, C. Smiraglia, Glacier surface-area changes in Sagarmatha national park, Nepal, in the second half of the 20th century, by comparison of historical maps, J. Glaciol., 54(187), 738-752, (2008).

Schaefer, J.M., A.E. Putnam, G.H. Denton, M.R. Kaplan, S.D. Birkel, A.M. Doughty, S. Kelley, D.J. Barrell, R.C. Finkel, G. Winckler, R.F. Anderson, U.S. Ninneman, S. Barker, R. Schwartz, B.G. Andersen, C. Schluechter, The Southern Glacial Maximum 65,000 years ago and its Unfinished Termination. Quaternary Sci. Rev., 114, p. 52-60, (2015).

Scheaf, M.A., L. Serpa, T.L. Pavlis, Exhumation rates in the St. Elias Mountains, Alaska. Tectonophysics, 367, 1-11, (2003).

Scherler, D., Climatic limits to headwall retreat in the Khumbu Himalaya, eastern Nepal, Geology, 42, 1019-1022, (2014).

Scherler, D., S. Leprince, M.R. Strecker, Glacier-surface velocities in alpine terrain from optical satellite imagery—Accuracy improvement and quality assessment, Remote Sens. Environ., 112(10), 3806-3819, (2008).

Scherler, D., B. Bookhagen, M.R. Strecker, Hillslope-glacier coupling: The interplay of topography and glacial dynamics in High Asia, J. Geophys. Res., 116(F2), doi: 10.1029/2010JF001751, (2011).

Scherler, D., B. Bookhagen, M.R. Strecker, Spatially variable response of Himalayan glaciers to climate change affected by debris cover, Nature Geosci., 4, 156-159, (2011).

Schrott, L., G. Hufschmidt, M. Hankammer, T. Hoffmann, R. Dikau, Spatial distribution of sediment storage types and quantification of valley fill deposits in an alpine basin Reintal, Bavarian Alps Germany, Geomorphology, 55, 45–63, (2003).

Searle, M.P., R. L. Simpson, R. D. Law, R. R. Parrish, D. J. Waters, The structural geometry, metamorphic and magmatic evolution of the Everest massif, high Himalaya of Nepal–south Tibet, J. Geol. Soc., 160, 345–366, (2003).

Searle, M.P., R. D. Law, M.J. Jessup, Crustal structure, restoration and evolution of the Greater Himalaya in Nepal–south Tibet: Implications for channel flow and ductile extrusion of the middle crust, Geol. Soc. Spec. Publ., 268, 355–378, (2006).

Seguinot, J., I. Rogozhina, A.P. Stroeven, M. Margold, J. Kleman, Numerical simulations of the Cordilleran ice sheet through the last glacial cycle, The Cryosphere, 9, 4147-4203, (2015).

Seong, Y.B., L.A. Owen, M. W. Caffee, U. Kamp, M.P. Bishop, A. Bush, L. Copland, J.F. Shroder, Rates of basin-wide rockwall retreat in the K2 region of the Central Karakoram defined by terrestrial cosmogenic nuclide 10Be, Geomorphology, 107, 254-262, (2009).

Shackleton, N.J., M.A. Hall, F. Vincent, E., Phase relationships between millennial-scale events 64,000-24,000 years ago, Paleoceanography 15, 565-569, (2000).

Shea, J., W. Immerzeel, P. Wagnon, C. Vincent, S. Bajracharya, Modelling glacier change in the Everest region, Nepal Himalaya, The Cryosphere, 9(3), 1105-1128, (2015).

Shuster, D.L., Rapid Glacial Erosion at 1.8 Ma Revealed by 4He/3He Thermochronometry, Science, 310, 1668–1670, (2005).

Siegert, M.J., N. Ross, J. Li, D.M. Schroeder, D. Rippin, D. Ashmore, R. Bingham, P. Gogineni, Subglacial controls on the flow of Institute Ice Stream, West Antarctica, Ann. Glaciol., (2016).

Simpson, R.L., R. R. Parrish, M. P. Searle, D. J. Waters, Two episodes of monazite crystallization during metamorphism and crustal melting in the Everest region of the Nepalese Himalaya, Geology, 28,403–406, (2000).

Smith, A.M., T.A. Jordan, F. Ferraccioli, R.G. Bingham, Influence of subglacial conditions on ice stream dynamics: Seismic and potential field data from Pine Island Glacier, West Antarctica, J. Geophys. Res.-Sol. Ea., 118, 1471-1482, (2013).

Spotila, J.A. and A.L. Berger, Exhumation at orogenic indentor corner under long-term glacial conditions: Example of the St Elias orogen, southern Alaska, Tectonophysics, 490, 241–256, doi: 10.1016/j.tecto.2010.05.015, (2010).

Stewart, R.J., B. Hallet, P. K. Zeitler, M. A. Malloy, C. M. Allen, D. Trippett, Brahmaputra sediment flux dominated by highly localized rapid erosion from the easternmost Himalaya, Geology, 36, 711-714, (2008).

Straneo, F., G. Hamilton, D.A. Sutherland, L.A. Stearns, F. Davidson, M.O. Hammil, G.B. Stenson, A. Rosing-Asvid, Rapid circulation of warm subtropical waters in a major glacial fjord in East Greenland, Nat. Geosci., 3, 1–5, doi:10.1038/ngeo764, (2010).

Straneo, F., R.G. Curry, D.A. Sutherland, G.S. Hamilton, C. Cenedese, K. Våge, L.A. Stearns, Impact of fjord dynamics and glacial runoff on the circulation near Helheim Glacier, Nat. Geosci., 4, 322-327, doi:10.1038/ngeo1109, (2011).

Streule, M.P. Searle, D.J. Waters, M.S.A. Horstwood, Metamorphism, melting, and channel flow in the greater Himalayan sequence and Makalu leucogranite: Constraints from thermobarometry, metamorphic modeling, and U-Pb geochronology, Tectonics, 29, (2010).

Streule, M.J., A. Carter, M.P. Searle, J.M. Cottle, Constraints on brittle field exhumation of the Everest-Makulu section of the Greater Himalayan Sequence: Implications for models of crustal flow, Tectonics, 31, (2012).

Stüwe, K., L. White, R. Brown, The influence of eroding topography on steady-state isotherms. Application to fission track analysis, Earth Planet. Sci. Lett., 124(1), 63-74, doi: http://dx.doi.org/10.1016/0012-821X(94)00068-9, (1994).

Tartari, G., G.P. Verza, L. Bertolani, Meteorological data at the Pyramid Laboratory Observatory. Khumbu Valley, Sagarmatha National Park, Nepal. In: A. Lami & G. Giussani (Eds), Limnology of high altitude lakes in the Mt Everest Region (Nepal). Mem. Ist. ital. Idrobiol., 57: 23-40, (1998).

Thiede, R.C, B. Bookhagen, J.R. Arrowsmith, E.R. Sobel, M.R. Strecker, Climatic control on rapid exhumation along the Southern Himalayan Front, Earth Planet. Sci. Lett., 222, 791-806, (2004).

Thiede, R.C and T.A. Ehlers, Large spatial and temporal variations in Himalayan denudation, Earth Planet. Sci. Lett., 371-372, 278-293, (2013).

Thompson, S.S., D.I. Benn, K. Dennis, A. Luckman, A rapidly growing moraine-dammed glacial lake on Ngozumpa Glacier, Nepal, Geomorphology, 145–146, 1-11, (2012).

Thomson, S.N., M. T. Brandon, J. H. Tomkin, P. W. Reiners, C. Vásquez, N. J. Wilson, Glaciation as a destructive and constructive control on mountain building, Nature, 467, 313–317, (2010).

Tomkin, J.H., Coupling glacial erosion and tectonics at active orogens: A numerical modeling study, J. Geophys. Res., 112, (2007).

Tomkin, J.H., Numerically simulating alpine landscapes: the geomorphic consequences of incorporating glacial erosion in surface process models, Geomorphology, 103, 180-188, (2009).

Trusel, L.D., B.A. Willems, R.D. Powell, L.A. Mayer, Quantification of glaciomarine sediment yields using multibeam sonar in Alaskan fjords, Eos Trans. AGU, 89(53), Fall Meet. Suppl., Abstract C11B-0508, (2008).

Tulaczyk, S., W.B. Kamb, H.F. Engelhardt, Basal mechanics of Ice Stream B, west Antarctica: 1. Till mechanics, J. Geophys. Res.-Sol. Ea., 105, 463-481, (2000).

Valla, P.G., D.L. Shuster, P.A. van der Beek, Significant increase in relief of the European Alps during mid-Pleistocene glaciations, Nature Geosci., 4, 588-692, (2011).

Vannay, J-C., B. Grasemann, M. Rahn, W. Frank, A. Carter, V. Baudraz, M. Cosca, Miocene to Holocene exhumation of metamorphic crustal wedges in the NW Himalaya: Evidence for tectonic extrusion coupled to fluvial erosion, Tectonics, 23, TC1014, (2004).

Vincent, C., P. Wagnon, J.M. Shea, W.W. Immerzel, P.D.A. Kraaijenbrink, D. Shrestha, A. Soruco, Y. Arnaud, F. Brun, E. Berthier, S.F. Sherpa, Reduced melt on debris-covered glaciers: investigation from Changri Nup Glacier, Nepal, The Cryosphere Discuss., doi:10.5194/tc-2016-75, in review, (2016).

Wang, T., A. Hamann, D.L. Spittlehouse, S.N. Aitken, Development of scale-free climate data for Western Canada for use in resource management, Int. J. Climatol., 26, 383-397, (2006).

Weertman, J., The theory of glacier sliding, J. Glaciol., 5, 287-303, (1964).

Westoby, M.J., N.F. Glasser, J. Brasington, M.J. Hambrey, D.J. Quincey, J.M. Reynolds, Modelling outburst floods from moraine-dammed glacial lakes, Earth-Sci. Rev., 134, 137-159, (2014).

Whipple, K.X., The influence of climate on the tectonic evolution of mountain belts, Nature Geosci., doi:10.1038/NGEO4713, (2009).

Willenbring, J.K. and D.J. Jerolmack, The null hypothesis: globally steady rates of erosion, weathering fluxes and shelf sediment accumulation during Late Cenozoic mountain uplift and glaciation, Terra Nova, 28, 11-18, (2016).

Williams, V.S., Present and former equilibrium-line altitudes near Mount Everest, Nepal and Tibet, Arctic Alpine Res., 15, 201-211, (1983).

Wobus, C.W., K.V. Hodges, K.X. Whipple, Has focused denudation sustained active thrusting at the Himalayan topographic front?, Geology, 31(10), 861-864, (2003).

World Glacier Monitoring Service (WGMS), Fluctuations of glaciers 1995–2000 (Vol. VIII), ed. Haeberli, W., M. Zemp, R. Frauenfelder, M. Hoelzle, A. Kääb. IAHS/UNEP/UNESCO, World Glacier Monitoring Service, Zürich, (2005).

Worthington, L.L., S.P.S. Gulick, T.L. Pavlis, Coupled stratigraphic and structural evolution of a glaciated orogenic wedge, offshore St. Elias orogen, Alaska, Tectonics, 29, (2010).

Yanites, B.J. and T.A. Ehlers, Global climate and tectonic controls on the denudation of glaciated mountains, Earth Planet. Sci. Lett., 325-326, 63-75, (2012).

Yanites, B.J. and T.A. Ehlers, Intermittent glacial sliding velocities explain variations in long-timescale denudation, Earth Planet. Sci. Lett., 450, 52-61, (2016).

Yokoyama, Y., K. Lambeck, P. De Deckker, P. Johnston, and L.K. Fifield, Timing of the Last Glacial Maximum from observed sea-level minima, Nature, 406, 713-716, (2000).

Zeitler, P.K., Cooling history of the NW Himalaya, Pakistan, Tectonics, 4, 127-151, (1985).

Zeitler, P.K., P.O. Koons, M.P. Bishop, C.P. Chamberlain, D. Craw, M.A. Edwards, S. Hamidullah, M. Qasim Jan, M. Asif Khan, M. Umar Khan Khattak, W.S.F. Kidd, R.L. Mackie, A.S. Meltzer, S.K. Park, A. Pecher, M.A. Poage, G. Sarker, D.A. Schneider, L. Seeber, J.F. Shroder, Crustal reworking at Nanga Parbat, Pakistan: Metamorphic consequences of thermal-mechanical coupling facilitated by erosion, Tectonics, 20(5), 712-728, (2001).

Zeitler, P.K., A.S. Meltzer, L. Brown, W.S.F. Kidd, C. Lim, E. Enkelmann, Tectonics and topographic evolution of Namche Barwa and the easternmost Lhasa block, Tibet, Geol. Soc. Am. Spec. Paper, 507, (2014).

Zhang, J., U.S. Bhatt, W.V. Tangborn, C.S. Lingle, Response of glaciers in northwestern North America to future climate change: an atmosphere/glacier hierarchical modeling approach, Ann. Glaciol., 46, 283-290, (2007).

Zhang, Y., K. Fujita, S. Liu, Q. Liu. T. Nuimura, Distribution of debris thickness and its effect on ice melt at Hailuogou glacier, southeastern Tibetan Plateau, using in situ surveys and ASTER imagery, J. Glaciol., 57(206), 1147-1157, (2011).

Zhang, T., C. Xiao, W. Colgan, X. Qin, W. Du, W. Sun, Y. Liu, M. Ding, Observed and modelled ice temperature and velocity along the main flowline of East Rongbuk Glacier, Qomolangma (Mount Everest), Himalaya, J. Glaciol., 59(215), 438-448, (2013).

Zhisheng, A., J.E. Kutzbach, W.L. Prell, S.C. Porter, Evolution of Asian monsoons and phased uplift of the Himalaya-Tibetan plateau since Late Miocene times, Nature., 411(6833), 62-66, (2001).